THE UNIVERSITY *of* LIVERPOOL

High Frequency Finite Element Modeling and Condition Assessment of Power Transformers

Thesis submitted in accordance with the
requirements of the University of Liverpool
for the degree of Doctor of Philosophy

in

Electrical Engineering and Electronics

by

ZIWEI ZHANG, B.Sc.(Eng.)

September 2015

High Frequency Finite Element Modeling and Condition Assessment of Power Transformers

by

ZIWEI ZHANG

To my loving parents and dear sister.

Acknowledgements

First and foremost, I would like to express my deepest gratitude to my supervisor, Dr. Joseph Yan, not only for his dedicated supervision and insightful guidance, but also for his intellectual advice in both academic and personal level. Without his inspiration, I would not be at the stage I am now. I appreciate his vast knowledge and the attitude towards life. He is more of a mentor, than a supervisor to me.

A very special thanks goes out to my former supervisor, Professor Wenhu Tang. He truly made a difference in my life. It was under his tutelage that I expanded my knowledge broadly. He provided me with direction, technical and financial support, and a great opportunity to conduct the experiment and work with brilliant colleagues in South China University of Technology.

There have been many friends who walked alongside me during the last four years. They have guided me and showed me the doors that might be useful to open. I would like to thank each and every one of them. I would especially like to thank Mr. Kun Cao for his kind assistance in writing this thesis. Appreciation also goes out to Mr. Huan Lin for the valuable discussions in the cooperation.

Finally and without hesitation I would like to thank my parents and my sister for the support they provided me through out my entire life.

Abstract

Due to the reforming and deregulation of electric power industry, investments in transmission equipment have drastically decreased to meet the economic needs of the competitive market. The electrical utility sector was forced to cut the costs in maintenance and operation without endangering steady supply of electrical power. With this trend, the maintenance strategy desires advanced methods for condition monitoring and assessment of in-service power transformers. Among the common condition assessment techniques, Frequency Response Analysis (FRA) is considered as an efficient off-line diagnostic technique for fault detection in transformer windings. Precise interpretation of the FRA output has proven a great challenge and attracted much effort in recent years. There is also a strong need in this research field to develop an intelligent interpretation procedure for automatic assessment of power transformer conditions.

This thesis focuses on two main aspects of power transformer condition assessment: developing an accurate transformer model for the interpretation of transformer FRA responses, and establishing FRA-based novel algorithms to automatically identify transformer failure modes.

Reviewing existing transformer modeling methods, this thesis explicitly introduces a simplified distributed parameter model (hybrid winding model) for FRA. The hybrid winding model has the advantage of less computational complexity and high accuracy in simulation results, even in the frequency range above 1 MHz. Analytical expressions for calculating key electrical parameters of winding models are presented.

The electrical parameters of transformer windings with a complex or deformed structure are difficult to calculate using analytical formulations. Therefore, computational models based on Finite Element Method (FEM) are developed in this thesis to calculate the frequency-dependent parameters of transformer windings especially with deformed structures. These parameters are then applied to the transformer winding model for frequency response analysis. By applying the electrical parameters obtained from the FEM models, the

accuracy of the hybrid winding model has been improved for cases with incipient winding faults. This methodology is implemented in simulation studies of radial winding deformation and minor axial winding movement to reveal the characteristic features of these two types of winding fault. Results show that: (1) frequency-dependent inductances and structure-dependent shunt capacitance derived from FEM models can be used in FRA analysis, (2) by using the proposed methodology, characteristics of frequency response above 1 MHz can be analyzed, (3) regarding radial winding deformation and minor axial winding movement, the changes in the electrical parameters also affect the frequency response in the high frequency range (>1 MHz).

A Hierarchical Dimension Reduction (HDR) classifier built on FRA results is proposed in this thesis for condition assessment of power transformers. The algorithms of this classifier make advantageous use of advanced image processing technologies including image binalization and binary erosion in the first step of the procedure. This preprocessing procedure optimizes the measured FRA data by filtering the frequency sections with minor deviations which can effect the calculating results of the indices. Also in this step, FRA diagrams are re-scaled in a linear coordinate system for the convenience of calculating the indices in later step. Subsequently, based on the correlation between electrical properties and features of FRA responses, a division approach is proposed to dynamically divide the frequency range into 5 sub-bands. This division method of frequency range is more reasonable than the conventional methods of fixed frequency sub-bands and more applicable than other existing methods. Then the proposed algorithms of hybrid quantitative indices which include four indices are employed. The dimension reduction for the FRA data is processed by these algorithms in the 5 dynamic frequency sub-bands.

It is the first time to establish the algorithms of the hybrid quantitative indices, which include two classical indices and two novel indices, for reducing the dimensions of the FRA data. Two new algorithms of indices, Area Ratio Index (ARI) and Angle Difference (AD), are proposed based on knowledge of FRA interpretation with respect to typical transformer failure modes. They

are able to improve the classification performance in terms of the ability to identify electrical failures and the condition of residual magnetization.

Based on these advantageous processes, the HDR classifier can aggregate related expertise and approved statistical indices in furtherance of automatic decision analysis on identifying transformer failure modes or conditions. The performance of this classifier has been verified by 32 sets of experimental FRA data, in which 20 sets are primarily used for determination of threshold values of the related algorithms and the rest 12 are purely used for the verification. Results of this implementation of the HDR classifier are 100% accuracy with using the 20 sets of training data and 95.83% accuracy with using the rest 12 sets.

Contents

List of Figures

List of Tables

List of Abbreviations

Abbreviations

AD	Angle Difference index
AM	Asset Management
ARI	Area Ratio Index
CBM	Condition-based Maintenance
CC	Correlation Coefficients
CFM	Core defects Failure Modes
DGA	Dissolved Gas Analysis
DRC	Different Remanence Condition (Residual magnetization)
FEM	Finite Element Method
FFM	Floating shield/tank Failure Modes
FFT	Fast Fourier Transform
ELFM	Electrical Failure Modes
FRA	Frequency Response Analysis
FRAnalyzer	Sweep frequency response analyzer (product name)
FRSL	Frequency Response of Stray Losses
HC	Healthy Condition
HCRFM	High Contact Resistance Failure Modes
HDR	Hierarchical Dimension Reduction
HV	High-Voltage
IFRA	Frequency Response Analysis
kHz	kilo Hertz
LV	Low-Voltage
LVI	Low Voltage Impulse method

MEFM	Mechanical Failure Modes
MHz	Mega Hertz
MM	Mathematical Morphology
MTL	Multi-Transmission Line
MTLM	Multi-conductor Transmission Line Model
MV	Middle-Voltage
MVA	Mega Volt-Ampere
NCEPRI	North China Electric Power Research Institute
OCFM	Open Circuit Failure Modes
ODE	Ordinary Differential Equation
PD	Partial Discharge
PDC	Polarization and Depolarization Current
PDE	Partial Differential Equation
SCTFM	Short-Circuited Turns Failure Modes
SD	Spectrum Deviation
SFRA	Sweep Frequency Response Analysis
STLM	Single-Transmission Line Model
SE	Structuring Element
TBM	Time-based Maintenance
VFTO	Very Fast Transient Overvoltage
2D and 3D	2 and 3 Dimensional

Chapter 1

Introduction

1.1 Background

In electric power industry, a reliable and continuous supply of electricity is always considered as an essential requirement to achieve a fault-free operation of power systems. Unexpected failures cause major disturbances to operating systems, resulting in unscheduled outages. Usually replacement of equipment based on their rated service life can increase the reliability. However, power transformers, which provide indispensable services for transmission and distribution of electrical power, belong to the type of equipment operating on a condition-based replacement due to their high initial cost and longevity of service life. The cost of a transformer unit ranges from 2 million dollars to 4 million dollars, and it usually the most valuable equipment in a substation or plant [11]. Besides, transformers are highly dependable equipment. Many transformers in industrial plants and utilities are still operating normally beyond their recommended life-time.

Power transformers are usually designed with an expected life-time of 20-35 years. A large number of power transformers in UK have been in service for about 30 years [9]. With appropriate maintenance, the life time of a transformer may be extended to 60-70 years (or even more in some cases) unless there are convincible circumstances to scrap them, such as planned upgrade of

the network [12]. However, the failure rate of ageing transformers is steadily increasing.

The ratings of power transformers vary from a few tens of kVA to several hundreds of MVA [13]. There is ongoing trend for higher system voltages at transmission level which requires high transformer ratings. Transformers suffering from frequent overload conditions or other risks tend to have a shortened lifetime and thus threat the operation of the network. In fact, safe operation of power transformers acts as a premise of safe service of power systems.

In order to describe the abnormality of transformers without confusion, the definitions of 'failure' and 'failure mode' of transformers are clarified to fit into this thesis. A 'failure' of a transformer indicates either any forced outage of the transformer due to its fault in service, or any abnormal issue occurred in the transformer that requires any kind of repair [14]. A 'failure mode' of a transformer, which can be an incipient fault of the transformer or damages caused in transportation, is not necessarily a failure.

Any failure of a transformer could cause long-term outage of the corresponding network. Besides, other equipment in the interconnected power systems could also be affected by the transients caused by transformer failures, and subsequently relay protection devices can be triggered, leading to unscheduled outages. Moreover, transformer failures not only impair the system's performance, but also have a serious social impact due to cut of electricity supply. In a large power utility the number of transformers excluding those in the distribution network could be anywhere between a few hundreds and one thousand [12]. Failures of transformers while in service could lead to distinct revenue loss to the utility, high expenditure on inevitable maintenance or replacement, potential environmental damage, and even explosion or fire hazards [13]. According to the data from Doble Life of a Transformer Seminar, the financial loss due to transformer failures can cost up to 15 million dollars [11].

1.1.1 Condition Monitoring and Assessment of Power Transformer

Due to the restructuring and deregulation of worldwide electric power industry, investments in new transmission equipment have drastically decreased to meet the economic needs of the competitive market. The electrical utility sector was forced to cut the costs in maintenance and operation without endangering steady supply of electrical power. Asset Management (AM) is being adopted by the electrical utility sector to improve decision-making while facing immense changes in the operation and management activities [15, 16]. AM of transformers can be classified into the following activities: (1) condition monitoring and condition assessment techniques, (2) performing maintenance schedules, (3) ageing, health and end of life assessment [16].

With the developing trend in electric power industry, the asset managers changed the maintenance strategy of power transformers from time-based maintenance (TBM) strategy to more sophisticated condition-based maintenance (CBM) strategy. TBM strategy performs the inspection of all transformers over a constant time interval using a time schedule irrespective of the necessity for maintenance, while CBM strategy focuses more maintenance on high-risk transformers than on low-risk transformers [11]. As indicated by Roberts et al. [17], condition-based maintenance provides a planned maintenance strategy with benefits: (1) determine appropriate time to perform maintenance activities, (2) reduce the average mean time of maintenance based on additional information, (3) detection of the incipient faults gains more time to develop appropriate maintenance plans. Therefore, to meet the requirements of CBM, there is an urgent need to develop advanced diagnostic methods to provide reliable information about the conditions of transformers for maintenance schedule. In recent years, many transformer monitoring and assessment techniques have been developed offering advantageous abilities to know the overload capability of the transformer and to diagnose the faults in the active part and accessories such as tap-changers and windings [18].

Transformer failures can be caused by either internal or external factors.

They can be broadly categorized as electrical, mechanical, or thermal [12]. The causes of the failures in terms of the internal factors include insulation deterioration/ageing, partial discharge, loss of clamping pressure, winding resonance, overheating, and defects during manufacture; whereas the external factors include lightning strikes, short-circuit forces from system faults, overloading and system switching operations. The causes are inter-related in some cases. For example, ageing may lead to loosened winding clamping, thereby reducing the mechanical integrity of windings. Acting along with a short-circuit fault in the system, this can ultimately lead to catastrophic failure of transformers. Documented surveys on transformer failures are listed in Table 1.1 [9, 12, 19, 20].

Table 1.1: Percentage of failures in power transformers [9]

Document Source	Doble Client [19]	CIGRE [12]	South Africa [12]	North America [20]
	Percentage of failures (%)			
Windings (ageing & distortion)	28	19	17	50
Tap changer	16	41	24	21
Tank/dielectric fluid	9	13	30	10
Core	7	3	15	2
Bushings	35	12	14	11
Accessories	5	12		6

From Table 1.1, it can be found that transformer failures relevant to windings take up a large percentage according to the documented surveys. Consequently, failure in transformer windings has attracted a great amount of attention.

In order to mitigate the high failure rate caused by defects in windings, developing methods of detecting incipient faults in windings is one of the major challenges in transformer condition monitoring and assessment. Although such faults usually do not necessarily affect the normal operation, the ability to with-

stand short circuit and overvoltage may be degraded severely. This degradation of the withstand strength could lead to failure eventually. Further explanations regarding winding deformations and other transformer failure modes can be found in Section 2.2 in Chapter 2.

1.1.2 Diagnostic Techniques

There are various diagnostic techniques available to evaluate the condition of transformers, both off-line and on-line. These diagnostic techniques, including which are currently used and developed further, mainly target at specific types of fault in a transformer [10,12,21]. Some of the techniques are designed for assessing the overall conditions of transformers, such as dissolved gas analysis (DGA) [22,23]. Whereas some diagnostic methods such as partial discharge (PD) analysis [13, 24, 25], furan analysis [13], polarization and depolarization current (PDC) measurement [26, 27], and frequency responses analysis (FRA) are aimed at detection of specific faults.

Each diagnosis technique is always weighed against other methods. Techniques which have been established over the years satisfy important criteria, some of which are as follows: (1) sensitivity to important parameters of transformer condition, (2) reproducibility of results over time and for different testing personnel, (3) compensation of raw data for significant environmental effects like temperature, (4) good correlation with other established methods and (5) availability of valuable information for the time and expense involved [13].

With regard to the faults in windings, the available techniques are compared as listed in Table 1.2 [10].

From the comparison, it can be found that most of the alternative techniques suffer from the lack of sensitivity or reference results, or both [10]. Among the existing diagnostic techniques, Frequency Response Analysis (FRA) is best known for its proven sensitivity to faults in transformer windings, that are one of the major types of transformer fault. To ensure the effectiveness of this technique in transformer condition assessment, two aspects are to be improved: standardization of techniques and guide to interpretation [10]. Cur-

Table 1.2: Comparison of main electrical diagnostic techniques for winding deformation [10]

Diagnostic technique	**Advantages**	**Disadvantages**
Magnetising (exciting) current	Requires relatively simple equipment. Can detect core damage.	Not sensitive to winding deformation. Strongly affected by core residual magnetism.
Impedance (leakage reactance)	Traditional method specified in short-circuits test standards. Reference (nameplate) values are available.	Very small changes can be significant. Limited sensitivity for some failure modes.
Frequency Response of Stray Losses (FRSL)	Can be more sensitive than impedance measurement. Almost unique to detect short circuits between parallel strands.	Not a standard use in the industry.
Winding capacitance	Can be more sensitive than impedance measurements. Standard equipment available.	Limited sensitivity for some failure modes. Relevant capacitance may not be measurable (e.g. between series windings for auto transformers).
Low Voltage Impulse (LVI) (time domain)	Recognized as very sensitive.	Specialist equipment required. Difficult to achieve reproducibility and interpretation.
Frequency Response Analysis (FRA)	Better reproducibility than LVI with the same sensitivity. Easier to interpret than LVI (frequency domain instead of time domain). Increasing usage.	Standardisation of techniques required. Guide to interpretation required.

rently the international standards such as CIGRE brochure 423 [10], EN 60076-18 [28] originally provided by IEC, and IEEE Std C57.149 [29] have provided guidance on measurement standardization of FRA techniques, and some general interpretations. Guidance on measurement standardization ensures the reliability and reproducibility of the measured results. However, since the FRA technique is based on comparison of the frequency response fingerprints between the 'reference' response and the 'suspected' response, the success of the technique heavily depends on the interpretation of deviations in terms of fault types and severity of deformation. More precise interpretations of FRA output are still worthwhile to be investigated.

1.1.3 Motivations

Practically, the characteristics of frequency response of a transformer can be accessed in two ways. The first is to make physical measurement on the transformer winding structure. The second is to model the transformer analytically [29]. An analytical winding model has the advantages of simulating fault conditions mathematically and investigating the sensitivity of the frequency response to changed parameters. Thus, taking advantage of the development of computational tools as well, there is a growing interest on investigation of modeling of power transformers in recent and forthcoming years.

In practical application, an interpretation of frequency responses is usually conducted by human experts based on visual comparison of reference and suspected responses. Although the role of human experts is irreplaceable, it is still possible to minimize its involvement, so that the FRA results can be assessed easier even for non-specialist. For this reason, research effort has been devoted to a reliable quantitative interpretation method by using statistical indices (or indicators) in recent years. However, the current quantitative interpretation methods only provide the information on the severity of deformation on transformer windings, rather than identifying the types of failure modes. Hence, the challenge in this regard is placed on developing intelligent interpretation tools for automatic assessment of power transformers.

1.2 Research Objectives

Based on the aforementioned discussion, detection of incipient faults in transformer windings is an extremely important task in this research field. The reason is that it can effectively support AM decisions to reduce the failure rate of transformers in service and thereby minimizing the cost due to unplanned outages. FRA is considered as the most suitable diagnostic tool for this task. In respect of the deficiency of the FRA technique on the interpretations at current stage, two main aspects are worthwhile to be investigated. The first one is aimed at precisely interpreting the FRA response for typical and specific cases to incipient winding faults by developing an accurate transformer model. The other is aimed at establishing an intelligent tool for identifying the types of failure modes automatically. Therefore, the research objectives in this thesis consist with these two aspects.

Regarding the first aspect of the objectives, the work is devoted to improving the performance of winding models for FRA interpretations of specific cases to incipient winding faults. The following tasks will be included:

- Constructing computational transformer models using Finite Element Method (FEM) for the purpose of calculating the electrical parameters corresponding to each specific case of winding deformation. This part of the work is expected to obtain more accurate values of electrical parameters compared with conventional analytical approaches.

- Utilizing a proper winding model and detailed electrical parameters to simulate typical modes of winding deformation.

- Identifying and characterizing the specific features of FRA output to each type of winding deformation to support the interpretation of corresponding winding faults.

Regarding the second aspect of the objectives, the work is devoted to the establishment of algorithms of an automatic transformer condition classification procedure. The following tasks will be included:

- Establishing a reasonable approach to divide the frequency range into sub-bands according to the correlation between electrical properties and features of FRA responses.
- Developing algorithms of quantitative indices for reliable interpretation of FRA responses.
- Developing an intelligent classifier for automatic assessment aiming at identification of the failure modes.

1.3 Thesis Overview

This thesis contains six chapters which describe the progress of the research in achieving the aforementioned objectives. In addition to the outline of the work, the other chapters are structured as follows:

Chapter 2 introduces background knowledge on transformer winding condition assessment using Frequency Response Analysis. This chapter begins with an introduction of typical transformer failure modes. Then fundamentals of the transformer condition diagnosis tool, FRA, are presented. This is followed by an introduction to the practical FRA measurement and examples of experiment data.

Chapter 3 reviews widely used winding modeling methods. Then a simplified distributed parameter model (hybrid winding model) is introduced in detail. Finally, conventional analytical expressions used to calculate parameters in the winding model are presented.

Chapter 4 shows the process of constructing computational FEM models with regard to an undeformed case and certain cases of different winding deformations. Effective permeability tensor of winding conductors, frequency-dependent inductances, shunt capacitances are obtained from these models. Then the results of theses FEM models are applied in the hybrid winding model for simulation studies of an undeformed case and

cases of incipient winding faults in both low and high frequency ranges. The frequency response in the undeformed case is compared with experimental results to verify the accuracy of the frequency-dependent parameters and mathematical winding models. Four cases of radial winding deformation and three scenarios of minor axial winding movement are analyzed in detail.

Chapter 5 firstly presents the procedure to preprocess the measured FRA data using image processing technologies, including image binalization and binary erosion. This procedure would support the new algorithms of the indices proposed in this chapter and improve the sensitivity of the rest of utilized indices. Combined with the preprocessed data, a new approach of dynamic division of frequency sub-bands is proposed. Two new algorithms of indices are proposed next, and then a classifier which uses hybrid quantitative indices to reduce the dimensions of the raw input FRA data is designed for classification of typical transformer failure modes or conditions.

Chapter 6 concludes the thesis summarizing the obtained results, and discusses prospective directions of further research.

1.4 Key Contributions

One of the major contributions arising from this research is the calculation of elementary parameters of equivalent circuits with regard to typical transformer winding deformations, by developing computational FEM models implemented in commercial software packages (COMSOL). In this manner, relevant parameters affected by mechanical winding deformation can be accurately obtained, factoring diamagnetic properties and the influence of frequency (Chapter 4). This approach improves frequency response modeling of power transformers, which furthers interpretation of FRA results. The effect of inductance and capacitance on frequency responses with respect to radial winding

deformation and minor axial winding movement is explored in an extended range of frequencies above 1 MHz by applying the specific parameters into a refined hybrid winding model. This sophisticated methodology provides an effective approach to extract characteristic features of incipient winding faults from FRA data, thereby guiding the identification of similar fault features from measured frequency response data.

Another major contribution of this research is the proposal of a classifier called Hierarchical Dimension Reduction Classifier (HDR Classifier) (Chapter 6). This classifier is designed to identify typical transformer failure modes or conditions using the hybrid quantitative indices that reduce the dimensions of the raw FRA data. This classifier can aggregate expertise and approved statistical indices in furtherance of automatic decision analysis on identifying transformer failure modes or conditions. Meanwhile, the utilization of image processing technologies to preprocess FRA curves optimizes the data set for calculations of the involved indices. Besides, this research also proposed a dynamic approach to divide the frequency range into 5 sub-bands according to the correlation between electrical properties and features of FRA responses. The proposed algorithms of indices, Area Ratio Index (ARI) and Angle Difference (AD), which are applied within the HDR classier, show high performance in identification of electrical failures and the condition of residual magnetization.

1.4.1 Research Publications

1. **Z.W. Zhang**, W.H. Tang, T.Y. Ji, Q.H. Wu, Finite Element Modeling for Analysis of Radial Deformations within Transformer Windings, *IEEE Transactions on Power Delivery*, vol.29, no.5, pp.2297,2305, Oct. 2014. [30]

2. **Z.W. Zhang**, W.H. Tang, J.D. Yan, Q.H. Wu, Detection of Minor Axial Winding Movement within Power Transformers Using Finite Element Modeling, *PES General Meeting | Conference Exposition, 2014 IEEE*, pp.1,5, 27-31 July 2014. [31]

3. **Z.W. Zhang**, J.D. Yan, W.H. Tang, H. Lin, Automatic Transformer Condition Classification Using Binary Erosion and Hybrid Indices. *Electric Power Systems Research*, submitted.

4. **Z.W. Zhang**, J.D. Yan, W.H. Tang, Experimental Investigation of Localized Axial Winding Displacement in High Frequency Range for Power Transformers. *2016 International Conference on Condition Monitoring and Diagnosis (CMD)*, submitted.

Chapter 2

Transformer Winding Condition Assessment Using Frequency Response Analysis

2.1 Introduction

This chapter presents an introduction to transformer failure and the popular diagnosis technique FRA for transformer winding conditions. Frequency response analysis (FRA) has been widely adopted to detect defects caused geometric changes within a transformer [29, 32–35]. These defects are commonly referred to as failure modes. As the aforementioned statement in Chapter 1, a transformer failure modes is not necessarily a failure. However, some defects, once they appear, can greatly reduce the possibility of a transformer surviving further deformations. The FRA technique originates from the Low Voltage Impulse method (LVI) which was introduced in 1966 [36]. It is based on the low-voltage rectangular impulse injection into a terminal of transformer windings and registration of the transient impulse response in the time domain. It was used as an off-line test for transformer winding condition monitoring due to the high sensitivity to winding defects [37, 38]. However, this technique has deficiency on the reproducibility of the measurement. With the discovery of

the good reproducibility of the transfer function in the frequency domain, the time-domain LVI method evolved into the frequency-domain impulse method which is also known as the Impulse Frequency Response Analysis (IFRA). In order to obtain the transfer function in the frequency domain directly, a new technique employing an frequency-varied sinusoidal signals was proposed by Dick et al. in 1975 [39]. This method was later named Sweep Frequency Response Analysis (SFRA). By comparing these two techniques [6, 40], FRA was gradually replacing the previously used LVI technique due to the higher sensitivity to winding defects and good reproducibility of the measurement.

In this chapter, typical transformer failure modes are discussed first. Secondly, fundamentals of FRA are presented, which are followed by an introduction of the practical FRA measurement with an example of experimental setup.

2.2 Transformer Failure Modes

Transformer failure modes are not exclusive to geometric variations within a transformer and can include variation in the core's magnetic circuit and contact resistance [29]. The failure modes are generally categorized as mechanical failure modes and electrical failure modes. Mechanical failure modes can be caused by many factors, such as strong electromagnetic forces arising from short-circuit faults, tap-changer faults, improper transportation, explosion of combustible gas in transformer oil, natural disaster, etc. Electrical failure modes refer to the change(s) of circuit within a transformer, such as short-circuit between turns, open circuit in a winding, etc. As mentioned in Chapter 1, the causes of the failure are complicated and usually inter-related. Thus the detected variations in a FRA test can be caused by a single type of failure modes or a combination of different failure modes.

The typical failure modes of transformers are categorized and listed below [10, 29, 41, 42]

- **Mechanical Failure Modes (MEFM)**:

  - Winding deformation modes caused by short-circuit forces:
    - Radial buckling
    - Conductor tilting
    - Conductor bending between spacer columns
    - Conductor telescoping
    - Spiral tightening under twisting forces
    - Collapse of the winding end supports
    - Movement of winding leads
  - Other reasons:
    - Winding looseness due to transportation

- **Electrical Failure Modes (ELFM)**:
  - Core defects (CFM)
  - Short-circuited turns (SCTFM)
  - Open circuit in a winding (OCFM)
  - High contact resistance (HCRFM)
  - Floating shield/tank (FFM)

- **Other abnormal conditions** :
  - Different Remanence Condition (Residual magnetization) (DRC)

Brief explanations of these failure modes are presented in the next sub-sections.

2.2.1 Short-circuit Forces

Of all possible transformer faults, winding deformation arising from short-circuit force is probably the most common type. An unexpected transient generated by faults of another piece of equipment in the attached network could result in a short circuit, and when this happens, the magnitude of the 'through

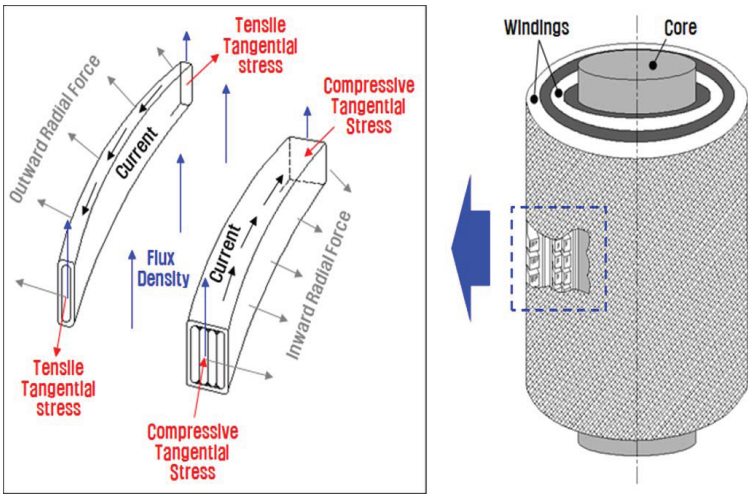

Figure 2.1: Directions of short-circuit, leakage flux and corresponding electromagnetic force [1]

fault' current is usually much higher than the normal in-service current (probably in up to 20 times). The amplitude of the first current peak can be nearly twice of the steady-state short-circuit current [10, 43]. Besides, out-of-phase synchronisation in the network could lead to a current in a transformer that is greater than or similar to a short-circuit current [10].

Short-circuit current in transformer windings and leakage flux produce an Lorentz force (electromagnetic force) acting on transformer windings, as shown in Fig. 2.1. It can be derived from the general equation below [1, 42, 44]:

$$\mathbf{F} = \int_l I_{sc} d\mathbf{l} \times \mathbf{B} \tag{2.2.1}$$

where, boldface means a vector, I_{sc} represents the short-circuit current, $\mathbf{F}$ denotes the Lorentz force, l is the length of the winding, $d\mathbf{l}$ is the space vector of the winding and $\mathbf{B}$ is the leakage flux density.

In a core-form transformer, the axial leakage flux and circumferential winding current produce radial electromagnetic forces which tend to push parts of the windings apart. The radial force acts inwards on inner winding conductors and exerts excessive compressive tangential stress along the winding. On the outer winding conductors, the force acts outwards and produces tensile tan-

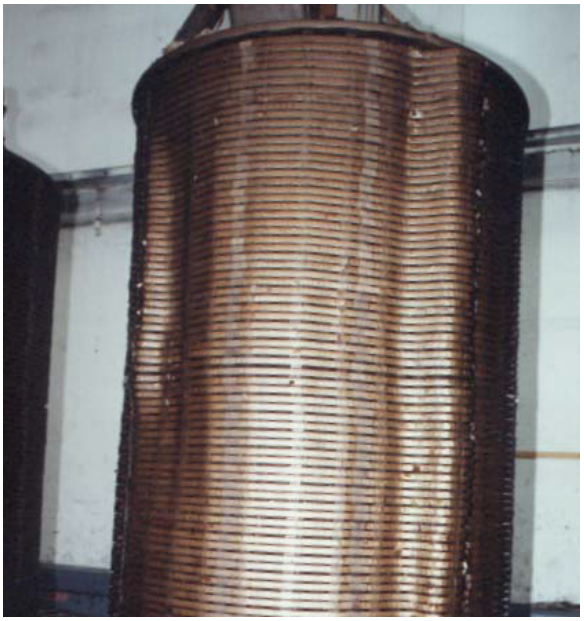

Figure 2.2: Radial buckling

gential stress along the winding. The most critical effect is the inward force on the inner winding that can lead to 'hoop buckling' (Fig. 2.2).

The interaction between winding current and radial magnetic flux produces axial electromagnetic forces which tend to compress the conductors and lead to further tilting or bending of the conductors. These two types of axial deformation are briefly illustrated in Fig. 2.3. Keeping each group of windings symmetrical about its electromagnetic centre is one of the key points in the design and manufacture of large transformers. Once it is not symmetrical or a slight displacement happens due to transportation for instance, an unbalanced compressive stress could be generated which acts on individual windings. In other words, axial winding deformation can be worsen because of the asymmetrical physical structures of a set of windings. Besides, there is some degree of spiralling in core-form windings, which may lead to a twisting force on the windings. This force tends to tighten the winding. In practice, these violent electromagnetic forces often cause compound winding deformations.

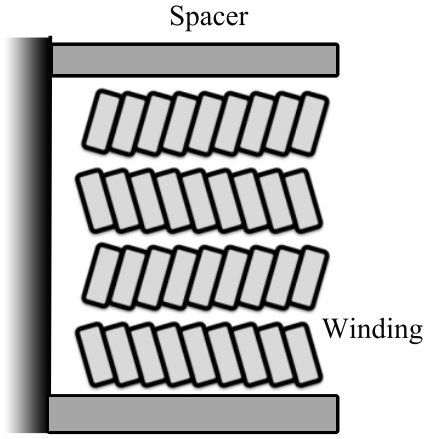

(a) Conductor tilting

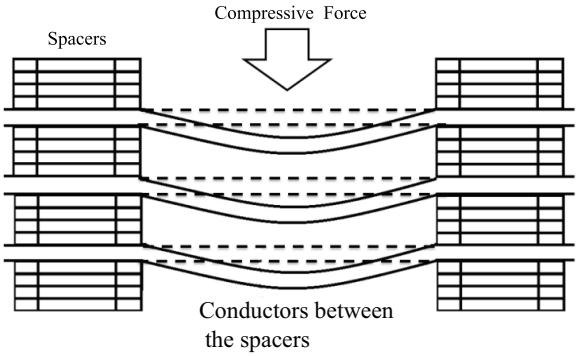

(b) Conductor bending

Figure 2.3: Axial winding deformation: (a) Conductor tilting (b) Conductor bending [2]

2.2.2 Other Typical Failure Modes or Abnormal Conditions

In addition to the most commonly met winding deformation faults, other types of defects or abnormal conditions are introduced as below:

Winding looseness due to transportation Winding looseness of a power transformer frequently occurs during the transportation. This failure mode is described as the gradual spreading of the disk-to-disk or turn-to-turn distances axially along a winding (Winding movement). This type of fault is further studied by modeling simulations in Chapter 4. During the transportation, in order to avoid moisture absorption of the transformer components, the tank is filled with dry air or other gas without chemical impact on the transformer insulation layers. The oil is injected on site. Therefore, FRA tests will be taken with the transportation assembling before and after the transportation to detect any possible winding looseness.

Core defects (CFM) All defects in cores, such as burnt core laminations, joint dislocations, lost/ multiple/ unintentional core grounds, and shorted core laminations, can lead to variations of the magnetic circuit in cores [29].

Short-circuited turns (SCTFM) Short-circuit turns can happen between adjacent turns or phases due to insufficient insulation.

High contact resistance (HCRFM) Poor contact conditions of tap changers which connect bushings and windings may cause high impedances during tests. This is not a classical failure mode, but it can be detected by the FRA.

Open circuit in a winding (OCFM) Loose connections or burned coils may lead to an open circuit, which results in high impedances during measurements. It commonly leads to a drop across a wide spectrum of the FRA

curves [29]. When it goes to a complete open circuit, the FRA results will lose the characteristic patterns.

Floating shield/tank (FFM) Floating shield or tank could result in high resistance between the winding and shield/tank which increases the damping effect of the transfer functions.

Different Remanence Condition (Residual magnetization) (DRC) DC winding resistance testing, switching operations and geomagnetic phenomena can lead to magnetic flux remaining in the core steel, which is the residual magnetization. This is not a failure mode, but the existence of residual magnetization could induce a mis-interpretation of the FRA results. It can be removed by demagnetizing the core.

2.3 Frequency Response Analysis (FRA)

FRA has been widely used to detect faults in transformer windings [32–35]. It is a non-invasive and sensitive diagnostic method based on the fact that the frequency response of a transformer winding is sensitive to its internal physical change, which causes variations of the electrical parameters of the winding, such as inductance and capacitance [45]. Basically FRA relies on a comparison between the measured frequency response and a reference taken from the same winding during previous tests or from a type-based (sister unit) or construction-based (phase) transformer [41]. The difference contains information of internal winding movements or deformation. Therefore, the main purpose of FRA is to detect winding deformation or displacements in transformers, and it is often used for condition assessment following an event where mechanical deformation or electrical damage could possibly happen, for example, transportation of a transformer, or changes occurring in other tests. Moreover, there is a growing interest in using FRA in transformer or system modeling to understand the 'fault conditions' of a transformer or its connected network [10, 29].

An transformer can be regarded as a complex RLC network, so transformer

windings can be represented by distributed electrical elements, namely, resistances, inductances and capacitances. Figure 2.5 illustrates a brief example of the equivalent RLC circuit of the transformer winding, which includes the conductor inductance and resistance, inter-turn capacitance, and shunt capacitances between two windings,or the winding and the core, or the winding and the tank. The RLC circuit is entirely depended on the physical geometry, construction and material properties of the transformer. Hence, any mechanical change alters the values of the RLC elements in the equivalent circuit. Sufficiently different combinations of these elements in turn alter the frequency response, which is in the form of a transfer function. A transfer function is defined as the ratio of the output response signal to the input signal. It is independent of the injected signal and fully characterizes the corresponding time-invariant linear system [46]. A block diagram representing the transfer function is shown in Fig. 2.4, where $H(s)$ is the voltage ratio, or the impedance, or the admittance.

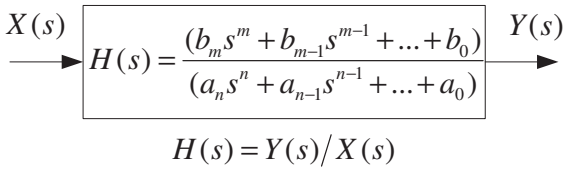

Figure 2.4: Block diagram of a transfer function

There are two commonly used methods to analyze the frequency response, Impulse Frequency Response Analysis (IFRA) and Sweep Frequency Response Analysis (SFRA) [12]. With the development of these two methods, purpose-built instruments for the application of IFRA or SFRA have been produced by manufacturers in recent years. These two methods are introduced in the following subsections.

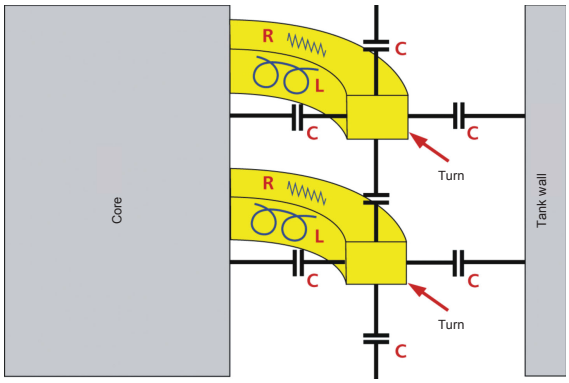

Figure 2.5: Equivalent RLC network of the transformer winding [3]

2.3.1 IFRA

Using this method, a double exponential impulse signal with pre-set rise&fall time is injected into one of the terminals of a winding, and simultaneously this applied signal as well as the corresponding response signal from the other terminal are measured by a dual channel digital instrument. Both measured signals are then converted into the frequency domain using the Fast Fourier Transform (FFT) algorithm [47]. Finally, the transfer function is defined as the ratio between the FFT of the response signal to that of the injected signal.

Compared with Low Voltage Impulse (LVI) which uses the same type of impulse signal as input signal in the time domain [10,36,38], the key advantage and improvement of IFRA is that the transfer function in the frequency domain is independent from the amplitude of applied impulse as long as the transformer can be considered as a linear and time-invariant system, which means the response embodies more information of the test object itself without much relevance to the test set-up. As a result, the interpretation is simplified and the repeatability is improved. The advantages of this IFRA compared with the SFRA techniques, which are described in the next subsection, are simultaneous and faster measurement of multi-types of transfer function [6, 40]. However, it really depends on the test instruments in nowadays, because some modern SFRA instruments, such as FRAnalyzer produced by *OMICRON*, can also

carry out different types of frequency responses (i.e., voltage ratio, admittance, impedance) without requiring any reconnection. In theory, under the same test condition, IFRA and SFRA techniques should obtain the same result. However, when applying the impulse method, the possibilities of encountering drawbacks should be concerned [6, 40]:

- Fixed frequency resolution leading to poor resolution at low frequencies that reduces the sensitivity of detection of short-circuited turns or core related faults. Besides, in order to avoid window functions of FFT, high-pass filters are usually used which also reduce the resolution at low frequencies.

- The applied source must produce enough energy in the whole frequency range of interest, otherwise it will cause different resolutions across the frequency range. In other words, the upper bound of the frequency band is limited by the diminished energy of the applied impulse at higher frequencies.

- Noise corruption because of the transfer from time domain to frequency domain. Even a very small error in signal measurement can cause significant deviations in the calculated frequency responses after the FFT transformation.

2.3.2 SFRA

This technique is performed by making a frequency sweep at predefined frequencies using constant amplitude sinusoidal signals as inputs which can be represented by:

$$U(t) = A{\cdot}sin(2\pi f_{sweep}t), f_{sweep} \in [f_{min}, f_{max}], \tag{2.3.1}$$

where A denotes the constant amplitude of the injected sinusoidal signal, and the sweep frequency f_{sweep} varies based on pre-set modes in the frequency range (f_{min}, f_{max}). The value of A is decided by the chosen types of FRA instruments.

By using this sweep frequency technique, the frequency response of windings can be determined directly in the frequency range of interest.

A typical measurement setup of SFRA is illustrated in Fig. 2.6. The cable impedance (source impedance/reference impedance/output impedance) of a network analyzer is usually 50 Ω, and it usually contains three channels which are 'source', 'reference' and 'measurement'. A frequency-variable sinusoidal signal from the 'source' channel excites the RLC network at one end of a terminal (usually an high-voltage (HV) terminal), and from the same terminal a reference signal $U1$ is measured by the 'reference' channel. Simultaneously, the response signal is measured at another terminal (usually an HV neutral) by the 'measurement' channel. Subsequently, following the instructions of various FRA equipment producers and recommendation standards [3,48], the response magnitude in the most common form of voltage ratio k can be derived in decibel (dB):

$$k = 20 \lg \left| \frac{U_2(2\pi f)}{U_1(2\pi f)} \right|, \tag{2.3.2}$$

and the responses phase in degrees–Hz or radian-Hz can be obtained by:

$$\varphi = \angle \left(\frac{U_2(2\pi f)}{U_1(2\pi f)} \right). \tag{2.3.3}$$

The response magnitude has been considered to convey more information than the response phase, so most literatures related to FRA pay more attention to the response results of magnitude, so does this research study.

To understand the transfer function in FRA test mathematically, a simple equivalent circuit of the SFRA measurement (Fig. 2.6) is depicted in Fig. 2.7, where Z_s, Z_{ref} and Z_m denote the source impedance, reference impedance and measurement impedance (or output impedance), respectively. These impedances are typically 50 Ω as mentioned previously, and Z_{tr} represents the impedance of tested transformer. From the computation based on the equivalent circuit, the source current I_{tot} flowing from the source channel can be calculated by (2.3.4), and the transfer function of voltage ratio is derived in (2.3.5). From (2.3.4) and (2.3.5), it can be found that the transfer function is independent of

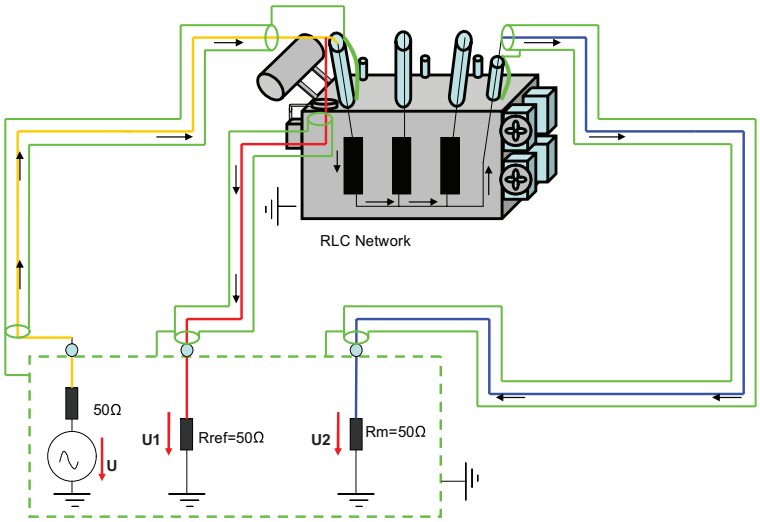

Figure 2.6: FRA measurement setup

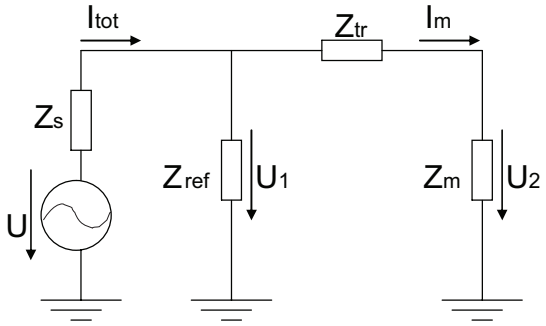

Figure 2.7: FRA measurement setup

the source signal, but the source current is proportional to the source voltage.

$$I_{tot} = \frac{Z_{tr} + Z_{ref} + Z_m}{Z_s(Z_{tr} + Z_{ref} + Z_m) + Z_{ref}(Z_{tr} + Z_m)} \cdot U \tag{2.3.4}$$

$$H(s) = \frac{U_2(s)}{U_1(s)} = \frac{Z_m}{Z_{tr} + Z_m} \tag{2.3.5}$$

The available frequency range of SFRA is usually wider than that of the impulse response method. According to [49], the measuring frequency range for test objects with a rated voltage $>$ 72.5 KV is 20 Hz – 1 MHz, and for test objects with a rated voltage $\leq$ 72.5 KV is 20 Hz – 2 MHz. In general, the IEC

recommends using at least 2 MHz in all tests for compatibility and simplicity. However, some researchers suggests an upper bound of 10 MHz [34]. According to the experimental results reported in [34], the frequency response in a higher frequency range is more sensitive to minor winding deformation.

The SFRA method is applied throughout this thesis. Hence, in this thesis the term FRA (Frequency Response Analysis) is used as a general term referring to SFRA in later chapters. The measurement setup of FRA is introduced in the next section.

2.4 Practical FRA Measurement

Basically, the characteristics of the frequency response of a transformer winding can be accessed in two ways. The first method is to compute the frequency responses mathematically by constructing an accurate analytic model of transformer windings. The simulation of transformer winding and the development of accurate computational models for undeformed and deformed transformer winding for calculating the parameters are parts of the essential tasks in this research and delivered in later chapters. In this section, the second method, which is to make physical measurements on transformers, is presented.

Considering that a three-phase transformer consists of several windings, the detected results with different ways of connections during the tests are not necessarily equally sensitive to the same winding deformation. In some recent literatures, e.g., [33, 45], the sensitivities of different connection methods were compared for different types of winding deformation. Some institutions like CIGRE [10], IEEE [29] and IEC [49] have intended to standardize the FRA practices, so that the quality of the measurement can be improved. More details of test techniques can be found in [10, 29, 49]. Here some essential information related to the FRA measurement is summarized, and a practical experiment measurement is delivered as a case study.

2.4.1 Connection Types

A basic measurement setup is demonstrated in Fig. 2.6 and briefly introduced in Subsection 2.3.2. According to the standard [10], the leads of source and reference coaxial cables are tapped together near the flange of the bushing. The cable shields are connected to the tank using a short lead. A lead extension runs along the body of the bushing to connect the signal to the bushing terminal. The same principle applies for the response cable.

The main FRA test types are described as follows.

End-to-end open-circuit

An end-to-end open-circuit measurement is made from one end of a winding to another with other untested terminals floating. The open-circuit test can be applied to both single-phase and three-phase transformers, and it is the most commonly used method due to its simplicity and the possibility to examine each winding separately. Open-circuit test results are primarily influenced by the core properties at or around the fundamental power frequency.

The end-to-end tests can be made with the source applied on the phase terminal or on the neutral terminal for star connected phases (standard phase configurations of three-phase transformers are shown in Fig. 2.8). The measurement principle is shown in Fig. 2.9(a). In this case the source and reference channels are connected to the neutral terminal while the response measurement channel is connected to one of the star connected phases.

End-to-end short-circuit

The short-circuit measurement is similar to the end-to-end open-circuit measurement above, but with associated windings on the same phase being short-circuited. For repeatability purposes, it is recommended that all associated windings are short circuited on three-phase transformers to create an equivalent three-phase short-circuit model, and available neutral connections should not be included in the shorting process [29]. This ensures that all

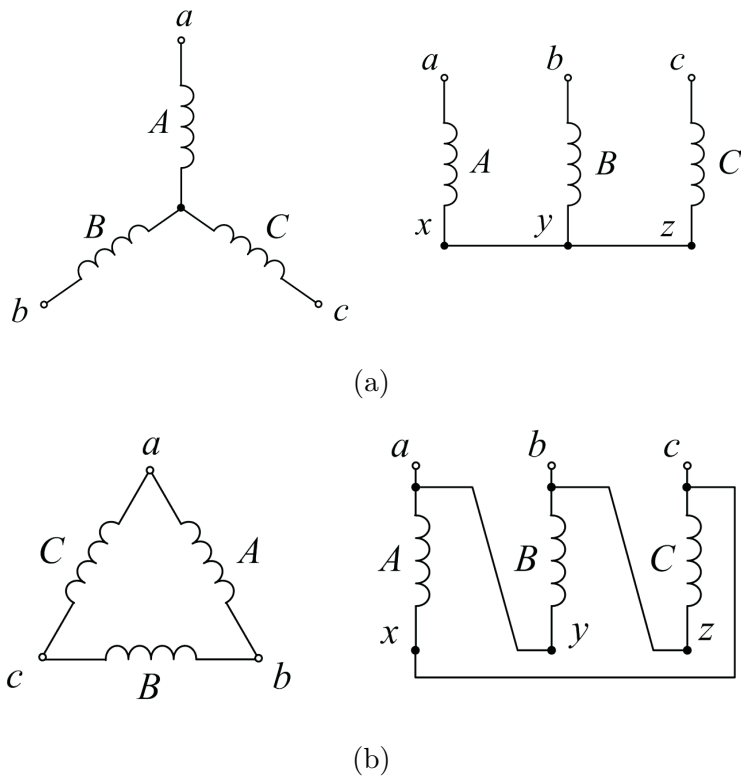

Figure 2.8: Standard phase connection configurations: (a) "star" (or "Y") phasor diagram and winding connections, (b) "delta" (or "Δ") phasor diagram and winding connections [4]

three phases are similarly short circuited to give consistent impedance. The short-circuit test removes the influence of the core below around 10-20 kHz, so the low-frequency response is determined by the leakage inductance instead of the magnetizing inductance. Therefore, the short-circuit results should produce similar and comparable diagnostic information as seen in both leakage reactance and dc winding resistance measurements, and the response at higher frequencies is similar to the one obtained using end-to-end open-circuit measurement.

The measurement principle for end-to-end short circuit is shown in Fig. 2.9(b). In this case the source and reference channels are connected to the neutral terminal while the response measurement channel is connected to one of the star connected phases, and the corresponding windings are short circuited.

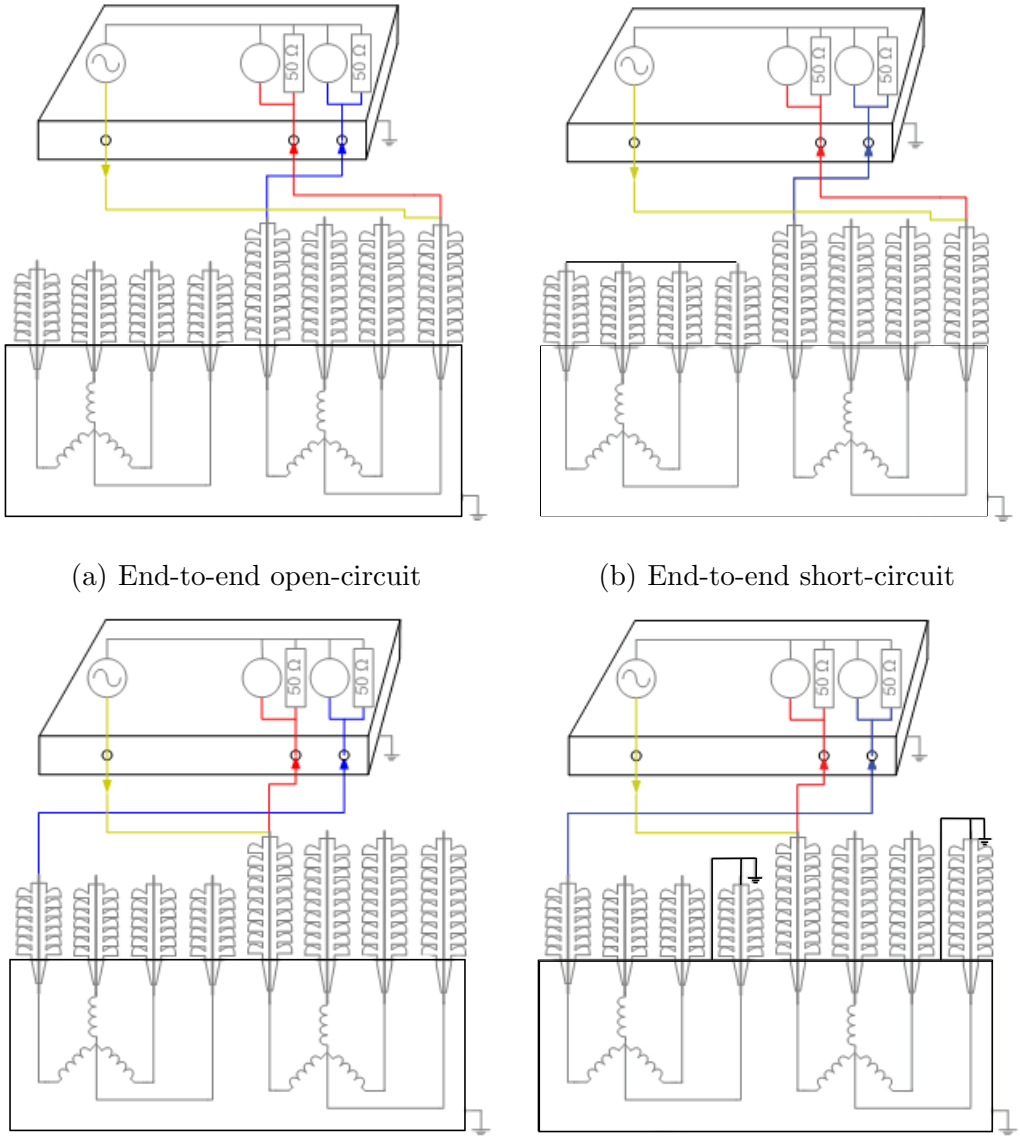

(a) End-to-end open-circuit

(b) End-to-end short-circuit

(c) Capacitive inter-winding

(d) Inductive inter-winding

Figure 2.9: Typical measurement connections: (a) End-to-end open-circuit, (b) End-to-end short-circuit,(c) Capacitive inter-winding, (d) Inductive inter-winding

Capacitive inter-winding

A capacitive inter-winding measurement is conducted between two electrically isolated windings. To perform this measurement, the source signal is applied to one end of the winding and the response signal is measured at one

end of another winding on the same phase, with all other terminals floating. Due to its capacitive property in nature, the trend of the impedance response generally decreases with frequency. This measurement principle is shown in Fig. 2.9(c).

Inductive inter-winding

An inductive inter-winding measurement is performed between two windings with one end of each winding grounded. The source signal is applied to a terminal of a HV winding, and the response signal is measured on the corresponding terminal of a low-voltage (LV) winding. The other end of both tested windings should be grounded, and other untested terminals should remain floating. This measurement principle is shown in Fig. 2.9(d). At or around the fundamental power frequency, this test result is determined by the winding turns ratio.

2.4.2 FRA Instrument Features

Noise is defined as unwanted disturbances that may be superimposed upon a useful signal. During a measurement, noise may affect or obscure the FRA results. Therefore, an understanding of the sources of noise, its detection and mitigation are necessary.

Two forms of noise, wideband and narrowband noises, can be found in a substation environment [5,50]. The wideband noise is related to the noise floor which is the sum of all the noises and unwanted signals within a measurement system. Therefore, the presence of wideband noise in an FRA curve depends on the dynamic range of the instrument in use. According to the FRA measurement standard [51], all FRA instrument should have a dynamic range of at least -100 dB to 20 dB. A typical narrowband noise is the power frequency noise (50 or 60 Hz noise) which is only present when measurements are carried out on-site in substations with strong electromagnetic fields. It usually appears between 30 Hz and 100 Hz, and when the frequency is higher than 300 Hz, this kind of noise almost disappears. However, high harmonic pollution

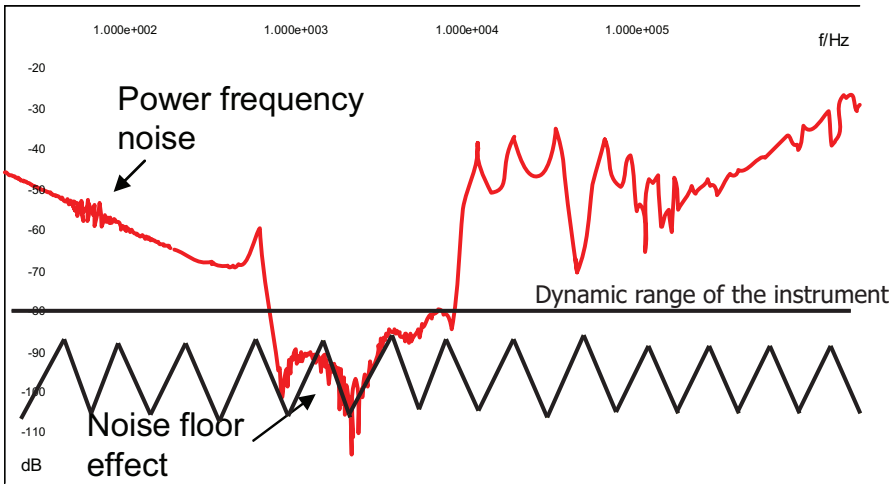

Figure 2.10: Characterization of noise in a FRA plot

may lead to detectable narrowband noises at the frequency multiples of the power frequency. Moreover, communication signals in the substation or noise generated by corona discharges could also cause narrowband noise, but such sources normally happen at higher frequencies and can be found rarely in the FRA curves [5, 50]. The frequently occurred noises can be characterized in an FRA plot in two regions as shown in Fig. 2.10

As mentioned in Subsection 2.3.2, the amplitude of the source sinusoidal signal depends on the FRA instrument in use. According to Equation (2.3.4), the source current I_{tot} is proportional to the source voltage, so a higher source voltage could improve the noise to signal ratio and therefore minimize noise at the power frequency. However, in most cases it is impossible to completely remove the noise by increasing the output voltage of the instrument only. Besides, it is not possible to reduce the wideband noise by increasing the source voltage. To investigate the effect of the amplitude of source voltage, an example of the experimental results tested by two instruments with different source voltage amplitudes is shown is Fig. 2.11. From the figure, it can be found that the FRA result tested by the instrument with an amplitude of 10 V has less

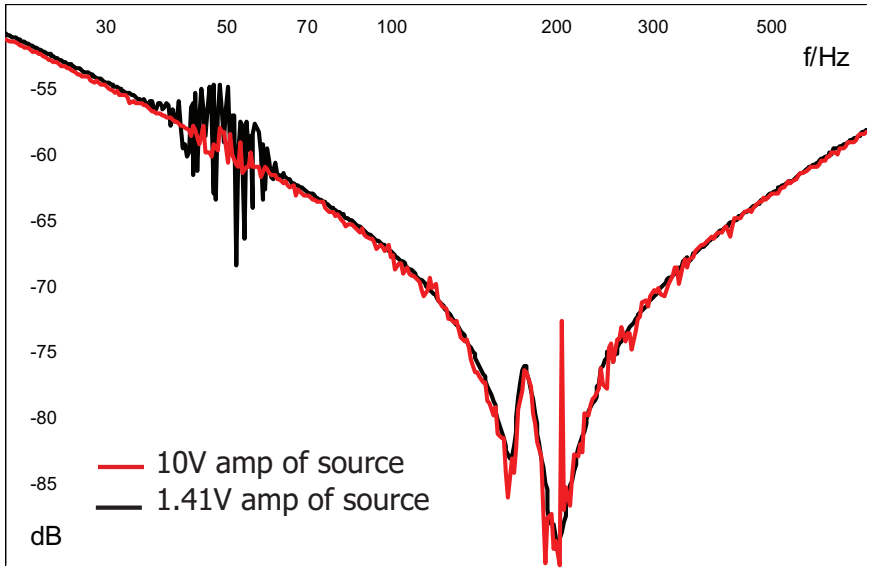

Figure 2.11: Experimental investigation of the effect of the amplitude of source voltage (reprint from [5])

power frequency noise around 50 Hz than the one with an amplitude of 1.41 V. However, the FRA curve tested by the instrument with an amplitude of 10 V shows more noticeable noise bellow -65 dB, due to a limited dynamic range of the instrument. Consequently, an FRA instrument should not only meet the requirement of responding in wide frequency range to detect subtle deformations, but also have the ability of noise suppression to ensure unambiguous diagnosis. Configurations of recently popular FRA instruments are listed in Table 2.1 [5].

Table 2.1: Configurations of recently popular FRA instruments

Instrument brand	Voltage amp	Impedance	Dynamic range
Doble: M5200/M5300	10 V	50 Ω	>90 dB
Megger: FRAX-101	10 V	50 Ω	>130 dB
Tettex: FRA 5310	6 V / 12 V	50 Ω / 1 MΩ	90 dB
OMICRON: FRAnalyzer	1.41 V	50 Ω	>120 dB

According to the recommendation of the newest FRA measurement stan-

dard [29], the FRA instrument should have the following attributes:

- The tested result should include both magnitude and phase angle of the transfer function.
- Ability of standard calibration.
- The power source should provide adequate power over the entire frequency range to ensure consistent measurement of the transfer function across the frequency range.
- The instrument should be capable of collecting a minimum of 200 measurements per decade, spaced either linearly or logarithmically.
- The characteristic impedances of the instrument and leads should be provided as a constant value and matched.
- Test leads should be coaxial cables as close to the same length as possible and less than 30 m long. Shielded test leads should have the ability to be grounded at either end.
- A three lead system, source, reference and measurement, should be used to reduce effect of leads in the measurement.
- The dynamic range of the instrument should be sufficient over the frequency range to adapt to most transformer test objects.

2.4.3 Case Study – Practical FRA Measurement

Construction of the test object

The test object, transformer-I, is a dry-type three-phase power transformer (50 kVA, 10/0.4 kV) as shown in Fig. 2.12(a). This transformer is custom-made for experimental purposes, so the first 15 discs of the HV winding in each phase can be moved or replaced. The detailed specification of the winding and core is presented in Fig. 2.13 and Table 2.2

Table 2.2: Specification of Transformer I

Model	SG10-50/10/0.4
Vector group	Yyn0
HV inner diameter	269 mm
HV outer diameter	326 mm
HV winding conductor	0.8×2 mm^2
LV inner diameter	167 mm
LV outer diameter	196 mm
LV winding conductor	3.15×8 mm^2
Isolation layer	0.15 mm

(a) (b)

Figure 2.12: Measurement set: (a) Transformer I: dry type three-phase power transformer (50 kVA, 10/0.4 kV), (b) Sweep frequency response analyzer (FRAnalyzer)

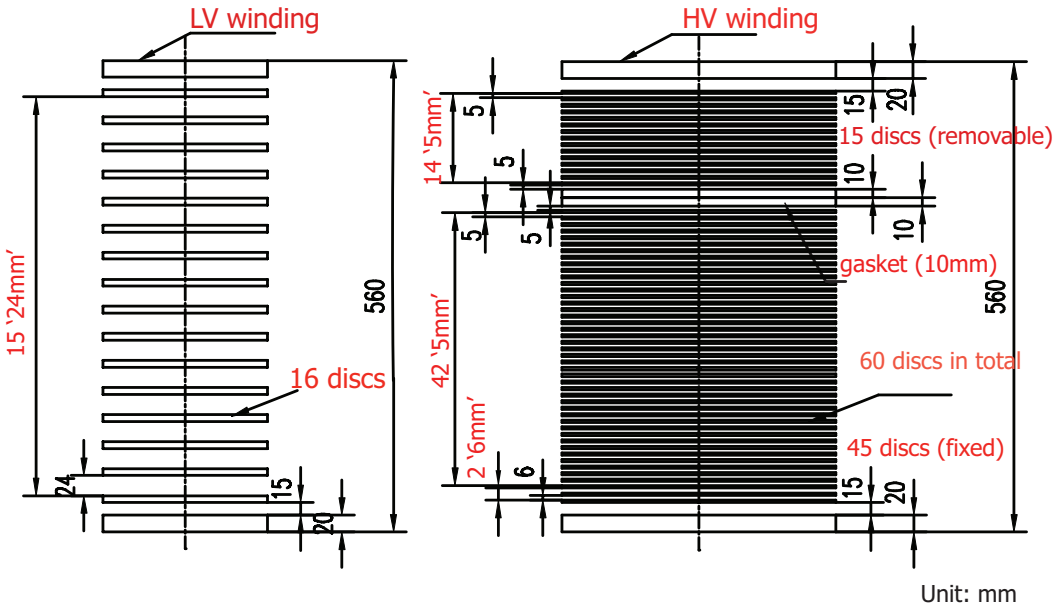

(a)

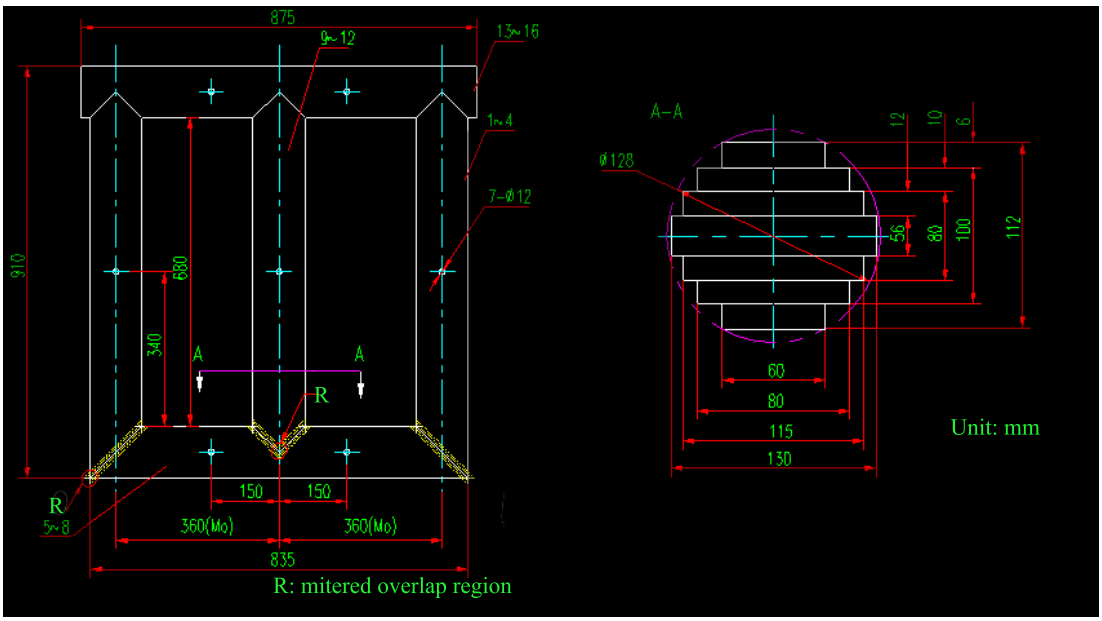

(b)

Figure 2.13: Measurement set: (a) Transformer I: dry type three-phase power transformer, (b) Sweep frequency response analyzer FRAnalyzer

Measurement

A sweep frequency response analyzer (FRAnalyzer) as shown in Fig. 2.12(b) is used for the FRA measurement in this experiment. This type of FRA instrument meets all requirements mentioned in Section 2.4.2. An innovative connection technique is applied by this instrument set to ensure reliable measurements above 1 MHz. Hence, the test frequency range of this instrument is from 10 Hz to 20 MHz. With the integral vector network analyzer toolkit, it can obtain the amplitude and phase of the voltage ratio, impedance and admittance. End-to-end open-circuit and short-circuit connections (explained in Subsection 2.4.1) are both applied in this test. Figure 2.14 to Figure 2.17 present the measured baseline (fingerprint) curves of the frequency responses. The measured frequency range is 20 Hz to 2 MHz. Figure 2.14, Figure 2.15 and Figure 2.16 are the amplitudes and phases of voltage ratio (dB), admittance (S) and impedance (Ω) transfer function respectively under the connection of end-to-end open-circuit. Figure 2.17 is the amplitude and phase of the voltage ratio transfer function in end-to-end short-circuit connection. It can be found that the curves of phase A (red) and phase C (black) are nearly identical due to the same magnetic flux path, while the curve of phase B (green) which is the middle phase is different from the others. By comparing Fig. 2.14 and Fig. 2.17, it is noticed that the magnitude of frequency response at low frequencies with LV short-circuited is much higher than the one with LV floating because of the absence of the influence of the core. Beyond that, the trend of the response curves of the same phase are similar at high frequencies.

In order to investigate the situation of minor axial winding movements, a certain number of gaskets are designed to be added between the removable and fixed sections of the HV winding to move the top section of 15 discs upwards, which is as shown in Fig. 2.18. More numbers of gaskets mean higher severity degree of the deformation.

Figure 2.19 shows the corresponding measured frequency responses across the frequency range 1 kHz - 5 MHz. It can be found that a visible trend is presented by adding the number of gaskets. The deviation of magnitude at

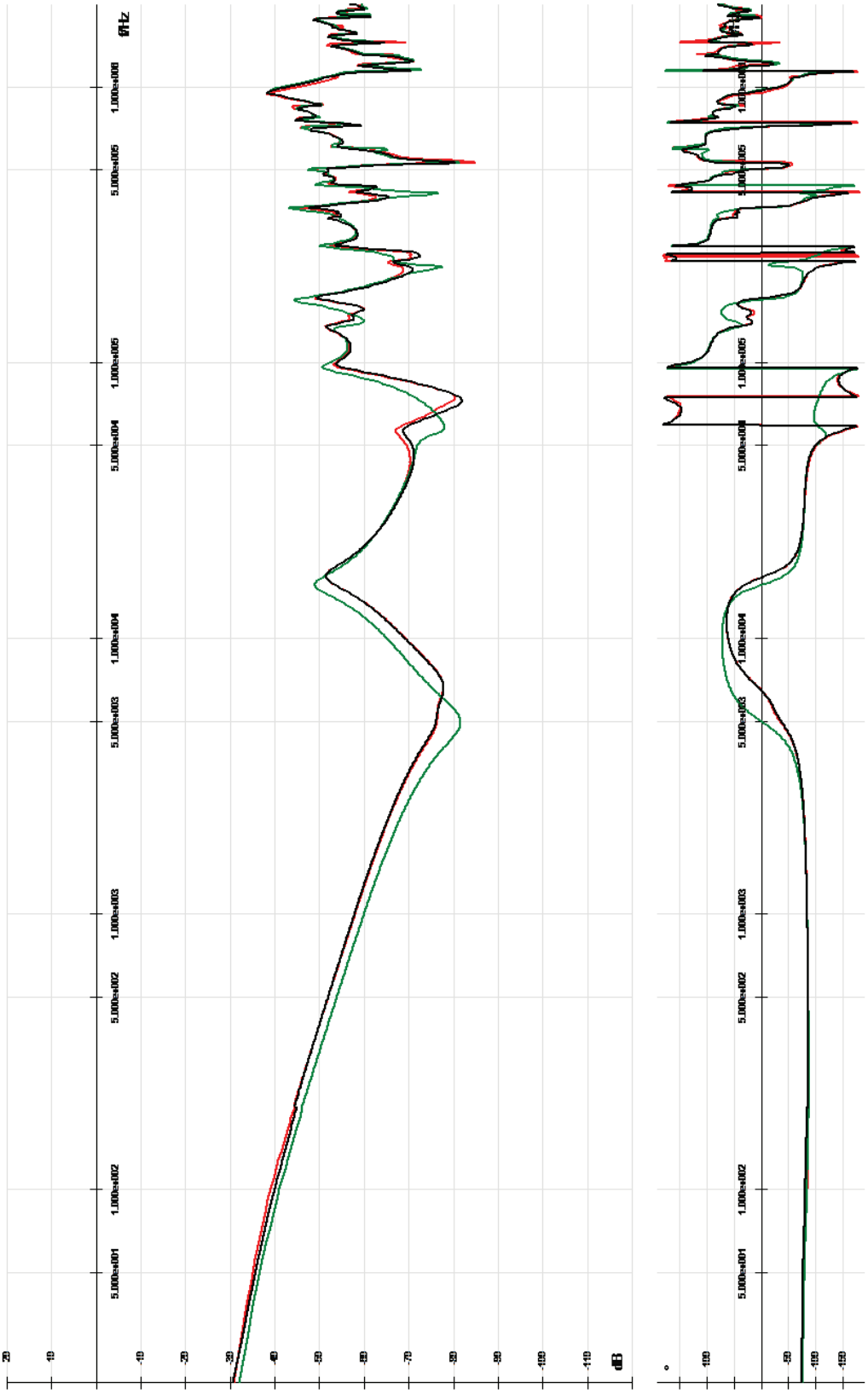

Figure 2.14: Frequency response of voltage ratio tested in end-to-end open-circuit connection. NA: Phase A, NB: Phase B, NC: Phase C. 20 Hz – 2 MHz

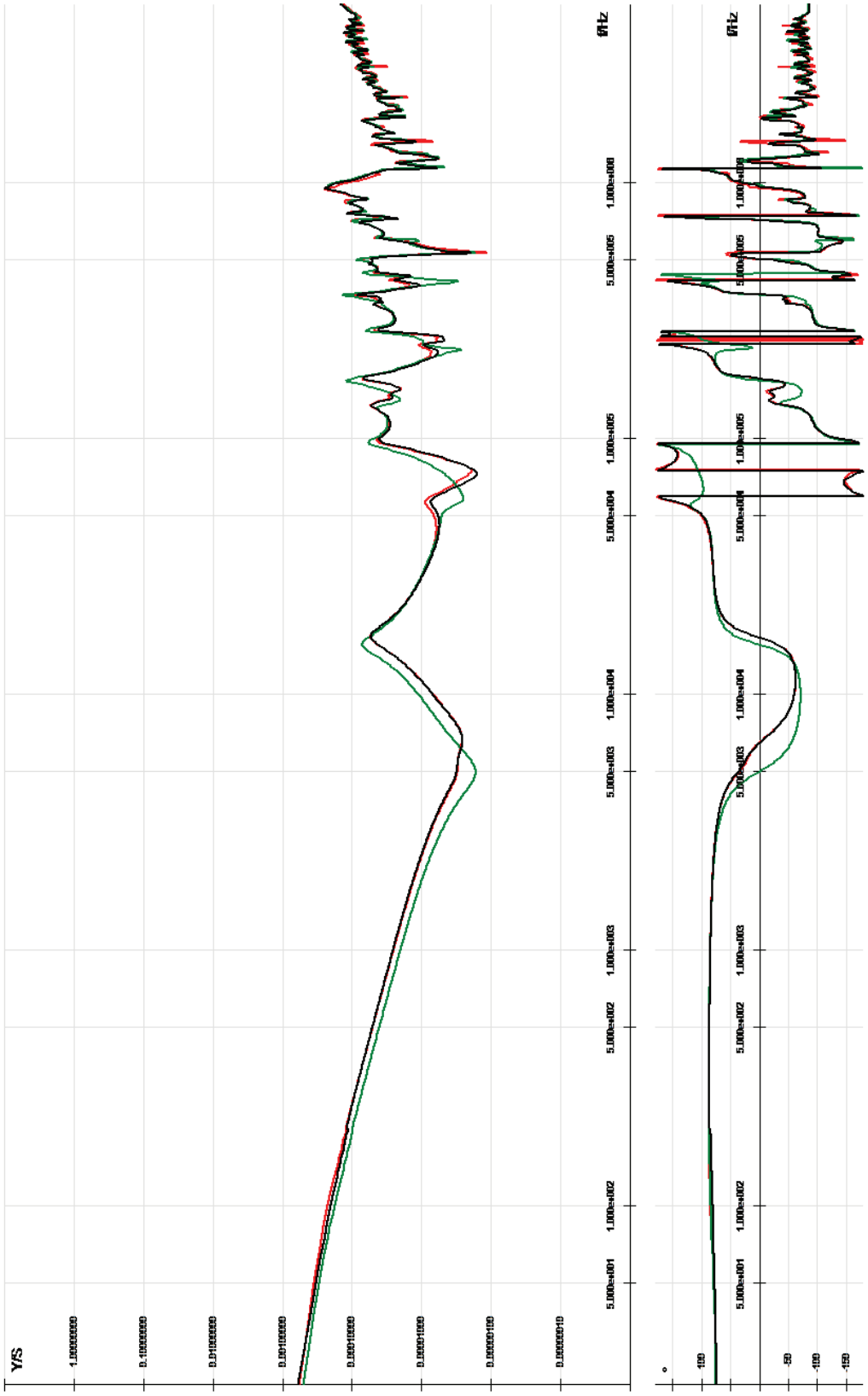

Figure 2.15: Frequency response of admittance tested in end-to-end open-circuit connection. NA: Phase A, NB: Phase B, NC: Phase C. 20 Hz – 2 MHz

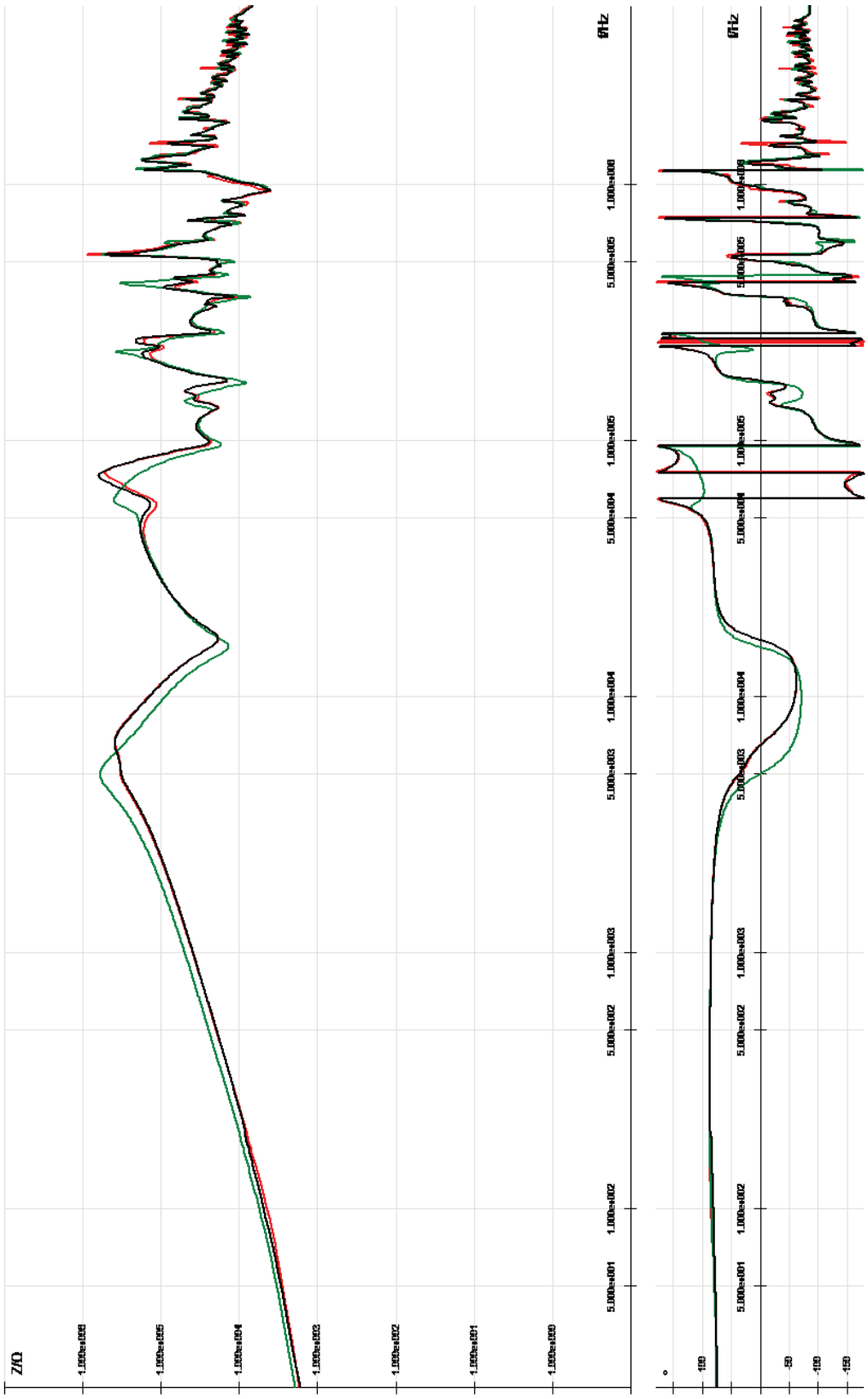

Figure 2.16: Frequency response of impedance tested in end-to-end open-circuit connection. NA: Phase A, NB: Phase B, NC: Phase C. 20 Hz – 2 MHz

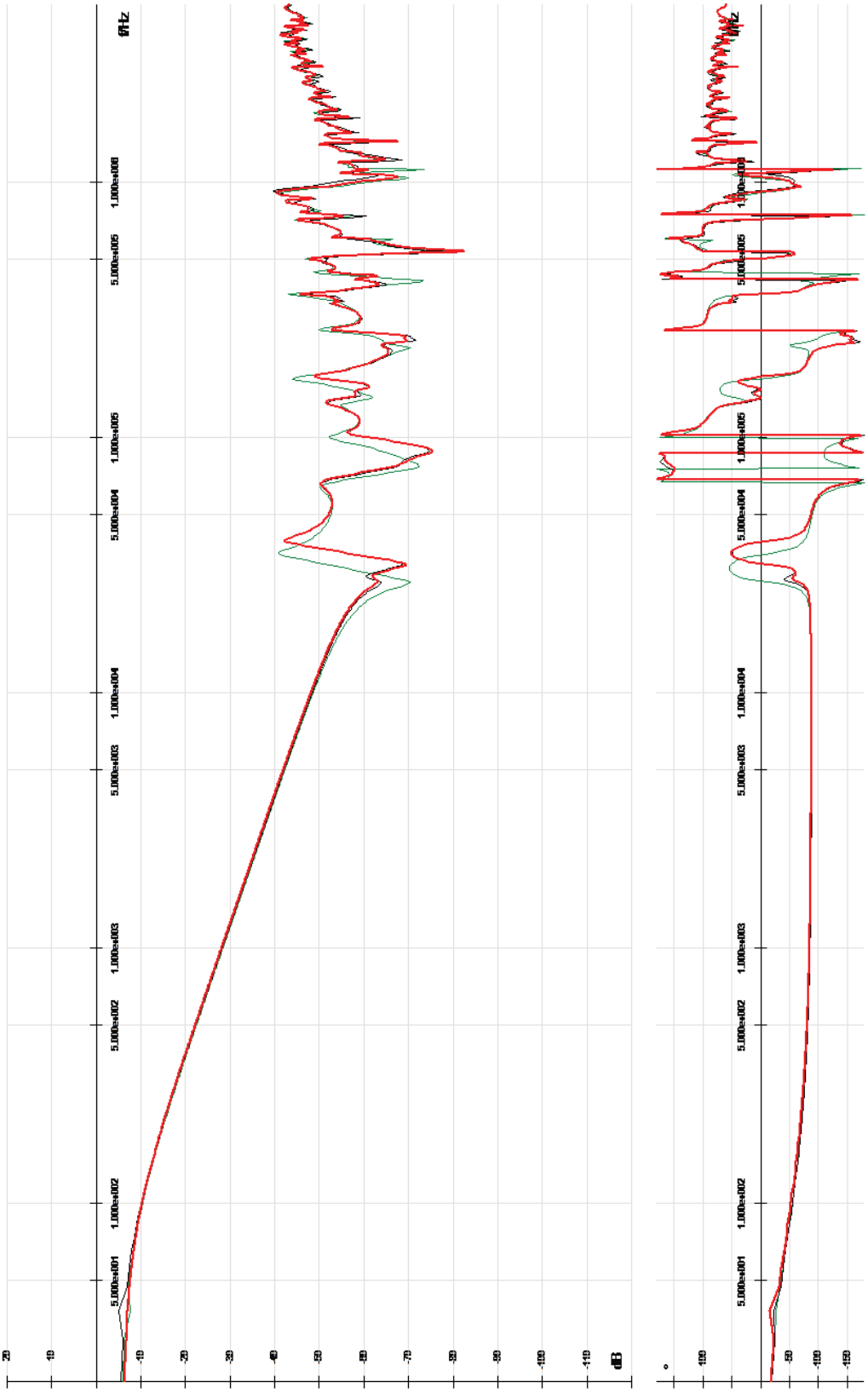

Figure 2.17: Frequency response of voltage ratio tested in end-to-end short-circuit connection. NA: Phase A, NB: Phase B, NC: Phase C. 20 Hz – 2 MHz

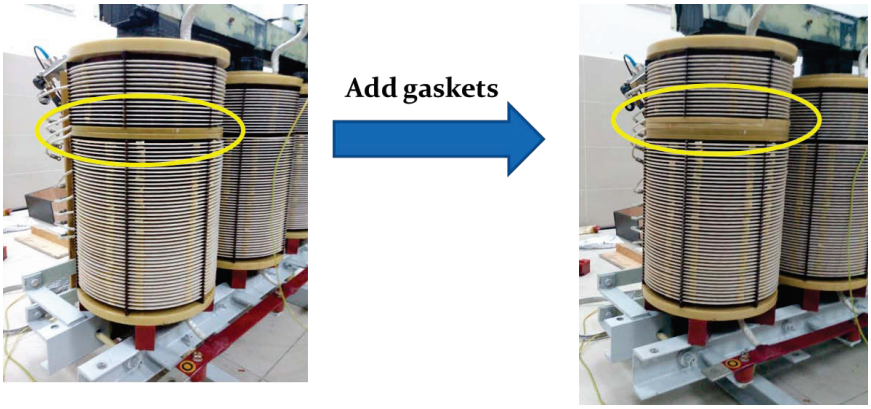

Figure 2.18: Experimental setup for minor axial displacement

resonant peaks is more detectable compared with shift of resonant peaks.

2.5 Summary

This chapter presents a review of typical failure modes of power transformers and the main reasons these failure modes, especially the influence of short circuit current. FRA technique as an effective method to detect winding deformation is introduced. By comparing two approaches of FRA, SFRA is selected as an main analysis method to investigate objectives of this thesis. Essential techniques for practical FRA measurement, especially the test connection types, are delivered. Besides, the FRA instrument attributes are discussed as well. An practical FRA measurement as well as the measured results with different transfer functions and measured connections are presented. Besides, a measurement design for testing minor axial winding movement is introduced, and the corresponding frequency responses are shown as well.

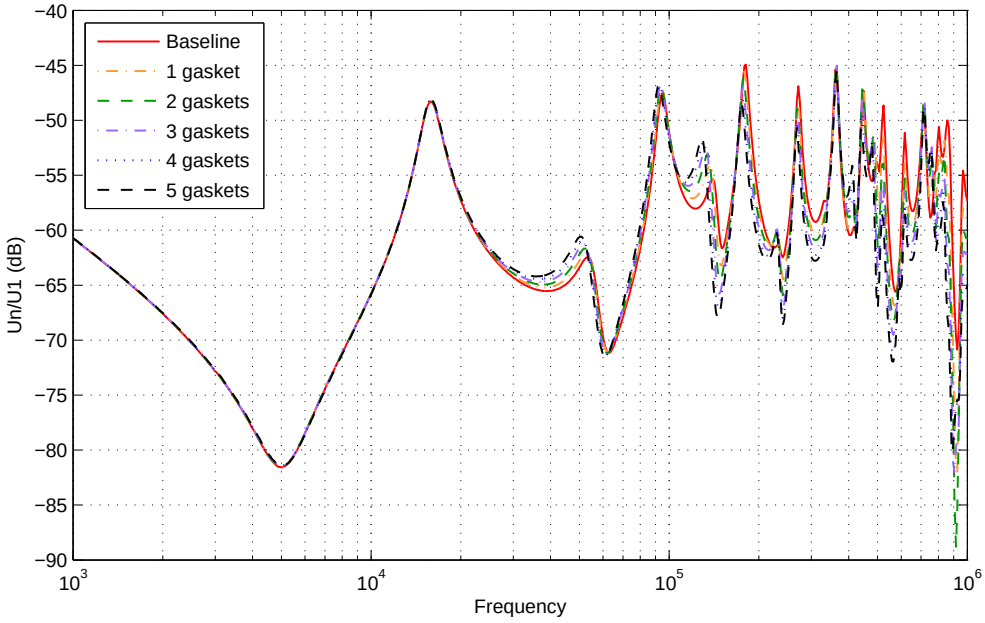

(a) 1 kHZ-1 MHz

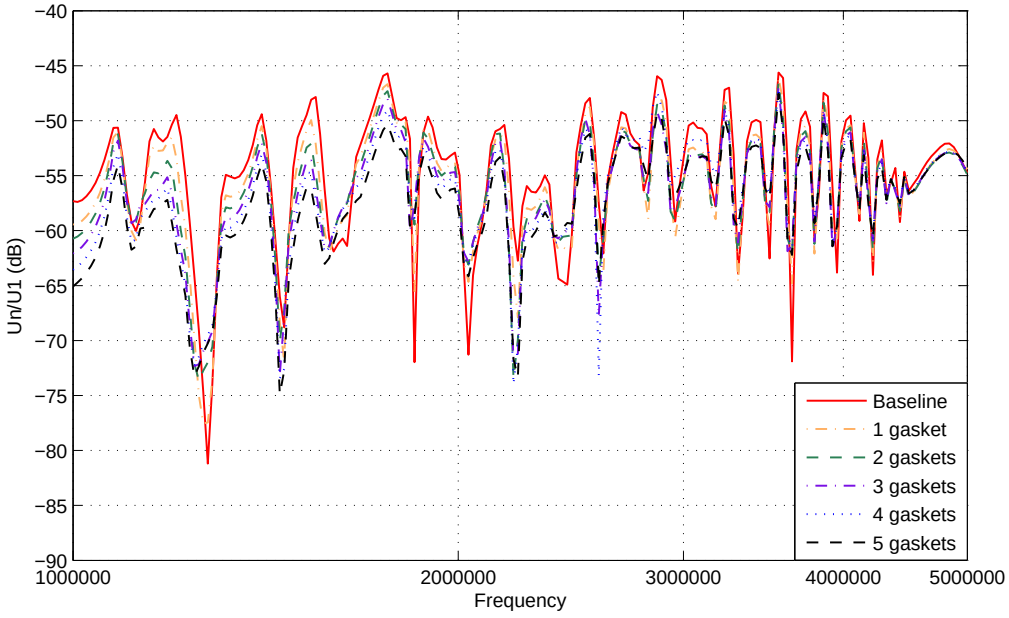

(b) 1 MHz-5 MHz

Figure 2.19: Measured frequency response for minor axial displacement. Frequency range: (a) 1 kHZ - 1 MHz (b) 1 MHz - 5 MHz

Chapter 3

High Frequency Modeling of Transformer Windings and Analytical Calculation of Winding Parameters

3.1 Introduction

As mentioned in Section 2.4, characteristics of the frequency response of a transformer winding can be assessed through practical measurements on transformers. Alternatively, the same goal can be achieved via modeling of a transformer winding to obtain frequency response curves mathematically. By constructing an analytical winding model, it is possible to estimate the influence of model parameters on failure modes and to simulate fault conditions mathematically. Moreover, these types of model offer a convenient way to study the sensitivities of frequency responses in correspondence with different failure modes by simulating several deformations with different severity. The origins of transformer modeling, which was published by Thomas [52], can be traced back to a 1902. There is a growing interest on condition monitoring for detecting incipient faults such as mechanical deformations. Therefore, research

on modeling of power transformers is still ongoing.

In this chapter, first of all a brief review of current transformer modeling methods is introduced to reveal the most suitable approach for modeling power transformers. After comparing typical modeling methods, a simplified distributed parameter model (hybrid winding model) is selected to support the interpretation of high frequency FRA introduced in next chapter. Its corresponding formulations are expressed secondly, followed by derivation of transfer functions for FRA. Finally conventional analytical expressions used to calculate parameters of winding models are presented.

3.2 Review of Transformer Modeling Methods

Transformer models are not only used in the study of frequency response of transformers, but also widely applied in other research studies, such as determining impulse stresses within windings [53], locating partial discharges [54,55] and analyzing transient overvoltages [56,57]. For the purpose of confirming the most appropriate transformer models for analyzing frequency responses at high frequencies with respect to specific transformer failure modes, a review of transformer models developed in recent years is given below.

Black-box modeling

In this case, the basic idea of black-box modeling is to rationally estimate the transfer function of transformers based on data from terminal measurements. These models are not physical models, so details of geometrical information of transformers do not need to be known. Due to this reason, many researchers attempted to develop this type of models. For example, Akiay et. al. [58] and Gustavsen et. al. [59] developed black box models based on rational approximations. In [60], Gustavsen et. al. used vector fitting algorithms to achieve a rational approximation. On the other hand, Soysal et al. [61] and Sofian et al. [9] approximated the transfer function in forms of poles and zeros representation. Another representative black-box modeling is implemented by

modal analysis by Wilcox et al. [62], [63] mainly in time domain. Following this work, Condon and Wilcox developed a methodology whereby an initial modal model can be tuned to fix experimental data [64]. The distinct advantages of this type of transformer models are that geometrical information of transformers are not required and it is feasible for implementing frequency domain models into time domain [6]. However, due to lack of physical meaning for the parameters obtained from these black box models, they are not suitable for studying geometric effects of transformers on frequency responses.

Core modeling based on the duality principle

This type of models is an core modeling based on the duality principle between magnetic and electrical circuits. It was firstly proposed by Cherry [65]. Core models based on the duality principle were widely applied to time domain transient studies of power transformers [66, 67]. Subsequently, this approach was utilized for transformer low frequency response analysis, and it was commonly applied to identify parameters of transformer cores; for instance [68–70]. However, this approach is only suitable for low frequency and intermediate frequency analysis.

Lumped parameter modeling

In the past few years, various detailed physical models have been developed, either based on self and mutual inductance or core and leakage inductance. Among them, a lumped parameter model is widely used on transformer windings, which has been applied in [33, 71–73], etc. This type of model is constructed by splitting windings into lumped segments. In practice, one or double discs in the case of a disc type windings and one or a few turns of helical type windings are represented as one unit (segment) in the model, thereby reducing the complexity of the model [73]. However, this discrete representation of windings also limits the valid frequency range of FRA. The upper limit of a typical lumped parameter model is up to 1 MHz, and it sometimes varies according to the size of the transformer.

Distributed parameter modeling

The multi-transmission line (MTL) model is another conventional physical winding model. The approach of MTL modeling was first proposed by Wagner [74]. Each turn of a winding is treated as a transmission line and decomposed into small differential segments described by distributed parameters [35,75]. By using the traveling wave theory the frequency range of accurate simulation results can be extended up to 10 MHz [75]. For computing very fast transient overvoltages (VFTOs) in transformer windings, Popov et al. [76] proposed a hybrid model which is an amalgamation of the multi-conductor transmission line model (MTLM) and the single-transmission line model (STLM). Nevertheless, a MTL model becomes very complex if a winding contains a large number of turns. A simplified distributed parameter model (hybrid model) combined with the traveling wave theory was developed in the previous research [75]. By using this winding model, the accuracy of simulation results in the high frequency range (>1 MHz) is kept but exhibits less complexity compared with the conventional turn-to-turn-based MTL model.

For FRA interpretation, physical transformer models are more competent compared with black-box models. According to the experimental results reported in [34], the frequency responses in the high frequency range (>1 MHz) are sensitive to minor winding faults. Thus, high frequency modeling has been popular in recent years. For high frequency modeling, detailed physical modeling, such as lumped parameter modeling and distributed parameter modeling, is more suitable than the core modeling based on the duality principle. Considering the accuracy at high frequencies and the complexity of establishing models, the method of simplified distributed parameter model (hybrid winding model) is used in this thesis. All formulations regarding hybrid winding model are given in next section.

3.3 Hybrid Winding Model

The hybrid winding model is developed for a continuous disc-type transformer winding, since this winding type represents the essential part of HV and MV transformer windings. The basic principle of this model is based on the wave propagation theory for a disc by regarding all turns in one disc as a single layer winding, so that each disc has similar equivalent parameter circuits. A common restriction of all physical modeling of apparatus is that constructional configurations are required. In reality, the coils of continuous disc-type windings are designed to ensure that the current along all discs of a winding flows in the same direction. Besides, the conductor length of discs near terminals in some transformers is shorter than conductor length of middle discs because of reinforced design of insulation layers near the ends of a winding. However, this method hypothesizes an equal conductor length of every disc in a winding. The traveling wave theory can be used with the assumption that the coils in each disc stretch outwards along radial direction of the winding.

3.3.1 Single Transmission Line Representation of Single Disc

The traveling wave theory can be represented in the form of the equivalent circuit as shown in Fig. 3.1. It takes a transmission line as infinite segments of length dx. l and r denote inductance and resistance per unit length, and c and G represent combined ground and inter-disc capacitances and conductances per unit length respectively. Based on Telegraphers's equations [77] and this equivalent circuit, the equations for lossy transmission lines are expressed as follows:

$$\frac{\partial u}{\partial x} = -l\frac{\partial i}{\partial t} - ri \tag{3.3.1}$$

$$\frac{\partial i}{\partial x} = -c\frac{\partial u}{\partial t} - Gu. \tag{3.3.2}$$

When treating a disc of the transformer winding which contains n turns as a transmission line, the mathematical model can be equivalent to the cir-

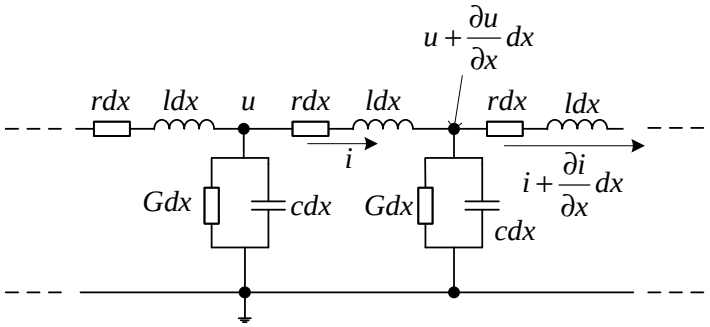

Figure 3.1: Equivalent circuit of a transmission line.

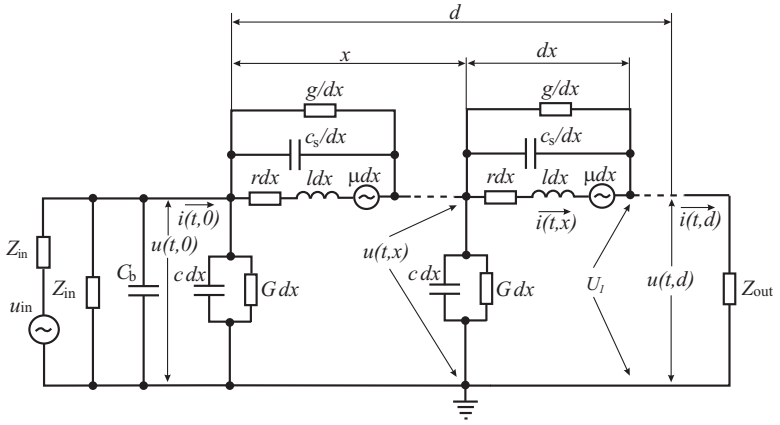

Figure 3.2: Equivalent circuit of the transmission line model for FRA.

cuit showing in Fig. 3.2. Comparing with the equivalent circuit in Fig. 3.1, the series capacitance and conductivity between turns are included. c_s and g represent the average inter-turn capacitance and conductance respectively. u_{in} denotes source signal, while Z_{in} and Z_{out} represent impedance of measurement cables. C_b corresponds to bushing capacitance, and μ denotes mutual inductance per unit length.

The branch current i_{gn} for each element of winding conductor length Δx of the n^{th} turn, flowing to 'ground' due to external capacitance and insulation conductivity, is:

$$i_{\text{gn}} = c\Delta x\frac{\partial u_n}{\partial t} + u_n \Delta x G. \tag{3.3.3}$$

u_n is the voltage of the n^{th} turn. The branch current flowing from the n^{th} turn to the $(n-1)^{\text{th}}$ turn is

$$\begin{aligned} i'_{\text{b}n} &= c_{\text{s}}\Delta x\frac{\partial(u_n-u_{n-1})}{\partial t}+(u_n-u_{n-1})\Delta x\, g \\ &= c_{\text{s}}\Delta x\frac{\partial\Delta' u_n}{\partial t}+\Delta' u_n\Delta x\, g, \end{aligned} \tag{3.3.4}$$

and current flowing to the $(n+1)^{\text{th}}$ turn is

$$\begin{aligned} i''_{\text{b}n} &= c_{\text{s}}\Delta x\frac{\partial(u_n-u_{n+1})}{\partial t}+(u_n-u_{n+1})\Delta x\, g \\ &= -c_{\text{s}}\Delta x\frac{\partial\Delta'' u_n}{\partial t}-\Delta'' u_n\Delta x\, g. \end{aligned} \tag{3.3.5}$$

Therefore, by adding (3.3.4) and (3.3.5) up, the total inter-turn current per Δx conductor length can be expressed as follows:

$$i_{\text{b}n}=i'_{\text{b}n}+i''_{\text{b}n}=-c_{\text{s}}\Delta x\frac{\partial\Delta^2 u}{\partial t}-\Delta^2 u\Delta x g, \tag{3.3.6}$$

where Δu is the voltage difference between adjacent turns and $\Delta^2 u$ denotes the difference of the Δu between successive turns.

Since only inter-turn relations are considered, the average turn length a of a conductor is assumed to be of interest:

$$\Delta x = a. \tag{3.3.7}$$

Then the second difference of voltage can be rewritten in a differential form [78]:

$$\Delta^2 u = a^2\frac{\Delta^2 u}{\Delta x^2}=a^2\frac{\partial^2 u}{\partial x}. \tag{3.3.8}$$

Substituting (3.3.8) into the sum of (3.3.3) and (3.3.6), the space derivative of the total current's decrease in the n^{th} turn is obtained as:

$$\begin{aligned} -\Delta i_n &= i_{\text{g}n}+i_{\text{b}n} \\ &= c\Delta x\frac{\partial u_n}{\partial t}+u_n\Delta xG-c_{\text{s}}\Delta x\, a^2\frac{\partial^3 u}{\partial t\,\partial x^2}-\Delta x\, ga^2\frac{\partial^2 u}{\partial x^2} \end{aligned} \tag{3.3.9}$$

or

$$\frac{\partial i}{\partial x}=-c\frac{\partial u}{\partial t}-uG+c_{\text{s}}a^2\frac{\partial^3 u}{\partial t\,\partial x^2}+ga^2\frac{\partial^2 u}{\partial x^2}. \tag{3.3.10}$$

Assume that the n^{th} turn with a self inductance per unit length of the n^{th} turn, λ, is separated from the rest of the winding, then the voltage induced by the current in it can be expressed as:

$$u_{\lambda n} = \lambda \Delta x \frac{\partial i_n}{\partial t} + r \Delta x \, i_n. \tag{3.3.11}$$

The two adjacent turns coupled by the mutual inductance μ per unit length induce a voltage in the n^{th} turn [78]:

$$\begin{aligned} u_{\mu n} &= \mu \Delta x \frac{\partial (i_{n+1} + i_{n-1})}{\partial t} \\ &= \mu \Delta x \frac{\partial \left[(i_{n+1} - i_n) - (i_n - i_{n-1}) + 2 i_n \right]}{\partial t} \\ &= 2\mu \Delta x \frac{\partial i_n}{\partial t} + \mu \Delta x \frac{\Delta^2 i_n}{\partial t}. \end{aligned} \tag{3.3.12}$$

Considering the tolerance of the calculation accuracy, the last term of (3.3.12) can be neglected. Then the total induced voltage of length Δx in n^{th} turn can be derived by considering all induced voltages by mutual inductances of other turns together with the induced voltage by self inductance, which leads to

$$\begin{aligned} u_{\text{L}n} &= \left(\lambda + \sum \mu \right) \Delta x \frac{\partial i_n}{\partial t} + r \Delta x \, i_n \\ &= L \Delta x \frac{\partial i_n}{\partial t} + r \Delta x \, i_n, \end{aligned} \tag{3.3.13}$$

where L is the self inductance of winding per unit length, derived from the total inductive effects between all turns. To simplify the calculation, L can be obtained as the self inductance of the entire winding divided by its total length.

Since the total voltage of n^{th} turn is decreased by $u_{\text{L}n}$, the decreased value $-\Delta u_n$ can be derived as follows:

$$-\Delta u_n = L \Delta x \frac{\partial i_n}{\partial t} + r \Delta x \, i_n, \tag{3.3.14}$$

and the voltage space derivative along the winding transforms into:

$$\frac{\partial u}{\partial x} = -L \frac{\partial i}{\partial t} - r i. \tag{3.3.15}$$

In order to transfer the expressions (3.3.10) and (3.3.15) into frequency domain, Laplace Transform is applied. Assume the initial conditions are:

$$i(t=0,x) = 0, \tag{3.3.16}$$

$$u(t=0,x) = 0. \tag{3.3.17}$$

The Laplace transforms of the space derivatives are:

$$\mathcal{L}\left[\frac{\partial u}{\partial x}\right] = \frac{\partial U(s,x)}{\partial x}, \tag{3.3.18}$$

$$\mathcal{L}\left[\frac{\partial i}{\partial x}\right] = \frac{\partial I(s,x)}{\partial x}, \tag{3.3.19}$$

$$\mathcal{L}\left[\frac{\partial^2 u}{\partial x^2}\right] = \frac{\partial U^2(s,x)}{\partial x^2}, \tag{3.3.20}$$

and those of the time derivatives are:

$$\mathcal{L}\left[\frac{\partial u}{\partial t}\right] = sU(s,x) - u(0,x) = sU(s,x), \tag{3.3.21}$$

$$\mathcal{L}\left[\frac{\partial i}{\partial t}\right] = sI(s,x) - i(0,x) = sI(s,x), \tag{3.3.22}$$

$$\begin{aligned}\mathcal{L}\left[\frac{\partial^3 u}{\partial t \partial x^2}\right] &= \mathcal{L}\left[\frac{\partial(\partial^2 u/\partial x^2)}{\partial t}\right] \\ &= s\mathcal{L}\left[\frac{\partial^2 u}{\partial x^2}\right] - \left.\frac{\partial^2 u}{\partial x^2}\right|_{t=0} \\ &= s\mathcal{L}\left[\frac{\partial^2 u}{\partial x^2}\right] \\ &= s\frac{\partial U^2(s,x)}{\partial x^2}.\end{aligned} \tag{3.3.23}$$

Therefore, (3.3.10) and (3.3.15) are transformed into frequency domain as follows:

$$\frac{\partial U(s,x)}{\partial x} = -LsI(s,x) - rI(s,x), \tag{3.3.24}$$

$$\begin{aligned}\frac{\partial I(s,x)}{\partial x} = &- C_{\mathrm{g}}\, sU(s,x) - G_{\mathrm{g}} U(s,x) \\ &+ Ka^2 s\frac{\partial^2 U(s,x)}{\partial x^2} + g\, a^2 \frac{\partial^2 U(s,x)}{\partial x^2},\end{aligned} \tag{3.3.25}$$

where $U(s,x)$ and $I(s,x)$ are the Laplace transforms of voltage $u(t,x)$ and current $i(t,x)$ correspondingly, L and r are self inductance and resistance of

windings per unit length, C_g and G_g are shunt capacitance and conductance of windings per unit length, K and g are inter-turn capacitance and conductance of winding conductors per unit length.

Thus, the derived equations (3.3.24) and (3.3.25) describe the injected signal propagation along a uniform winding disc in frequency domain.

3.3.2 Multiple Transmission Line Representation of a Transformer Winding

Mathematical Derivation

Based on equations (3.3.24) and (3.3.25) derived from a single disc equivalent circuit, the model of a disc-type transformer winding which contains several discs can be derived involving inter-disc capacitances and conductances. Considering the inter-disc capacitances and conductances on the basis of the equivalent circuit shown in Fig. 3.2, an entire winding can be made equivalent to the circuit in Fig. 3.3 [4]. The circuit parameters are defined as follows, where 'average' means the corresponding value per unit length:

K_i, g_i	average inter-turn capacitance and conductance of the i^{th} disc;
Z_{inp}, Z_{out}	impedances of measurement cables;
C_i, G_i	average ground capacitance and conductance;
L_i, $M_{i(i+1)}$	average self and mutual inductance;
$C_{\text{d}i(i+1)}$	average inter-disc capacitance between the i^{th} and $(i+1)^{th}$ discs;
$G_{\text{d}i(i+1)}$	average inter-disc conductance between the i^{th} and $(i+1)^{th}$ discs.

The equations for the first disc of a winding are derived as:

$$\begin{aligned}
\frac{\partial U_1(s,x)}{\partial x} &= -(L_1 s + r_1) I_1(s,x) - sM_{12} I_2(s,x) - \ldots - sM_{1n} I_n(s,x) \\
&= -Z_1 I_1(s,x) - sM_{12} I_2(s,x) - \ldots - sM_{1n} I_n(s,x), \qquad (3.3.26) \\
\frac{\partial I_1(s,x)}{\partial x} &= -C_1 s U_1(s,x) - G_1 U_1(s,x) + a^2 K_1 s \frac{\partial^2 U_1(s,x)}{\partial x^2} + a^2 g_1 \frac{\partial^2 U_1(s,x)}{\partial x^2} \\
&\quad -C_{\text{d12}}\, s[U_1(s,x) - U_2(s,x)] - G_{\text{d12}}[U_1(s,x) - U_2(s,x)] \\
&= -Y_1 U_1(s,x) + a^2 Y_{\text{s1}} \frac{\partial^2 U_1(s,x)}{\partial x^2} + Q_{12} U_2(s,x), \qquad (3.3.27)
\end{aligned}$$

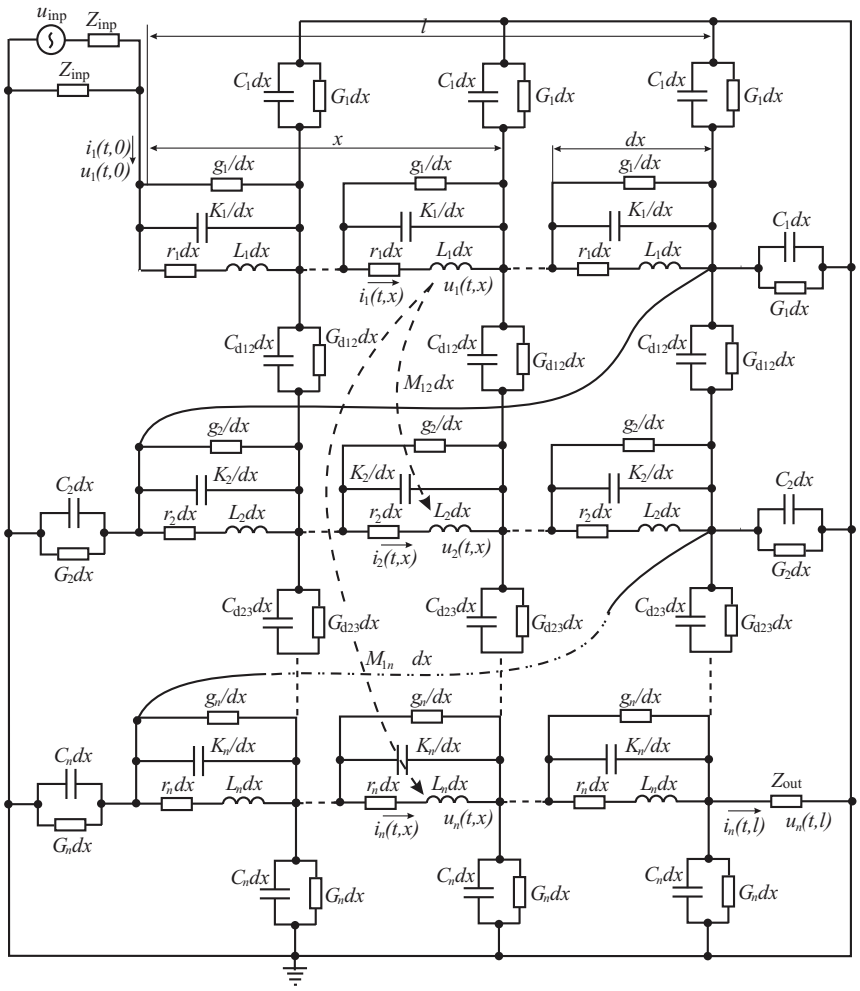

Figure 3.3: The equivalent circuit of a disc-type transformer winding [4]

where

$$\begin{aligned} Y_1 &= (C_1 + C_{\mathrm{d12}})\, s + (G_1 + G_{\mathrm{d12}}) \\ Y_{\mathrm{s1}} &= K_1 s + g_1 \\ Q_{12} &= C_{\mathrm{d12}}\, s + G_{\mathrm{d12}}. \end{aligned}$$

The expressions of the i^{th} $(i = 2, \ldots, n-1)$ disc can be described as:

$$\begin{aligned}\frac{\partial U_i(s,x)}{\partial x} &= -Z_i I_i(s,x) - sM_{i1} I_1(s,x) - \ldots - sM_{i,i-1} I_{i-1}(s,x) \\ &\quad -sM_{i,i+1} I_{i+1}(s,x) - \ldots - sM_{in} I_n(s,x) \qquad (3.3.28) \\ \frac{\partial I_i(s,x)}{\partial x} &= -Y_i U_i(s,x) + a^2 Y_{\text{si}} \frac{\partial^2 U_i(s,x)}{\partial x^2} \\ &\quad +Q_{(i-1)i} U_{i-1}(s,x) + Q_{i(i+1)} U_{i+1}(s,x). \qquad (3.3.29)\end{aligned}$$

The expressions for the last disc are:

$$\begin{aligned}\frac{\partial U_n(s,x)}{\partial x} &= -Z_n I_n(s,x) - sM_{n1} I_1(s,x) \\ &\quad - \ldots - sM_{n(n-1)} I_{n-1}(s,x) \qquad (3.3.30) \\ \frac{\partial I_n(s,x)}{\partial x} &= -Y_n U_n(s,x) + a^2 Y_{\text{sn}} \frac{\partial^2 U_n(s,x)}{\partial x^2} \\ &\quad +Q_{(n-1)n} U_{n-1}(s,x). \qquad (3.3.31)\end{aligned}$$

Equations (3.3.26)$\sim$(3.3.31) can be combined together to form the following matrix equations:

$$\begin{aligned}\frac{\partial}{\partial x}\mathbf{U}(s,x) &= -\mathbf{Z}\,\mathbf{I}(s,x) \qquad (3.3.32) \\ \frac{\partial}{\partial x}\mathbf{I}(s,x) &= -\mathbf{Q}\,\mathbf{U}(s,x) + \mathbf{Y_S}\frac{\partial^2}{\partial x^2}\mathbf{U}(s,x), \qquad (3.3.33)\end{aligned}$$

where

$$\mathbf{U}(s,x) = \begin{bmatrix} U_1(s,x) \\ \vdots \\ U_i(s,x) \\ \vdots \\ U_n(s,x) \end{bmatrix}, \mathbf{I}(s,x) = \begin{bmatrix} I_1(s,x) \\ \vdots \\ I_i(s,x) \\ \vdots \\ I_n(s,x) \end{bmatrix}, \qquad (3.3.34)$$

$$\mathbf{Z} = \begin{bmatrix} Z_1 & sM_{12} & \cdots & sM_{1n} \\ sM_{21} & Z_2 & \ddots & \vdots \\ \vdots & \ddots & \ddots & sM_{(n-1)n} \\ sM_{n1} & \cdots & sM_{n(n-1)} & Z_n \end{bmatrix}, \tag{3.3.35}$$

$$\mathbf{Q} = \begin{bmatrix} Y_1 & -Q_{12} & \cdots & 0 \\ -Q_{21} & Y_2 & \ddots & \vdots \\ \vdots & \ddots & \ddots & -Q_{(n-1)n} \\ 0 & \cdots & -Q_{n(n-1)} & Y_n \end{bmatrix}, \tag{3.3.36}$$

$$\mathbf{Y_S} = \begin{bmatrix} a^2Y_{s1} & 0 & \cdots & 0 \\ 0 & a^2Y_{s2} & \ddots & 0 \\ \vdots & \ddots & \ddots & \vdots \\ 0 & 0 & \ddots & a^2Y_{sn} \end{bmatrix}. \tag{3.3.37}$$

The impedances and admittances Z, Y, Y_s of every disc and the inter-disc admittances Q per unit length are defined as follows:

for $i = 1, \ldots, n$

$$Z_i = L_i s + r_i \tag{3.3.38}$$

$$Y_{si} = K_i s + g_i, \tag{3.3.39}$$

for $i = 2, \ldots, n-1$,

$$Y_i = (C_i + C_{\mathrm{d}i-1,i} + C_{\mathrm{d}i,i+1})s + (G_i + G_{\mathrm{d}i-1,i} + G_{\mathrm{d}i,i+1}) \tag{3.3.40}$$

$$Q_{i-1,i} = C_{\mathrm{d}i-1,i}s + G_{\mathrm{d}i-1,i} \tag{3.3.41}$$

$$Q_{i,i+1} = C_{\mathrm{d}i,i+1}s + G_{\mathrm{d}i,i+1}, \tag{3.3.42}$$

$$\tag{3.3.43}$$

and

$$Y_n = (C_n + C_{\mathrm{d}n-1,n})s + (G_n + G_{\mathrm{d}n-1,n}). \tag{3.3.44}$$

Equations (3.3.32) and (3.3.33) are re-arranged into a matrix form as follows:

$$\begin{aligned} \frac{\partial \mathbf{U}(s,x)}{\partial x} &= -\mathbf{Z}\ \mathbf{I}(s,x), \\ \frac{\partial}{\partial x}\mathbf{I}(s,x) &= -(\mathbf{II} + \mathbf{Y_S}\mathbf{Z})^{-1}\mathbf{Q}\mathbf{U}(s,x) = -\mathbf{Y}\mathbf{U}, \end{aligned} \tag{3.3.45}$$

where $\mathbf{II}$ is the $n \times n$ identity matrix and

$$\mathbf{Y} = (\mathbf{II} + \mathbf{Y_S Z})^{-1}\mathbf{Q}. \tag{3.3.46}$$

The equations (3.3.45) also can be written as:

$$\frac{\partial}{\partial x}\begin{bmatrix} \mathbf{U}(s,x) \\ \mathbf{I}(s,x) \end{bmatrix} = \mathbf{A}\begin{bmatrix} \mathbf{U}(s,x) \\ \mathbf{I}(s,x) \end{bmatrix}, \tag{3.3.47}$$

where

$$\mathbf{A} = \begin{bmatrix} \mathbf{0} & -\mathbf{Z} \\ -\mathbf{Y} & \mathbf{0} \end{bmatrix} \tag{3.3.48}$$

with $\mathbf{0}$ the $n \times n$ zero matrix.

In order to solve (3.3.47) and incorporate the boundary conditions, let

$$\mathbf{X} = \begin{bmatrix} \mathbf{U} \\ \mathbf{I} \end{bmatrix}, \tag{3.3.49}$$

then (3.3.47) becomes

$$\frac{\partial \mathbf{X}}{\partial x} = \mathbf{A}\mathbf{X}. \tag{3.3.50}$$

Assume s is a constant, then the solution of (3.3.50) can be derived from an n-dimensional homogeneous ordinary differential equation (3.3.51) (ODE).

$$\frac{d}{dt}\mathbf{X}(t) = \mathbf{A}\mathbf{X}(t), \tag{3.3.51}$$

where

$$\mathbf{X}(t) = \begin{bmatrix} x_1(t) \\ \vdots \\ x_i(t) \\ \vdots \\ x_n(t) \end{bmatrix}, \mathbf{A} = \begin{bmatrix} a_{11} & \cdots & a_{1i} & \cdots & a_{1n} \\ \vdots & \ddots & \vdots & \ddots & \vdots \\ a_{i1} & \cdots & a_{ii} & \cdots & a_{in} \\ \vdots & \ddots & \vdots & \ddots & \vdots \\ a_{n1} & \cdots & a_{ni} & \cdots & a_{nn} \end{bmatrix}. \tag{3.3.52}$$

For the scalar version of (3.3.51):

$$\frac{d}{dt}x(t) = ax(t) \tag{3.3.53}$$

with a prescribed initial state $x(t_0)$, the solution is

$$x_{\mathrm{h}}(t) = e^{a(t-t_0)}x(t_0) = \phi(t-t_0)x(t_0) \tag{3.3.54}$$

where $\phi(t) = e^{at}$ is called the state-transition function.

This result can be extended to n-dimensional differential equations characterized by (3.3.51) and the solution can be obtained as:

$$\mathbf{X}(t) = \mathbf{\Phi}(t-t_0)\mathbf{X}(t_0), \tag{3.3.55}$$

where $\mathbf{\Phi}(t)$ is the $n \times n$ state-transition matrix and $\mathbf{\Phi}(t) = \mathbf{e}^{\mathbf{A}t}$.

$\mathbf{\Phi}(t)$ has the properties:

$$\mathbf{\Phi}(0) = \mathbf{II} \tag{3.3.56}$$

$$\mathbf{\Phi}^{-1}(t) = \mathbf{\Phi}(-t). \tag{3.3.57}$$

Thus, according to (3.3.55), the solution of (3.3.47) can be obtained:

$$\begin{aligned}\begin{bmatrix}\mathbf{U}(s,x_2)\\ \mathbf{I}(s,x_2)\end{bmatrix} &= \mathbf{\Phi}(x_2-x_1)\begin{bmatrix}\mathbf{U}(s,x_1)\\ \mathbf{I}(s,x_1)\end{bmatrix}\\ &= \begin{bmatrix}\mathbf{\Phi}_{11}(x_2-x_1) & \mathbf{\Phi}_{12}(x_2-x_1)\\ \mathbf{\Phi}_{21}(x_2-x_1) & \mathbf{\Phi}_{22}(x_2-x_1)\end{bmatrix}\begin{bmatrix}\mathbf{U}(s,x_1)\\ \mathbf{I}(s,x_1)\end{bmatrix}\end{aligned} \tag{3.3.58}$$

where $\mathbf{\Phi}$ is the $2n \times 2n$ chain parameter matrix whereas matrices $\mathbf{\Phi}_{ij}$ are $n \times n$ chain parameter matrices. When $x_1 = 0$ and $x_2 = l$, the solution of (3.3.47) at the end of the discs is given as:

$$\begin{bmatrix}\mathbf{U}(s,l)\\ \mathbf{I}(s,l)\end{bmatrix} = \mathbf{\Phi}(l)\begin{bmatrix}\mathbf{U}(s,0)\\ \mathbf{I}(s,0)\end{bmatrix} = \begin{bmatrix}\mathbf{\Phi_{11}}(l) & \mathbf{\Phi_{12}}(l)\\ \mathbf{\Phi_{21}}(l) & \mathbf{\Phi_{22}}(l)\end{bmatrix}\begin{bmatrix}\mathbf{U}(s,0)\\ \mathbf{I}(s,0)\end{bmatrix} \tag{3.3.59}$$

and

$$\begin{aligned}\mathbf{\Phi}(l) &= \mathbf{e}^{\mathbf{A}l} = \mathbf{e}^{\mathbf{A}(a_p+\ldots+a_2+a_1)}\\ &= \mathbf{e}^{\mathbf{A}a_p} \times \cdots \times \mathbf{e}^{\mathbf{A}a_2} \times \mathbf{e}^{\mathbf{A}a_1}\end{aligned} \tag{3.3.60}$$

where a_i is the length of the i^{th} turn and p is the number of turns per disc.

3.4 Transfer Functions For Frequency Response Analysis

The transfer functions with respect to the mathematical winding model described in Section 3.3 are now calculated for frequency response analysis.

In order to derive the expressions for transfer functions, equation (3.3.59) is rearranged as below [79]:

$$\begin{bmatrix} \mathbf{I}(s,0) \\ \mathbf{I}(s,l) \end{bmatrix} = \begin{bmatrix} \boldsymbol{\Upsilon}_{\mathbf{11}}(l) & \boldsymbol{\Upsilon}_{\mathbf{12}}(l) \\ \boldsymbol{\Upsilon}_{\mathbf{21}}(l) & \boldsymbol{\Upsilon}_{\mathbf{22}}(l) \end{bmatrix} \cdot \begin{bmatrix} \mathbf{U}(s,0) \\ \mathbf{U}(s,l) \end{bmatrix}, \tag{3.4.1}$$

where

$$\begin{aligned} \boldsymbol{\Upsilon}_{\mathbf{11}}(l) &= -\boldsymbol{\Phi}_{\mathbf{12}}(l)^{-1}\, \boldsymbol{\Phi}_{\mathbf{11}}(l), \\ \boldsymbol{\Upsilon}_{\mathbf{12}}(l) &= \boldsymbol{\Phi}_{\mathbf{12}}(l)^{-1}, \\ \boldsymbol{\Upsilon}_{\mathbf{21}}(l) &= \boldsymbol{\Phi}_{\mathbf{21}}(l) - \boldsymbol{\Phi}_{\mathbf{22}}(l)\, \boldsymbol{\Phi}_{\mathbf{12}}(l)^{-1}\, \boldsymbol{\Phi}_{\mathbf{11}}(l), \\ \boldsymbol{\Upsilon}_{\mathbf{22}}(l) &= \boldsymbol{\Phi}_{\mathbf{22}}(l)\, \boldsymbol{\Phi}_{\mathbf{12}}(l)^{-1}. \end{aligned} \tag{3.4.2}$$

The boundary conditions for equation (3.4.1) are derived from Fig. 3.3:

$$\begin{aligned} U_{i+1}(s,0) &= U_i(s,l), \quad \text{for} \quad i = 1, \ldots, n-1, \\ I_{i+1}(s,0) &= I_i(s,l), \quad \text{for} \quad i = 1, \ldots, n-1. \end{aligned} \tag{3.4.3}$$

Combining these boundary conditions, equation (3.4.1) can be simplified into the form:

$$\begin{bmatrix} I_1(s,0) \\ I_2(s,0) \\ \vdots \\ I_n(s,0) \\ I_2(s,0) \\ \vdots \\ I_n(s,0) \\ I_n(s,l) \end{bmatrix} = \begin{bmatrix} & & \\ & \boldsymbol{\Upsilon}(l) & \\ & & \end{bmatrix} \cdot \begin{bmatrix} U_1(s,0) \\ U_2(s,0) \\ \vdots \\ U_n(s,0) \\ U_2(s,0) \\ \vdots \\ U_n(s,0) \\ U_n(s,l) \end{bmatrix}, \tag{3.4.4}$$

where $\boldsymbol{\Upsilon}(l)$ is an $2n \times 2n$ chain parameter matrix.

It can be found that $U_i = U_{i+n}$ for $i = 1, \ldots, n-1$ in $\mathbf{U}$ which is an $2n \times 1$ matrix. Equation (3.4.4) can therefore be simplified by summing up the following columns of matrix $\boldsymbol{\Upsilon}(l)$:

$$\Upsilon_{(:,i+1)} + \Upsilon_{(:,i+n)}, \quad \text{for } i = 1, \ldots, n-1. \tag{3.4.5}$$

Therefore, (3.4.4) becomes:

$$\begin{bmatrix} I_1(s,0) \\ I_2(s,0) \\ \vdots \\ I_n(s,0) \\ I_2(s,0) \\ \vdots \\ I_n(s,0) \\ I_n(s,l) \end{bmatrix} = \begin{bmatrix} \\ \\ \\ \boldsymbol{\Upsilon}'(l) \\ \\ \\ \\ \end{bmatrix} \cdot \begin{bmatrix} U_1(s,0) \\ U_2(s,0) \\ \vdots \\ U_n(s,0) \\ U_n(s,l) \end{bmatrix}, \tag{3.4.6}$$

where $\boldsymbol{\Upsilon}'(l)$ is a $2n \times (n+1)$ matrix, and the new $\mathbf{U}$ is and $(n+1) \times 1$ matrix.

In matrix $\mathbf{I}$ from equation (3.4.6), it can be seen that $I_i = I_{i+n}$ for $i = 1, \ldots, n-1$. Therefore, equation (3.4.6) can be simplified by subtracting the following rows of $\boldsymbol{\Upsilon}'(l)$:

$$\Upsilon'_{(i+1,:)} - \Upsilon'_{(i+n,:)}, \quad \text{for } i = 1, \ldots, n-1. \tag{3.4.7}$$

Hence, the simplified equation is showing as follows:

$$\begin{bmatrix} I_1(s,0) \\ 0 \\ \vdots \\ 0 \\ I_n(s,l) \end{bmatrix} = \begin{bmatrix} \\ \\ \boldsymbol{\Upsilon}''(l) \\ \\ \\ \end{bmatrix} \cdot \begin{bmatrix} U_1(s,0) \\ U_2(s,0) \\ \vdots \\ U_n(s,0) \\ U_n(s,l) \end{bmatrix}, \tag{3.4.8}$$

where $\boldsymbol{\Upsilon}''(l)$ is an $(n+1) \times (n+1)$ matrix, and the new $\mathbf{I}$ is an $(n+1) \times 1$ matrix. Mark the inversion of $\boldsymbol{\Upsilon}''(l)$ with $\boldsymbol{\Omega}(l)$, then equation (3.4.8) can be

converted to:

$$\begin{bmatrix} U_1(s,0) \\ U_2(s,0) \\ \vdots \\ U_n(s,0) \\ U_n(s,l) \end{bmatrix} = \begin{bmatrix} & & \\ & \mathbf{\Omega}(l) & \\ & & \end{bmatrix} \cdot \begin{bmatrix} I_1(s,0) \\ 0 \\ \vdots \\ 0 \\ I_n(s,l) \end{bmatrix}, \tag{3.4.9}$$

where $\mathbf{\Omega}(l) = [\mathbf{\Upsilon}''(l)]^{-1}$.

Open-circuit measurement is one of the most frequently used measurement mehtod to obtain the FRA magnitude of a winding. In order to derive the corresponding expression for the transfer function of the FRA magnitude in modeling, the following terminal condition is applied:

$$U_n(s,l) = Z_{\text{out}} I_n(s,l). \tag{3.4.10}$$

Together with this terminal condition, the transfer function of the FRA magnitude in the model can be derived as the ratio of $U_n(s,l)$ and $U_1(s,0)$:

$$H(s) = \frac{U_n(s,l)}{U_1(s,0)} = \frac{\Omega_{(n+1,1)} Z_{\text{out}}}{\Omega_{(1,1)} \left(Z_{\text{out}} - \Omega_{(n+1,n+1)}\right) + \Omega_{(1,n+1)} \Omega_{(n+1,1)}}. \tag{3.4.11}$$

Considering the grounded neutral end and measurements at the high voltage end, the terminal voltage is set to $U_n(s,l) = 0$. Then the transfer function of input impedance can be derived [75]:

$$Z_{\text{inp}}(s) = \frac{U_1(s,0)}{I_1(s,0)} = \frac{\Omega_{(1,1)}\Omega_{(n+1,n+1)} - \Omega_{(1,n+1)}\Omega_{(n+1,1)}}{\Omega_{(n+1,n+1)}}. \tag{3.4.12}$$

The transfer function of admittance can be derived as follows:

$$H(s) = \frac{I_n(s,l)}{U_1(s,0)} = \frac{\Omega_{(n+1,1)}}{\Omega_{(1,n+1)}\Omega_{(n+1,1)} - \Omega_{(1,1)}(\Omega_{(n+1,n+1)} - Z_{out})}, \tag{3.4.13}$$

where $I_n(s,l)$ is the terminal current.

High Voltage Bushing

To investigate the effect of high voltage bushing on the FRA test, an equivalent circuit of the bushing (see Fig.3.4) is added to the winding model [34].

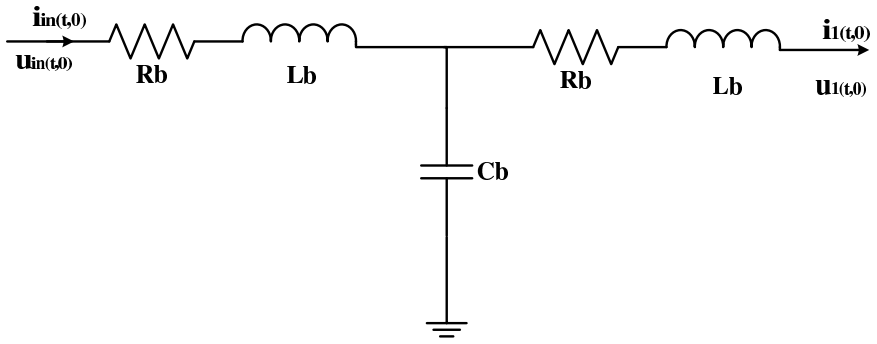

Figure 3.4: Bushing Equivalent Circuit

From the equivalent circuit, it seems that the input impedance needs to be updated. Let $X = U_1(s,0)/I_1(s,0)$ which corresponds to equation (3.4.12). Then, the input impedance, with the effect of bushing taken into consideration, can be derived:

$$H(s) = \frac{U_{in}(s,0)}{I_{in}(s,0)} = \frac{1}{\frac{1}{X+Z_b} + Y_c} + Z_b, \tag{3.4.14}$$

where $Z_b = sL_b + R_b$, and $Y_c = sC_b$.

Since Z_b is much smaller than X, Z_b can be neglected for simplification. Therefore, the equivalent circuit can be treated as a parallel connection between X and Z_b. Then the input impedance becomes:

$$\begin{aligned} H(s) &= \frac{U_{in}(s,0)}{I_{in}(s,0)} = \frac{1}{\frac{1}{X} + Y_c} \\ &= \frac{\Omega_{(1,1)}\Omega_{(n+1,n+1)} - \Omega_{(1,n+1)}\Omega_{(n+1,1)}}{\Omega_{(n+1,n+1)} + Y_c(\Omega_{(1,1)}\Omega_{(n+1,n+1)} - \Omega_{(1,n+1)}\Omega_{(n+1,1)})}. \end{aligned} \tag{3.4.15}$$

Formula of different transfer functions with respect to different measurement connection ways can be derived based on the hybrid winding models. As a consequence simulation studies of FRA interpretations can be investigated as long as accuracy parameters of winding models are provided.

3.5 Analytical Calculation of Electrical Parameters of Winding Models

Suitable calculations of model parameters determine the accuracy of the detailed physical models. Analytical calculations of elementary parameters have been applied widely for decades in physical transformer models. The accuracy of these analytical approaches is limited by geometrical details of real transformers, but they can basically satisfy the models for homogenous transformer geometries.

In the previous research [4, 75], conventional analytical methods are used to calculate parameters in the hybrid winding model. Analytical calculations of capacitive parameters in winding models are introduced in this subsection. Moreover, the approaches for calculating inductive parameter of the model which are derived by Wilcox [80,81] are employed in the previous research, and their detailed formulas can be found in [80–82]. Alternatively, finite element methods (FEM) are applicable for calculating model parameters, especially for cases with deformed windings or complex geometries. A proposal of computational FEM models for undeformed and deformed transformers is presented in Chapter 4.

3.5.1 Insulation Permittivity

In practice, a transformer insulation layer is made of dielectric materials with frequency dependent properties. This property can be revealed in the form of a complex electrical permittivity: $\hat{\varepsilon} = \hat{\varepsilon}_\mathrm{r}\varepsilon_0$. In this expression, ε_0 is the permittivity of free space, and $\hat{\varepsilon}_\mathrm{r}$ denotes complex effective relative permittivity of insulation. It is defined as follows [4, 7]:

$$\hat{\varepsilon}_\mathrm{r} = \varepsilon'(\omega) - j\varepsilon''(\omega) = \varepsilon'(\omega)(1 - j\tan\delta), \tag{3.5.1}$$

where ω is the angular frequency. $\tan\delta$ is the dissipation factor, defined as the ratio between the imaginary and the real parts of the relative permittivity as

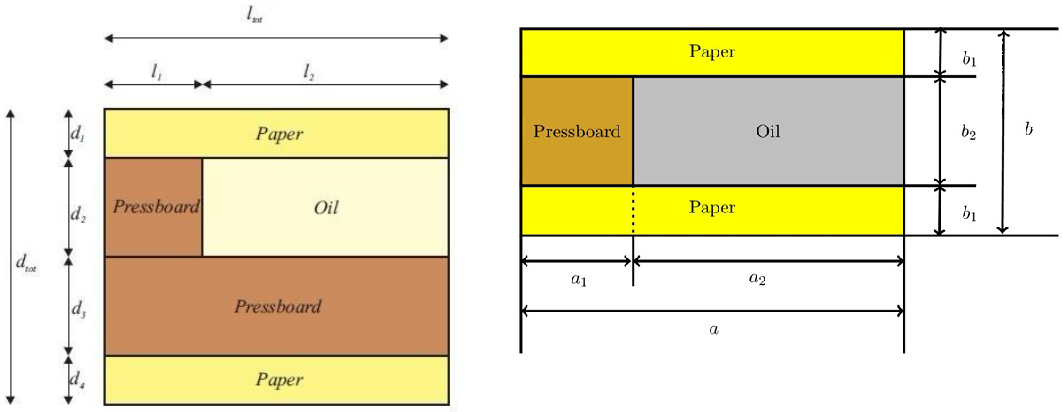

(a) (b)

Figure 3.5: Dielectric structure of (a) insulation between windings [6] and (b) insulation between disks.

below:

$$\tan\delta = \frac{\varepsilon''(\omega)}{\varepsilon'(\omega)}. \tag{3.5.2}$$

The relation between overall conductance G and corresponding capacitance is defined as below [83]:

$$G = C\,\omega\tan\delta. \tag{3.5.3}$$

Typical transformer insulation mainly consists of oil and pressboard, and the permittivity can be calculated by using X-Y model [4, 6]. Considering the paper as well, the dielectric structure of insulation between windings is illustrated in Fig. 3.5(a). In this figure, l_{tot} is length of the total axial spacer, l_1 and l_2 are the width of the axial pressboard spacer and oil duct between the spacers respectively. d_{tot} represents the distance between the windings, d_1 and d_4 is the paper thickness of both sides, and d_2 is the depth of the oil duct, and d_3 is the thickness of the pressboard cylinders between the windings [6]. The complex effective relative permittivity then can be expressed as follows [4, 6]:

$$\frac{1}{\hat{\varepsilon}_{\mathrm{eff}}} = \frac{1}{\hat{\varepsilon}_{\mathrm{paper}}}\cdot\frac{(d_1+d_4)}{d_{\mathrm{tot}}} + \frac{1}{\hat{\varepsilon}_{\mathrm{pb}}\dfrac{l_1}{l_{\mathrm{tot}}} + \hat{\varepsilon}_{\mathrm{oil}}\dfrac{l_2}{l_{\mathrm{tot}}}}\cdot\frac{d_2}{d_{\mathrm{tot}}} + \frac{1}{\hat{\varepsilon}_{\mathrm{pb}}}\cdot\frac{d_3}{d_{\mathrm{tot}}}, \tag{3.5.4}$$

where $\hat{\varepsilon}_{\mathrm{paper}}$, $\hat{\varepsilon}_{\mathrm{pb}}$ and $\hat{\varepsilon}_{\mathrm{oil}}$ are the complex relative permittivities of insulation paper, pressboard material and insulating oil respectively.

Similarly, the insulation between two disks is typically structured as shown in Fig. (3.5(b)), and the expression of the relative permittivity is:

$$\frac{1}{\hat{\varepsilon}_{\mathrm{eff,d}}} = \frac{1}{\hat{\varepsilon}_{\mathrm{paper}}} \cdot \frac{2b_1}{b} + \frac{1}{\hat{\varepsilon}_{\mathrm{pb}}\frac{a_1}{a} + \hat{\varepsilon}_{\mathrm{oil}}\frac{a_2}{a}} \cdot \frac{b_2}{b}, \tag{3.5.5}$$

3.5.2 Calculation of Winding Capacitive Parameters

Series Capacitance

For a continuous disc type winding, in order to calculate series capacitance between discs and between the turns, it is assumed that equipotential surfaces exist in the middle space between adjacent discs and that the potential difference of each disc is equal [4, 6, 7]. A cross-sectional structure of a continuous disc winding with rectangular conductors is illustrated in Fig. 3.6.

The inter-disc capacitance, denoted as C_d, can be calculated by treating the adjacent discs as parallel plates [4, 6, 7]:

$$C_{\mathrm{d,tot}} = \pi\varepsilon_{\mathrm{eff,d}}\varepsilon_0\frac{(R^2_{\mathrm{out,h}} - R^2_{\mathrm{in,h}})}{\tau_{\mathrm{d}} + \tau_{\mathrm{t}}}, \tag{3.5.6}$$

where τ_{t} is the insulation thickness between two turns, τ_{d} is the distance between discs, $R_{\mathrm{out,h}}$ and $R_{\mathrm{in,h}}$ are the outer and inner radii of a disc winding as shown in Fig. 3.6. $\varepsilon_{\mathrm{eff,d}}$ is the relative permittivity between discs and can be derived using equation (3.5.5).

The inter-turn capacitance of rectangular conductors, denoted as C_t, can be calculated as follows:

$$C_{\mathrm{t}} = 2\pi\hat{\varepsilon}_{\mathrm{paper}}\varepsilon_0 R_{\mathrm{i}}\frac{h + 2\tau_{\mathrm{t}}}{\tau_{\mathrm{t}}}, \tag{3.5.7}$$

where h is the height of the disc and R_{i} is the radius of the i_{th} turn. In this equation, $2\tau_{\mathrm{t}}$ is added to take the fringing effect into account [4].

For the reason that parameters per unit length are required in the hybrid winding model as shown in Fig. 3.3, calculations of the inter-disk and inter-turn capacitances per unit length are necessary.

The conductor length of a disk l can obtained by:

$$l = \frac{Area_{disc}}{b} = \frac{\pi(R^2_{\mathrm{out,h}} - R^2_{\mathrm{in,h}})}{b}, \tag{3.5.8}$$

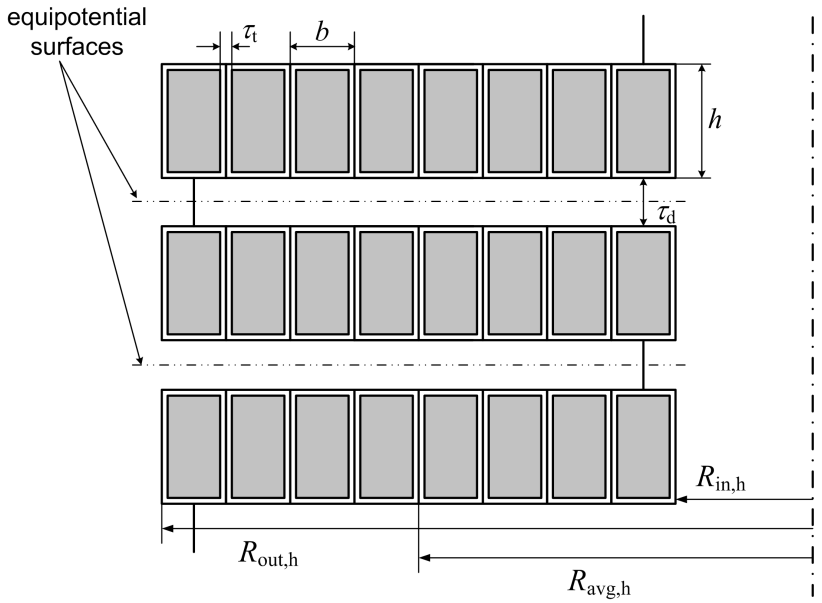

Figure 3.6: Cross-section of a continuous disc winding with 8 turns per disc [4]

where b is the width of a turn of a conductor as shown in Fig. 3.6. Hence, the inter-disc capacitance per unit length can be derived as follows:

$$C_{\mathrm{d}} = \varepsilon_{\mathrm{eff,d}}\varepsilon_0 \frac{b}{\tau_{\mathrm{d}} + \tau_{\mathrm{t}}}, \tag{3.5.9}$$

The length of a turn of conductor is $a_i = 2\pi R_i$, so the inter-turn capacitance per unit length can by obtained by the following equation:

$$K = \hat{\varepsilon}_{\mathrm{paper}}\varepsilon_0 \frac{h + 2\tau_{\mathrm{t}}}{\tau_{\mathrm{t}}}, \tag{3.5.10}$$

The corresponding conductances, G_d and g, can then be calculated using equation (3.5.3). The further simulation studies in the following chapter are specific to continuous disc windings. For other types of winding (eg. helical winding, interleaved disc winding, etc.), calculations of capacitance can be found in [6, 7].

Shunt Capacitance

Shunt capacitances (or ground capacitances) are capacitances either between windings or between a winding and grounded parts (a tank or a core) of

a transformer. The capacitance between HV and LV winding with respect to each disc can be obtained by treating windings as coaxial cylindrical surfaces, which is expressed as follows [6]:

$$C_{\mathrm{HVLV}} = \frac{2\pi\varepsilon_0\varepsilon_{\mathrm{eff}}(h+\tau_{\mathrm{d}})}{\ln\left(\dfrac{R_{\mathrm{in,HV}}}{R_{\mathrm{out,LV}}}\right)}, \tag{3.5.11}$$

where $\varepsilon_{\mathrm{eff}}$ is the effective permittivity between the HV and the LV windings, $R_{\mathrm{in,HV}}$ is the inner radius of the HV winding, and $R_{\mathrm{out,LV}}$ is the outer radius of the LV winding.

The average capacitance per unit length regarding the hybrid winding model as shown in Fig. 3.3 can be derived from equation (3.5.12):

$$K_{\mathrm{HVLV}} = \frac{\varepsilon_0\varepsilon_{\mathrm{eff}}(h+\tau_{\mathrm{d}})}{\ln\left(\dfrac{R_{\mathrm{in,HV}}}{R_{\mathrm{out,LV}}}\right)R_{\mathrm{in,HV}}}, \tag{3.5.12}$$

The shunt capacitance C_{LV} usually indicates the capacitance between a LV winding to an coaxial grounded core. Since the core usually can be regarded as a cylinder approximately, C_{LV} can be considered as a coaxial cylindrical capacitance which is similar to C_{HVLV}. Therefore, its corresponding expressions are similar with equation (3.5.11) and (3.5.12).

On the other hand, due to outermost positions of HV windings, the shunt capacitance C_{HV} between the HV winding and a tank and the shunt capacitance C_{HVHV} between the HV windings in adjacent limbs of a three-phase transformer should be considered as well.

C_{HV} depends on the geometrical shape of the tank. For single-phase transformers, the tank is usually a cylinder. In this case, C_{HV} can be considered as a coaxial cylindrical capacitance which is the same way as C_{HVLV} or C_{LV}. For three-phase transformers, the tank is usually a rectangle with semicylindrical sides, as shown in Fig. 3.7. In this case, C_{HV} of the central phase HV winding can be calculated by equation (3.5.13) [6, 7].

$$C_{\mathrm{HV,geo}} = \frac{1}{4}\cdot\frac{\pi\varepsilon_0(h+\tau_{\mathrm{d}})}{\ln\left(\dfrac{R_{\mathrm{t}}}{R_{\mathrm{out,h}}}+\sqrt{\left(\dfrac{R_{\mathrm{t}}}{R_{\mathrm{out,h}}}\right)^2-1}\right)} \tag{3.5.13}$$

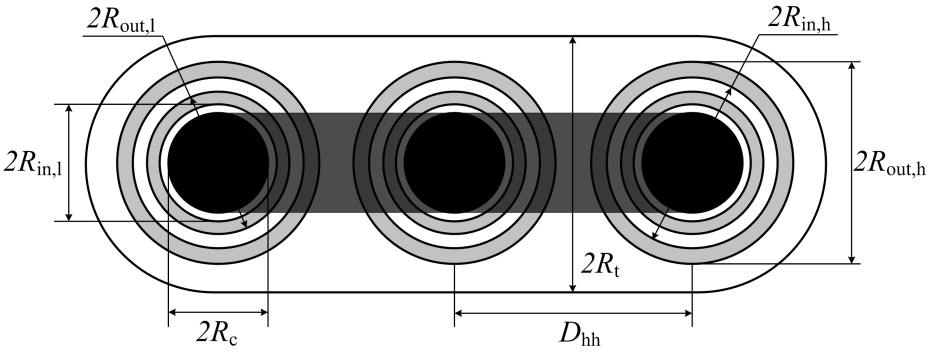

Figure 3.7: Dimensions of a transformer windings, a core and a tank [4]

$R_{\mathrm{t}}, D_{\mathrm{hh}}, R_{\mathrm{t}}$ and $R_{\mathrm{out,h}}$ are illustrated in Fig. 3.7. C_{HV} of the outer phase HV winding can be calculated by equation (3.5.14) [6, 7].

$$C_{\mathrm{HV,geo}} = \frac{3}{4} \cdot \frac{2\pi\varepsilon_0(h+\tau_{\mathrm{d}})}{\ln\left(\dfrac{R_{\mathrm{t}}}{R_{\mathrm{out,h}}}\right)}. \tag{3.5.14}$$

C_{HVHV} can be considered as the capacitance between two parallel cylinders as follows [6]:

$$C_{\mathrm{HVHV,geo}} = \frac{\pi\varepsilon_0(h+\tau_{\mathrm{d}})}{\ln\left(\dfrac{D_{\mathrm{hh}}}{2R_{\mathrm{out,h}}} + \sqrt{\left(\dfrac{D_{\mathrm{hh}}}{2R_{\mathrm{out,h}}}\right)^2 - 1}\right)}, \tag{3.5.15}$$

where D_{hh} is the distance between the axes of two HV windings.

3.6 Summary

A review of widely used transformer modeling methods is presented in this chapter, so that the advantages and drawbacks of existing modeling methods are introduced. Detailed physical modeling is considered to be the appropriate method for high frequency modeling of power transformers. After analyzing and comparing two typical detailed physical models, a simplified distributed parameter model (hybrid winding model) is decided to be employed for high frequency FRA interpretation due to comprehensive properties of less computation complexity and high accuracy of simulation results in high frequency

range. For the purpose of numerical simulations of frequency responses of a transformer presented in the next chapter, this hybrid winding model of power transformers is discussed in detail, and the expressions of transfer functions for FRA is presented as well. Analytical calculations of the model parameters are presented to support the complete construction of the mathematical winding model.

Chapter 4

Finite Element Modeling of Power Transformers for Analysis of Incipient Winding Faults

4.1 Introduction

In terms of the accuracy of transformer modeling, on the one hand, it depends on the types of models (eg. lumped parameter model, multi-transmission line (MTL) model, etc. as introduced in Section 3.2). On the other hand, it also heavily depends on the accuracy of model parameters (eg. inductance, series capacitance, shunt capacitance, etc.).

It was stated in Section 3.5.2 that analytical calculation of elementary parameters is suitable for homogenous transformer geometries. Nevertheless, for transformers with complex geometries or deformed windings, conventional analytical approaches can on longer ensure the accuracy of the parameters, and the resulting mathematical models contain nonlinear partial differential equations (PDEs). Finite element method (FEM) is an alternative tool to solve the mathematical models with certain incipient winding faults, to which analytical approaches are no longer applicable. FEM is a powerful numerical technique to find the approximate solutions of PDEs and integral equations. The basic idea

of FEM is that it divides the whole space into non-overlapping elements with simpler geometry, called finite elements or a mesh, and variational methods from the calculus of variations are used to solve the problem by minimizing an associated error function. Commercial software packages are developed to implement the FEM for physics-based modeling and simulation, such as COMSOL multiphyics and ANSYS. They offer advantageous options of meshing and PDE's solvers. COMSOL [84] is used as a solution tool throughout this work. The description of the meshing methods and variational methods for solving the PDE's can be found in the support document of this software.

In most FRA research such as in [33, 35, 71, 75], parameters for an equivalent winding model are calculated using analytical expressions, where the skin effect and diamagnetic properties in windings are neglected [72,85]. To develop a winding model with adequate high frequency performance, accurate calculation of frequency-dependent parameters such as inductances is required, which can be obtained using FEM. In [69, 85, 86], the frequency-dependent behaviors of winding parameters (permeability, conductor resistance and inductance) were investigated by constructing 3-D computational models. However, models concerning transformer winding deformations were not considered, and such parameters obtained from the FEM models were not directly applied into FRA.

The experimental results in [87] illustrate that small changes of parameters, especially capacitance, affect features of the frequency responses. Winding deformation leads to changes in electrical parameters, especially the capacitance and inductance with respect to different severity of faults. However, by using analytical expressions alone, the electrical parameters for certain types of winding deformation are very difficult to calculate in an accurate manner. As a result, in most previous research such as [34, 35, 88], specific changed values of each parameter in correspondence with changes of transformer structures were not available, and only percentage values of parameters were suggested to roughly represent a deformed winding. An effective way to calculate these changed parameters is to construct an FEM model for a deformed transformer winding, and then distributions of electromagnetic fields in this model can be

calculated, thereby enabling accurate derivation of relative parameters of this deformed winding.

In this chapter, computational models with regard to an undeformed case and certain cases of different winding deformations are constructed to implement the FEM, for the purpose of calculation of accurate parameters including the effect of diamagnetic properties of the transformer materials. Effective permeability tensor of winding conductors is firstly calculated by constructing corresponding 2-D models. In this manner, certain frequency-dependent effects of the transformer materials can be included in further modeling for calculation of inductance. Secondly, 3-D models for different cases of winding conditions are constructed to calculate corresponding frequency-dependent inductances. 2-D models are next constructed to calculate shunt capacitances especially regarding cases of radial winding deformation.

The results of theses FEM models are then applied in the hybrid winding model introduced in last chapter for simulation studies of an undeformed case and cases of incipient winding faults at both low and high frequency ranges. The frequency response in the undeformed case is compared with experimental results to verify the accuracy of the frequency-dependent parameters and mathematical winding models. Four cases of radial winding deformation and three scenarios of minor axial winding movement are analyzed in detail.

4.2 FEM Modeling of Winding Parameters

4.2.1 Effective Permeability Tensor of a Winding Conductor

Permeability Tensors

Before constructing 3-D models of power transformers, 2-D models of winding conductors are built firstly to calculate the effective permeability of windings. When the frequency rises to a certain range, the effects, such as the skin effect, proximity and geometrical effects, cannot be ignored for accurate

determination of eddy-current losses in windings. A winding can be treated as a homogeneous aggregate of unit cells of winding conductors. Therefore, in order to determine the effective permeability of windings, a single unit of conductor is considered first.

When a solid conductor is placed in an magnetic field, eddy current is induced inside the conductor, and thereby producing corresponding magnetic field which interacts with the external magnetic field. The conductor then shows anisotropic diamagnetic property. Due to this property, the diamagnetic permeability of a winding conductor is expressed by a 3 by 3 matrix, which is written as [85]:

$$\overleftrightarrow{\hat{\boldsymbol{\mu}}}_{\mathrm{eff}} = \begin{bmatrix} \hat{\mu}_{\mathrm{x}}^{\mathrm{eff}} & 0 & 0 \\ 0 & \hat{\mu}_{\mathrm{y}}^{\mathrm{eff}} & 0 \\ 0 & 0 & \hat{\mu}_{\mathrm{z}}^{\mathrm{eff}} \end{bmatrix}. \tag{4.2.1}$$

$\hat{\mu}_{\mathrm{x}}^{\mathrm{eff}}$, $\hat{\mu}_{\mathrm{y}}^{\mathrm{eff}}$, and $\hat{\mu}_{\mathrm{z}}^{\mathrm{eff}}$ are the complex effective permeabilites in the x, y and z directions respectively concerned with the local Cartesian coordinate of the cross-section of winding conductors (see Fig. 4.1). The symbol $\hat{}$ is used to represent complex quantities, and bold letters stand for vectors.

In order to simulate the magnetic field of winding conductors in 2-D plane for simplicity, the system of conductors is assumed to be extended infinitely along the direction which is tangential of the coils (y axis in the local Cartesian coordinate). With the aim of simulating the magnetic field of a single unit conductor, it is assumed that each conductor subjects to the average transverse magnetic field, collectively produced by all conductors of the winding.

Permeability tensor in each direction in local coordinate

When an external alternating current flows along the winding conductor, the magnetic flux density $\hat{\mathbf{B}}$ induced by this current can be expressed by the curl of vector potential $\hat{\mathbf{A}}$:

$$\hat{\mathbf{B}} = \nabla \times \hat{\mathbf{A}}. \tag{4.2.2}$$

The direction of magnetic vector potential $\hat{\mathbf{A}}$ is consistent with the current.

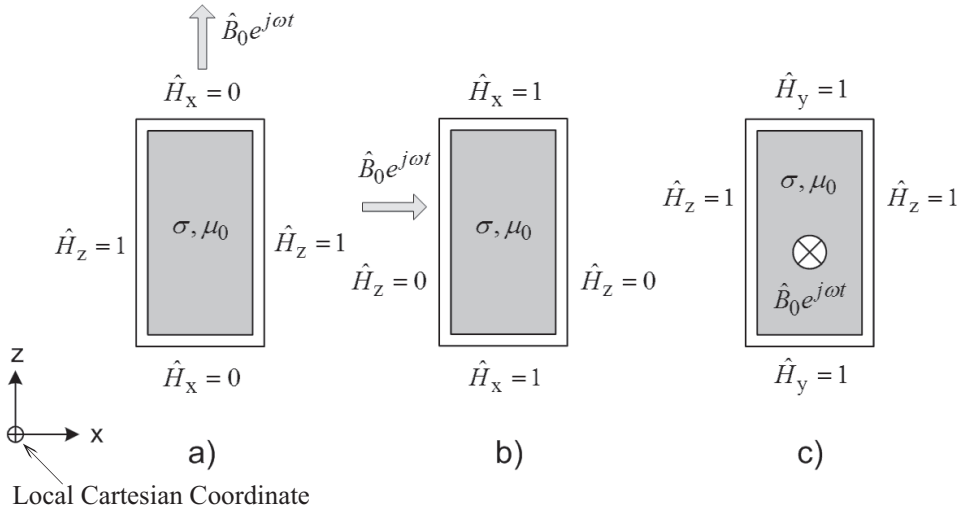

Figure 4.1: Computational regions (unit cells) and boundary conditions for rectangular winding conductors.

According to Stoke's theorem, the $Maxwell - Ampére$ circuital law can be written in a differential form:

$$\nabla \times \hat{\mathbf{H}} = \hat{\mathbf{J}}, \tag{4.2.3}$$

where $\hat{\mathbf{H}}$ is the magnetic filed intensity and $\hat{\mathbf{J}}$ is the current density.

The constitutive relations between the magnetic flux density $\hat{\mathbf{B}}$ and magnetic field intensity $\hat{\mathbf{H}}$ can be expressed as follows:

$$\hat{\mathbf{B}} = \mu_0 \mu_r \hat{\mathbf{H}}, \tag{4.2.4}$$

where μ_0 is the free space permeability, and μ_r denotes the local magnetic permeability. From equations (4.2.2), (4.2.3) and (4.2.4), the current density $\hat{\mathbf{J}}$ can be represented by $\hat{\mathbf{A}}$ as follows:

$$\nabla \times ({\mu_0}^{-1} \mu_r^{-1} \nabla \times \hat{\mathbf{A}}) = \hat{\mathbf{J}}. \tag{4.2.5}$$

Considering the effects of time-harmonic eddy currents, the diffusion equation is expressed as [89]:

$$\nabla \times ({\mu_0}^{-1} \mu_r^{-1} \nabla \times \hat{\mathbf{A}}) + j\omega\sigma \hat{\mathbf{A}} = \hat{\mathbf{J}}, \tag{4.2.6}$$

where σ is the conductivity of winding conductors.

Due to the identical direction of $\hat{\mathbf{J}}$ and $\hat{\mathbf{A}}$ (along axis y), they can be re-written as $\hat{\mathbf{J}} = (0, \hat{J}, 0)$ and $\hat{\mathbf{A}} = (0, \hat{A}_y, 0)$.

The current density $\hat{J}$ in the direction of y can be derived as follows [89]:

$$\hat{J} = \sigma E = \sigma(-\nabla \hat{V}) = \sigma(-d\hat{V}/dy) = \sigma(-\Delta \hat{V}/L) \tag{4.2.7}$$

where E denotes the electric filed intensity, $\hat{V}$ denotes the voltage potential. Electric field intensity E equals the gradient of voltage potential $\hat{V}$, while due to the orientation of conductor, $\nabla \hat{V} = d\hat{V}/dy$. The differential of $\hat{V}$ in y direction can be presented by the voltage drop over length L, $\Delta \hat{V}/L$.

Substituting (4.2.7) into (4.2.6), it can be obtained:

$$\nabla \times ({\mu_0}^{-1}\mu_r^{-1} \nabla \times \hat{\mathbf{A}}) + j\omega\sigma\hat{\mathbf{A}} = \sigma(-\Delta \hat{V}/L)\mathbf{e}_y, \tag{4.2.8}$$

where $\mathbf{e}_y$ stands for the unit matrix of y.

The current flowing through the cross section area of the conductor S can be expressed:

$$I_0 = \int_S -j\omega\sigma\hat{A}_y - \sigma\Delta\hat{V}/L ds. \tag{4.2.9}$$

In order to calculate the effective permeability tensor, the z component of the tensor is calculated first. The unit cell is shown in Fig.4.1a), where the external magnetic flux density is $\hat{\mathbf{B}}_0 = (0, 0, \hat{B}_0)$. The governing equations are derived from equation (4.2.8) and (4.2.9) by setting the total current to zero to preserve the characteristics of induced eddy current. Then the governing equations are:

$$\nabla \times ({\mu_0}^{-1}\mu_r^{-1} \nabla \times \hat{\mathbf{A}}) + j\omega\sigma\hat{\mathbf{A}} = \sigma(-\Delta \hat{V}/L)\mathbf{e}_y \tag{4.2.10}$$

$$\int_S (-j\omega\sigma\hat{A}_y - \sigma\Delta\hat{V}/L) ds = 0. \tag{4.2.11}$$

The boundary conditions have been shown in the Fig.4.1a). With the governing equations and boundary conditions, the field problem can be solved using FEM regarding the software. After the variables $\hat{\mathbf{A}}$ and $\Delta \hat{V}/L$ are obtained, the z component of effective permeability is further determined by:

$$\hat{\mu}_z^{\text{eff}} = \frac{1}{\mu_0 a \hat{H}_z} \int_0^a \hat{B}_{z|z=0} dx, \tag{4.2.12}$$

where a is the dimension of the unit cell in the x direction. From the Fig.4.1a), $\hat{H}_z = 1$. Based on (4.2.2), $\hat{B}_z$ can be obtained by:

$$\hat{B}_z = \frac{\partial \hat{A}_y}{\partial x}. \tag{4.2.13}$$

Therefore, the z component of effective permeability tensor can be obtained at different frequency ranges.

Equations similar to (4.2.10)$\sim$(4.2.13) are used to calculate the x component of effective permeability tensor, as shown in (4.2.14). In this case, the external magnetic field is directed in the x direction, so $\hat{\mathbf{B}}_0 = (\hat{\mathrm{B}}_0, 0, 0)$. The boundary conditions are shown in Fig. 4.1b).

$$\begin{aligned} \hat{\mu}_{\mathrm{x}}^{\mathrm{eff}} &= \frac{1}{\mu_0 b \hat{H}_x} \int_0^b \hat{B}_{\mathrm{x|x=0}} dz \\ \hat{B}_{\mathrm{x}} &= \frac{\partial \hat{A}_{\mathrm{y}}}{\partial z} \\ \hat{H}_x &= 1, \end{aligned} \tag{4.2.14}$$

where b is the dimension of the unit cell in the z direction.

When considering the external magnetic flux density in the y direction ($\hat{\mathbf{B}}_0 = (0, \hat{\mathrm{B}}_0, 0,)$), as shown in Fig.4.1c), the governing equations are formulated in terms of the y component of the magnetic field intensity $\hat{H}_{\mathrm{y}}$ as follows [85]:

$$j\omega\mu_0 \hat{H}_{\mathrm{y}} + \nabla \times \left(\sigma^{-1} \nabla \times \hat{H}_{\mathrm{y}}\right) = 0. \tag{4.2.15}$$

The boundary conditions of this case are shown in Figs.4.1 c), the y component of $\overleftrightarrow{\boldsymbol{\mu}}_{\mathrm{eff}}$ is determined by [85]:

$$\begin{aligned} \hat{\mu}_{\mathrm{y}}^{\mathrm{eff}} &= \frac{1}{\mu_0 a b \hat{H}_y} \int_0^a \int_0^b \hat{B}_{\mathrm{y}} dx dz \\ \hat{H}_y &= 1. \end{aligned} \tag{4.2.16}$$

Permeability tensor in global coordinate

By observing the geometric structure of transformer windings, it can be found that the local Cartesian coordinate system of winding conductors is equivalent to the polar coordinate of a 3-D transformer model. Therefore, to convert the permeability tensors of winding conductors obtained from 2-D models into the global Cartesian coordinate system of the 3-D transformer model, $\overset{\leftrightarrow}{\hat{\boldsymbol{\mu}}}_{\text{eff}}$ in the Cartesian coordinate system of the 3-D model (Fig. 4.2) is expressed as follows [86], where (x, y, z) are the unit length in each direction of a 3-D transformer model:

$$\overset{\leftrightarrow}{\hat{\boldsymbol{\mu}}}_{\text{eff}} = \begin{bmatrix} \dfrac{x^2\hat{\mu}_{\text{x}}^{\text{eff}} + y^2\hat{\mu}_{\text{y}}^{\text{eff}}}{x^2+y^2} & \dfrac{\left(\hat{\mu}_{\text{x}}^{\text{eff}} - \hat{\mu}_{\text{y}}^{\text{eff}}\right)xy}{x^2+y^2} & 0 \\ \dfrac{\left(\hat{\mu}_{\text{x}}^{\text{eff}} - \hat{\mu}_{\text{y}}^{\text{eff}}\right)xy}{x^2+y^2} & \dfrac{x^2\hat{\mu}_{\text{x}}^{\text{eff}} + y^2\hat{\mu}_{\text{y}}^{\text{eff}}}{x^2+y^2} & 0 \\ 0 & 0 & \hat{\mu}_{\text{z}}^{\text{eff}} \end{bmatrix}. \tag{4.2.17}$$

4.2.2 Inductance

An undeformed and a radial deformed 3-D models of an experimental transformers used in this research are shown in Fig. 4.2. Due to the symmetrical structure of this transformer, only a quarter geometric model is built to reduce computational time. However, to calculate the inductances of an unsymmetrical structure, a full model is required. For instance, for calculating the self and mutual inductances between two discs of the winding on an outer phase limb, a full transformer model requires to be constructed as shown in Fig. 4.3. A full model would take longer in simulations due to the increased meshing elements, or its computation accuracy would decrease due to the decreased meshing density. Actually it is a compromise between computational time and accuracy. Moreover, the computational time also depends on the performance of implementation computers. In this thesis, quarter geometric models of a single phase transformer are implemented for simulation studies. The computational domains for FEM modeling are as shown in Fig. 4.2(a): D_1 is the volume of the air space in the tank, D_2 is the volume of the core, D_3 is the

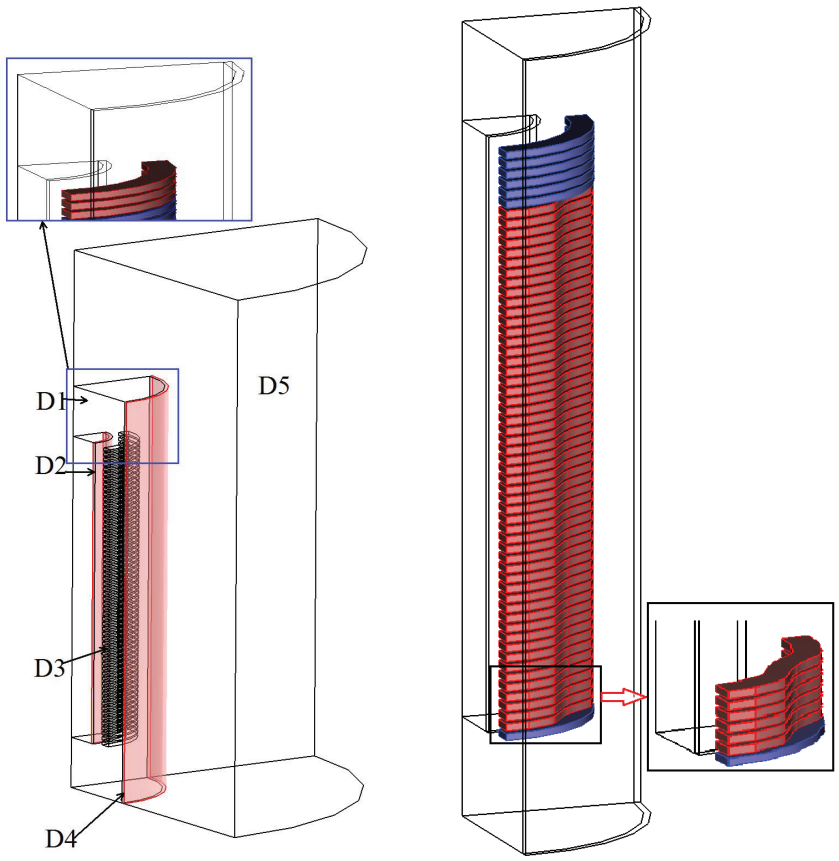

(a) Undeformed model (b) Radial deformed model

Figure 4.2: Computational model of a single-phase transformer. (a) Undeformed model (b) Radial deformed model

volume of the HV windings, D_4 is the volume of the tank, and D_5 is associated with the volume surrounding the transformer.

This model is built in the magnetostatics mode, where the variables are: the vector magnetic potential $\hat{\mathbf{A}}$ and the electric potential $\hat{V}$. Based on the Maxwell's equations the governing formulation in the frequency domain is expressed as below [69]:

$$\nabla \times ((\mu_0 \overleftrightarrow{\hat{\boldsymbol{\mu}}})^{-1} \cdot \nabla \times \hat{\mathbf{A}}) = \begin{cases} 0 & \text{in } D_1, D_2, D_4, D_5 \\ \mathbf{J}^e & \text{in } D_3 \end{cases}, \tag{4.2.18}$$

where μ_0 is the magnetic permeability of free space, $\overleftrightarrow{\hat{\boldsymbol{\mu}}}$ is the complex frequency-

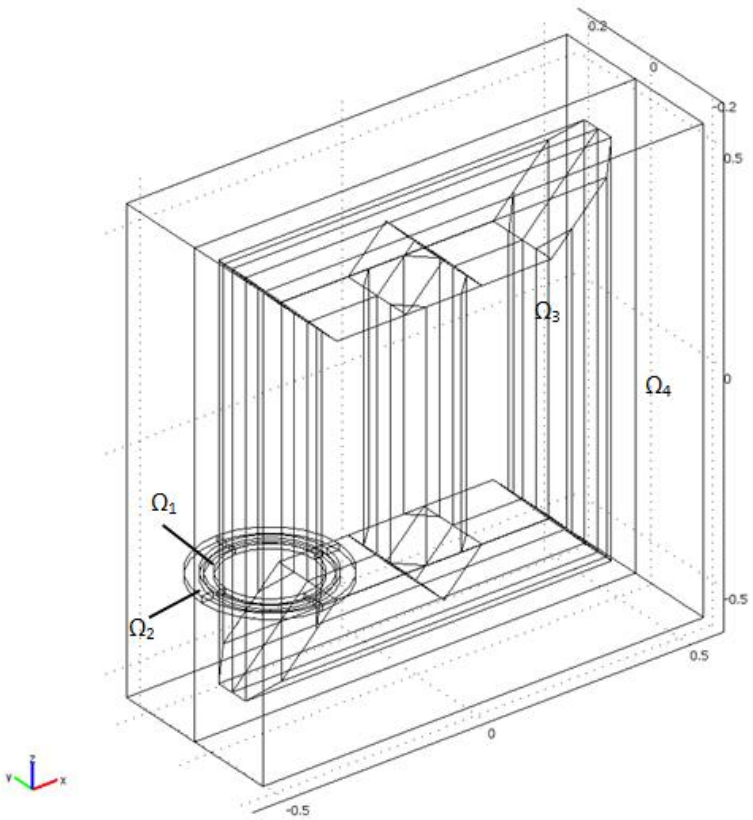

Figure 4.3: Computational model of a three-phase transformer in which two discs of winding are drawn for calculating the self and mutual inductances between these two discs (unit: m)

dependent permeability tensor, $\mathbf{J}^e$ is the external current density along the azimuthal direction. The permeability tensors used in this 3-D model are:

$$\overleftrightarrow{\hat{\boldsymbol{\mu}}} = \begin{cases} \overleftrightarrow{\hat{\boldsymbol{\mu}}}_{\text{tank}} & \text{in } D_4 \\ \overleftrightarrow{\hat{\boldsymbol{\mu}}}_{\text{eff}}^{\text{HV}} & \text{in } D_3 \\ \overleftrightarrow{\hat{\boldsymbol{\mu}}}_{\text{core}} & \text{in } D_2 \\ 1 & \text{in } D_1, D_5 \end{cases} . \tag{4.2.19}$$

In (4.2.19), $\overleftrightarrow{\hat{\boldsymbol{\mu}}}_{\text{eff}}^{\text{HV}}$ can be derived from (4.2.17). For models with consideration of LV winding, the effective permeability of similar to $\overleftrightarrow{\hat{\boldsymbol{\mu}}}_{\text{eff}}^{\text{HV}}$. For a laminated core, the derivation of the effective permeability tensor $\overleftrightarrow{\hat{\boldsymbol{\mu}}}_{\text{core}}$ can be found

in [69]. For a cylindrical core which is used as an equipotential surface, $\overleftrightarrow{\hat{\boldsymbol{\mu}}}_{\text{core}}$ is simply decided by the general property of the core material.

The uniform external current density $\mathbf{J}^e$ can be derived by:

$$\mathbf{J}^e = \mathbf{t}N\hat{I}/S_{\text{c}}, \tag{4.2.20}$$

where N is the number of turns in the winding, $\hat{I}$ is the external current, and S_{c} denotes the total cross-sectional area (including the area of the insulation layer) of the winding section. $\mathbf{t}$ is the unit vector in the azimuthal direction of the winding, which can be expressed as (4.2.21) in the Cartesian coordinate system of the 3-D model. (x_0, y_0, z) represents the central z axis of the winding.

$$\mathbf{t} = \begin{bmatrix} -\dfrac{y-y_0}{m} & 0 & 0 \\ 0 & \dfrac{x-x_0}{m} & 0 \\ 0 & 0 & z \end{bmatrix}, \tag{4.2.21}$$

where $m = \sqrt{(x-x_0)^2 + (y-y_0)^2}$.

For the governing equation (4.2.18), the boundary conditions in domains D_2, D_3 and D_4 are set as continuity, which can be expressed by $\mathbf{n}\times(\mathbf{H}_1 - \mathbf{H}_2) = \mathbf{0}$, where $\mathbf{n}$ denotes the surface normal, and $\mathbf{H}_1$ and $\mathbf{H}_2$ are the magnetic field intensities through the surface. The boundary constraint of the air surrounding (D_1 and D_5) is magnetic insulation, which is expressed by $\mathbf{n} \times \mathbf{A} = \mathbf{0}$. Combining these boundary conditions, the governing formulation can be solved numerically using FEM in the static analysis type.

The effective frequency-dependent inductance and resistance of a transformer winding can be derived by injecting an external alternating current $\hat{I}$ into one disc of the winding and solved at different frequencies. An induced voltage on the k^{th} disc of a winding is given by the Faraday's law of electromagnetic induction:

$$\hat{U}_k = \frac{d\phi}{dt}, \tag{4.2.22}$$

where ϕ is the magnetic flux, which can be calculated from the magnetic vector potential $\hat{\mathbf{A}}$ [90]:

$$\phi = \frac{N_k}{S_{ck}} \int_{D_k} \hat{\mathbf{A}} \cdot \mathbf{t} dD, \tag{4.2.23}$$

where N_k, S_{ck} and D_k are the number of turns in the k^{th} disc of the winding, the total cross-sectional area and the computational domain of the k^{th} winding section respectively. For the case of a quarter model, (4.2.23) needs to be multiplied by 4, because only a quarter of $\hat{\mathbf{A}}$ is accounted in the integral. Combining (4.2.22) and (4.2.23), the induced voltage in the k^{th} disc of the winding is calculated by integrating $\hat{\mathbf{A}}$ in the azimuthal direction of the k^{th} disc, which is defined as [69]:

$$\hat{U}_k = \frac{N_k}{S_{ck}} j\omega \int_{D_k} \hat{\mathbf{A}} \cdot \mathbf{t} dD. \tag{4.2.24}$$

For the case of a quarter model, (4.2.24) needs to be multiplied by 4 correspondingly. When the external current flows through a winding in the k^{th} disc only, the self inductance (L_{kk}) and resistance (R_{kk}) of the k^{th} section of the winding can be found from the relation in $\hat{U} = \hat{I}(j\omega L + R)$:

$$R_{kk} = Re\left(\frac{\hat{U}_k}{\hat{I}}\right), L_{kk} = \frac{1}{\omega} Im\left(\frac{\hat{U}_k}{\hat{I}}\right), \tag{4.2.25}$$

where ω is the angular frequency, $\hat{U}_k$ is the induced voltage in the k^{th} disc. Similarly the mutual inductance M_{km} and the mutual resistance R_{km} between the k^{th} and m^{th} discs can be determined by:

$$R_{km} = Re\left(\frac{\hat{U}_m}{\hat{I}}\right), M_{km} = \frac{1}{\omega} Im\left(\frac{\hat{U}_m}{\hat{I}}\right), \tag{4.2.26}$$

where $\hat{U}_m$ is the induced voltage in the m^{th} disc.

In order to reduce computational time, each of the above parameters can be calculated at several frequency points in the frequency range of interest, and the parameter values for the remaining frequency points can be determined using a linear interpolation method. Therefore, frequency-dependent inductances and resistances are calculated. The same processes can be used to set and solve models with incipient winding faults, such as the radial deformed model shown in Fig. 4.2(b).

4.2.3 Capacitance

In most research, the capacitances of a winding model are calculated using the classic analytical formulae introduced in [6, 75]. Nevertheless, this method is difficult to apply when calculating the capacitance between deformed coils, especially radial deformed coils. For this reason, in this research FEM is only implemented to calculate the ground capacitance (shunt capacitance) aiming at determining capacitances in cases of radial deformation.

The average ground capacitance C_i used in the hybrid model represents the electrical field between the HV winding and the tank or the LV winding per unit length of winding conductor. In the simulation of the undeformed case, C_i is normally treated as a cylindrical capacitance. However, when winding buckling occurs due to radial electromagnetic forces, such as shown by Fig. 4.4(a), the electrical field is inhomogeneous, which means the cylindrical capacitance expression is not applicable anymore. The calculation method illustrated in [33] and [6] requires analytical equations describing the deformed shapes [6], which makes the analytical calculation too complicated. In this study, a 2-D model can be constructed to calculate deformed capacitance C_i by using FEM directly.

In order to calculate the ground capacitance C_i, i.e. C_i between a deformed HV winding and a healthy LV winding, the winding in its 2-D cross-sectional plane can be simplified to a curve as each winding is equipotential. By setting one surface as an input port, maintaining a constant potential at this port, and keeping the other one at the ground potential, a method based on the conservation of energy can be used. Fig. 4.4(b) shows an example of simulation results, which illustrates the distribution of electric potential between the HV winding with 3 buckling and the tank.

In an electrostatic field, the electric potential satisfies the Poisson's equation, which is $-\nabla \cdot (d\varepsilon_0\varepsilon_r \nabla V) = d\rho$, where ε_0 and ε_r are the permittivity of free space and the relative permittivity respectively, d is the thickness of a disc of HV winding, and ρ is the charge density. Because the charge density in dielectric material (sub-domain D) is zero, the electric potential at any position

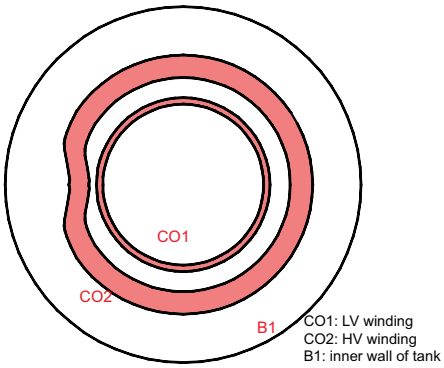

(a)

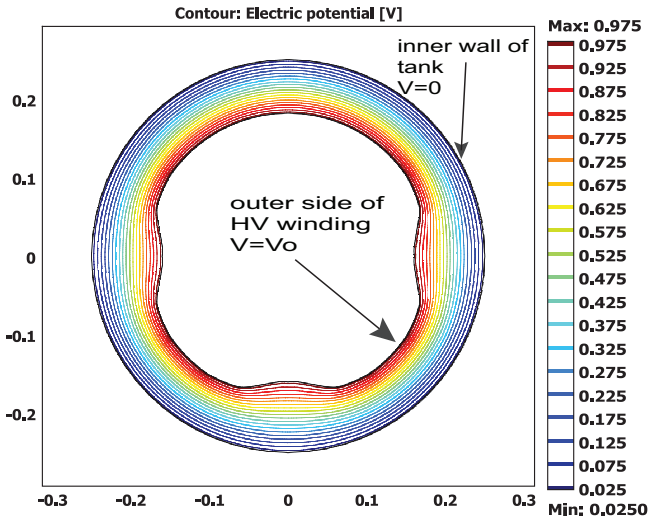

(b)

Figure 4.4: (a) Free mode buckling on HV Winding. (b) Distribution of electrical potential between a deformed HV winding and a healthy LV winding.

of this space can be calculated by FEM, as well as the electric energy density W_e. The differential potential between the two surfaces of windings (V_0) is already set, and as a result the capacitance can be derived by (4.2.27):

$$C_{\mathrm{i}} = \frac{2}{V_0} \int_D W_e dD. \tag{4.2.27}$$

4.3 Specification of Case Studies

4.3.1 Specification of Test Transformer

A single-phase power transformer, transformer-II, is employed as a test object in this study. The HV winding consists of 30 double-discs (11 turns per disc), and the LV winding is a 23-turn (6 conductors in parallel) helical winding. Aluminum has been chosen as the material for simulating the equipotential core surface and tank surface. The geometrical dimension is provided in Fig. 4.5. In the case studies, because the magnetic flux path travels through the core and tank rather than a closed loop of a core, the effects of the cylindrical core and tank is not such sensitive. Therefore to simplify the analysis,

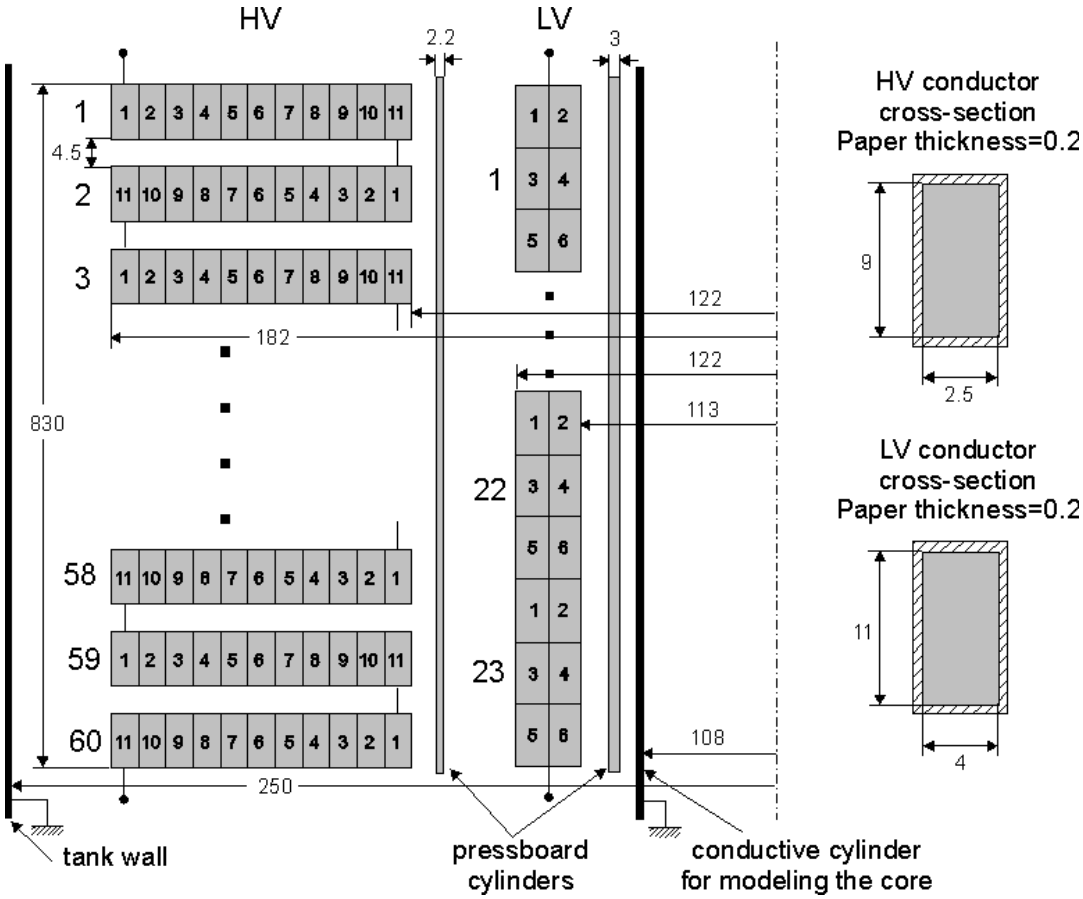

Figure 4.5: Geometrical Dimensions of transformer 2 (unit: mm) [4, 7]

a simple scalar permeability of the core and the tank is specified instead of a complex permeability to simplify the computational model. The simulation frequency range is generally from 10 Hz to 5 MHz (varies according to each case study). The 3-D model of the transformer in the undeformed case is meshed into 169,747 elements as illustrated in Fig. 4.6(a). Taking the case study of minor radial deformation as an example, the general process of FEM modeling using COMSOL Multiphysics and the parameter calculation procedures are illustrated in Fig. 4.7.

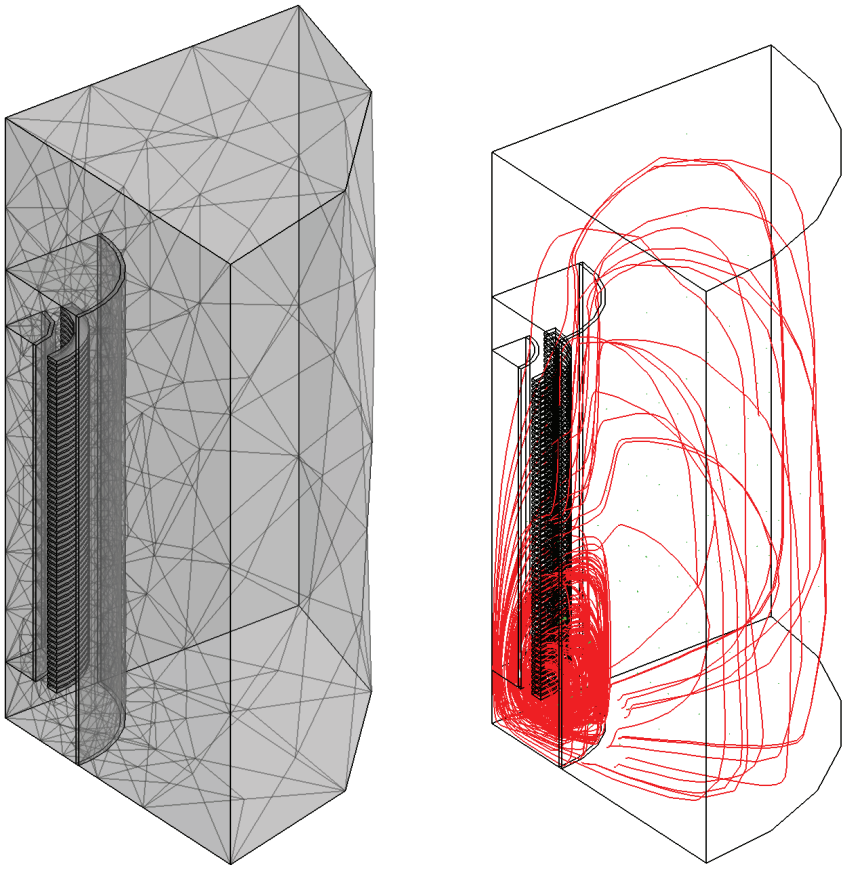

(a) 3-D transformer model of finite-element mesh.

(b) Simulation result at a frequency of 50 Hz.

Figure 4.6: 3-D computational model of the experimental transformer

In practice, a proper device setup is required for precise FRA measurement in the high frequency range. Fortunately, various FRA test instruments are

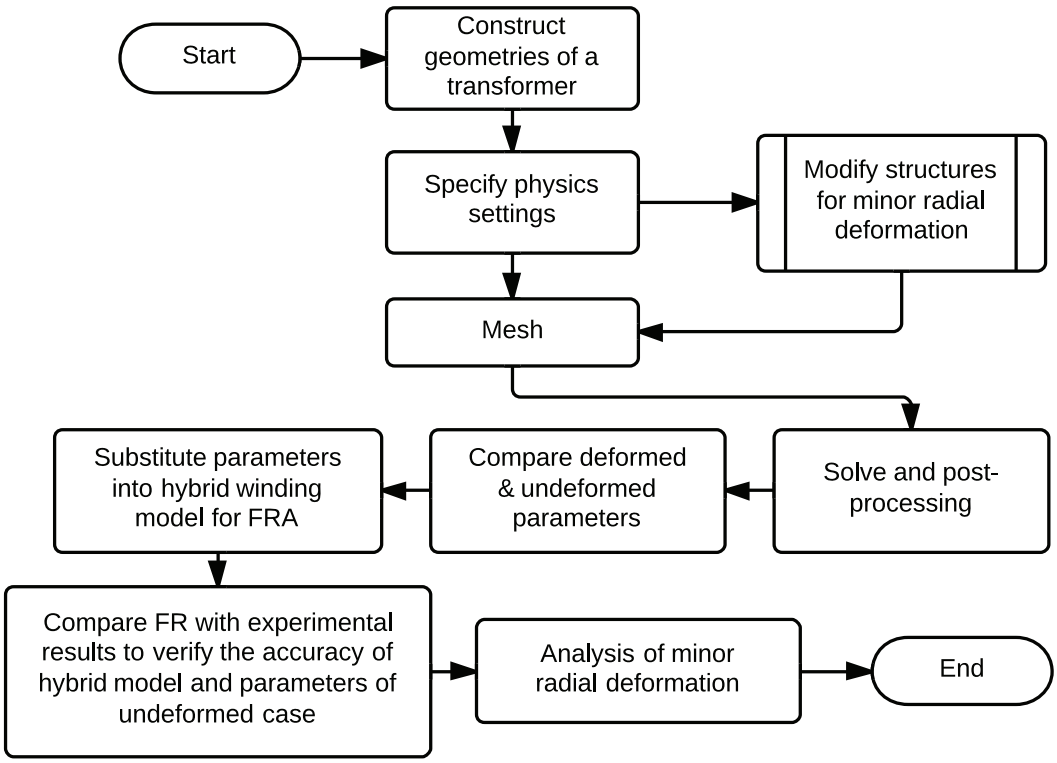

Figure 4.7: The flowchart for calculation of parameters and FRA

developed using innovative connection technique to improve the measurement sensitivity in the high frequency range. For example, as mentioned in Chapter 2, the test frequency range of a FRAnalyzer is from 10 Hz to 20 MHz.

4.3.2 Inductance Variation at Different Frequencies

Figure. 4.6(b) illustrates one of the simulation results of the undeformed model at 50 Hz, in which the stream-line represents magnetic fluxes. The self inductance of the first disc of the winding and the mutual inductances to the next 29 discs at different frequencies are plotted in Fig. 4.8, which shows that the self inductance experiences a significant decrease with the increase of frequency. In comparison, the change of mutual inductances is not drastic. The self inductance has a remarkable influence on the frequency response of the equivalent winding circuit, which means its accuracy determines the accuracy

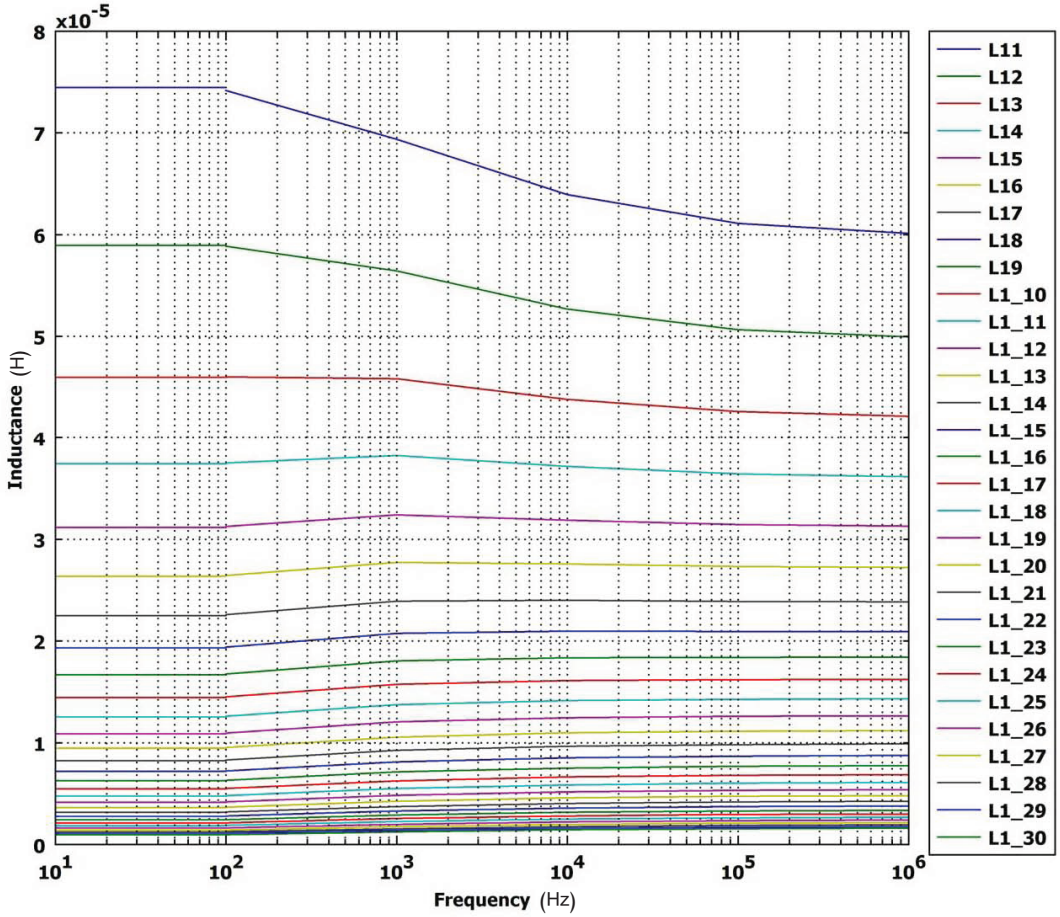

Figure 4.8: Inductances of first 30 discs

of the hybrid winding model. Therefore, functions of the average inductances corresponding to different frequencies are used in the study instead of a constant value across all frequency ranges. In this case, the self inductance is expressed in 5 frequency ranges based on the trend shown in Fig. 4.8 as listed below:

$$L_{11} = \begin{cases} L_{50\text{Hz}} & \text{when } f < 100 \text{ Hz} \\ a_1 * f + b_1 & \text{when } 100 \text{ Hz} \leq f < 1 \text{ kHz} \\ a_2 * f + b_2 & \text{when } 1 \text{ kHz} \leq f < 10 \text{ kHz} \\ a_3 * f + b_3 & \text{when } 10 \text{ kHz} \leq f < 100 \text{ kHz} \\ a_4 * f + b_4 & \text{when } f \geq 100 \text{ kHz} \end{cases}, \tag{4.3.1}$$

where, f represents the frequency, and L_{50Hz} is the average self inductance at 50 Hz. The interpolation coefficients represented by 1×4 matrices $\mathbf{A} = [a_1\ a_2\ a_3\ a_4]$ and $\mathbf{B} = [b_1\ b_2\ b_3\ b_4]$ can be derived from simulation results.

4.3.3 Comparison with Experiment Responses for Undeformed Case

Applying the coefficients obtained in (4.3.1) and the derived capacitances into the transfer function (3.4.15) derived in Chapter 3, the frequency response of input impedance is derived and plotted in Fig. 4.9. In order to compare the result with the measured frequency response clearly, the frequency response results presented in Fig. 4.9 is plotted in the log-log type. It is observed that the simulated and measured responses are close to each other as far as the general shape and resonant frequencies are concerned, this verifies the accuracy of the hybrid winding model using the parameters derived by FEM simulations.

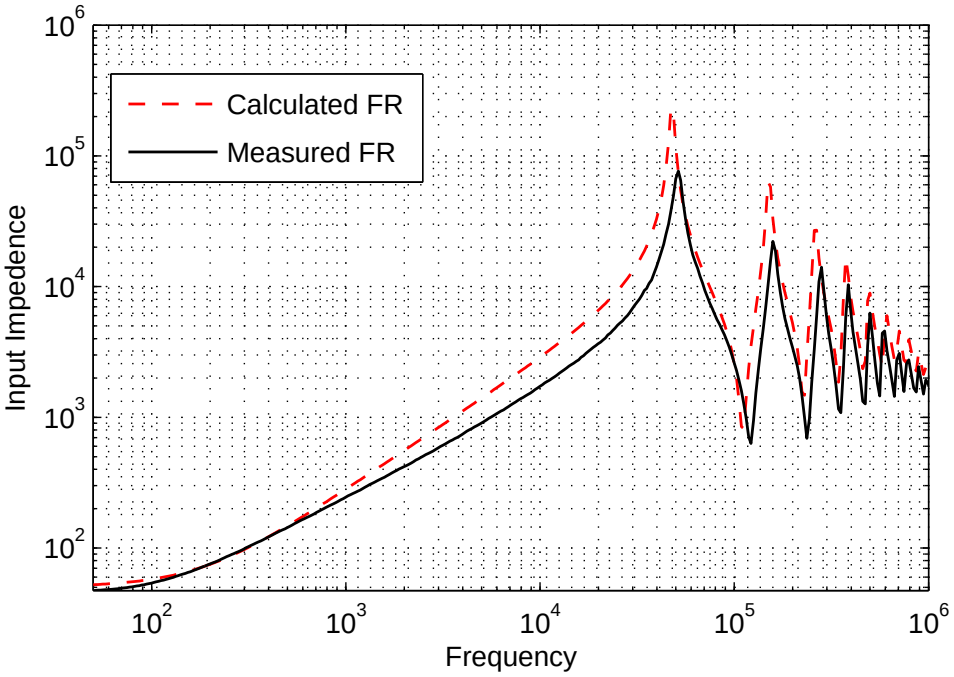

Figure 4.9: Log-log plot of input impedance response

4.4 Case Study of Radial Winding Deformation

4.4.1 Variation of Inductance

This section is focused on radial deformation. Obviously, change of the transformer geometric structure affects the distribution of magnetic flux, which thereby changes inductances. An example of radial deformed model, in which the HV winding suffered 4 buckling from the 2nd to 54th discs as shown in Fig. 4.2(b), has been simulated at 50 Hz to investigate the change of inductance matrix. Table 4.3 shows the relative deviation of self and mutual inductances compared with the results derived from the undeformed case; the comparison yields an approximate 10% reduction of mutual inductances of the 2nd to 54th discs to the first disc.

According to the Telegrapher's equations for lossy transmission lines introduced in Chapter 3, the capacitance (C) as well as the inductance (L) have a significant impact on a FRA test. In most previous research, small changes in capacitance were considered to greatly affect the features of frequency responses especially at the high frequency range, while the changes of inductances were ignored in simulations for detecting of winding movements. In fact, it can be deduced from one of the propagation expression (3.3.24) that frequency responses also have high sensitivity to significant change of inductance at the higher frequency range in certain cases of winding faults [4]. In some cases of winding deformation, such as axial movement, the change of inductance is not as significant as the change of capacitance. However, from Table 4.3, it can be found that there is around 10% reduction of mutual inductances of the 2nd to 54th discs to the first disc. Therefore, the changes of inductances are remarkable due to free buckling on winding coils.

Table 4.1: Relative deviation (%) of elements of inductance matrix with 4 bucklings on 2nd-54th discs of HV Winding (f=50 Hz)

$L_{1,1}$	$L_{1,2}$	$L_{1,3}$	$L_{1,4}$	$L_{1,5}$	$L_{1,6}$
0.4801	-9.9971	-9.7099	-9.4511	-9.2304	-9.1881
$L_{1,7}$	$L_{1,8}$	$L_{1,9}$	$L_{1,10}$	$L_{1,11}$	$L_{1,12}$
-9.3259	-9.3589	-9.4028	-9.3117	-9.4879	-9.5771
$L_{1,13}$	$L_{1,14}$	$L_{1,15}$	$L_{1,16}$	$L_{1,17}$	$L_{1,18}$
-9.5544	-9.5200	-9.4708	-9.6154	-9.5689	-9.5823
$L_{1,19}$	$L_{1,20}$	$L_{1,21}$	$L_{1,22}$	$L_{1,23}$	$L_{1,24}$
-9.6656	-9.5632	-9.5317	-9.7106	-9.7260	-9.6392
$L_{1,25}$	$L_{1,26}$	$L_{1,27}$	$L_{1,28}$	$L_{1,29}$	$L_{1,30}$
-9.4923	-9.6431	-9.6615	-9.5346	-9.6791	-9.7054
$L_{1,31}$	$L_{1,32}$	$L_{1,33}$	$L_{1,34}$	$L_{1,35}$	$L_{1,36}$
-9.7147	-9.7330	-9.8813	-10.0158	-9.6862	-9.9535
$L_{1,37}$	$L_{1,38}$	$L_{1,39}$	$L_{1,40}$	$L_{1,41}$	$L_{1,42}$
-9.8533	-9.9065	-9.9630	-10.0677	-10.0386	-10.0768
$L_{1,43}$	$L_{1,44}$	$L_{1,45}$	$L_{1,46}$	$L_{1,47}$	$L_{1,48}$
-10.0361	-10.2590	-10.0031	-10.2772	-10.1912	-10.3618
$L_{1,49}$	$L_{1,50}$	$L_{1,51}$	$L_{1,52}$	$L_{1,53}$	$L_{1,54}$
-10.1659	-10.2457	-10.5466	-10.3082	-10.5709	-10.4899
$L_{1,55}$	$L_{1,56}$	$L_{1,57}$	$L_{1,58}$	$L_{1,59}$	$L_{1,60}$
-0.0267	-0.0284	-0.0332	0.1033	-0.0490	-0.0598

4.4.2 Variation of Capacitance

For the investigation of radial deformation of HV discs, 4 cases are simulated and compared [33] [4]:

1 Buckling HV coils are radially deformed on one position (Fig. 4.4(a)). The deformed depth is around 2 cm, which is about 10% of the HV winding radius.

2 Buckling HV coils are radially deformed on the opposite positions. The deformed depth is around 2 cm.

3 Buckling HV coils are radially deformed on 3 positions with a difference of 90° with respect to each other. The deformed depth is around 2 cm.

4 Buckling HV coils are radially deformed on 4 positions with 90ifference with respect to each other. The deformed depth is around 2 cm.

More numbers of buckling points of same degree on a winding are equivalent to stronger severity of radial deformation on the same winding. The calculated ground capacitances in both the undeformed and the radial deformed cases are gpresented and compared in Table 4.2. Comparing the results between the analytical calculations and FEM simulations in the underformed case, the relative deviations are close to zero, which means the FEM simulations are reliable. According to the relative capacitance deviations of deformed cases based on the results using FEM, in this type of deformation, the average capacitance between HV and LV windings increases with the growing number of buckling, while the average capacitance between the HV winding and the tank decreases with the growing number of buckling.

4.4.3 Simulation Results for Radial Winding Deformation

In this research, the LV winding is left floated to simplify the calculation, so radial buckling in the 4 cases only affects the HV winding parameters. Since

Table 4.2: Ground Capacitance with bucklings of HV Winding

Cases	Average Capacitance(pF)		Relative Deviation(%)	
	$C_{\texttt{HVLV}}$	$C_{\texttt{HV-Tank}}$	$C_{\texttt{HVLV}}$	$C_{\texttt{HV-Tank}}$
Undeformed Analytical	6.0119	3.1683	-0.0033	0
Undeformed FEM	6.0117	3.1683		
1 Buckling	6.5993	3.0945	9.77	-2.33
2 Buckling	7.2350	3.0210	20.35	-4.65
3 Buckling	7.8708	2.9474	30.92	-6.97
4 Buckling	8.5066	2.8739	41.50	-9.29

the analysis focuses on one winding, the simulation results are also applicable to the same type of deformation on the LV winding. The transfer function of admittance in (3.4.13) is employed in this section.

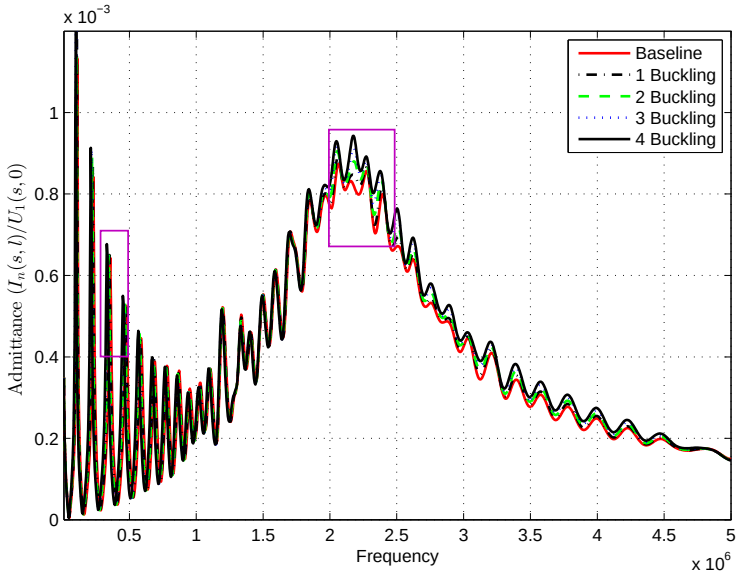

Figure 4.10: Frequency response in 4 cases of radial deformation without changing inductance. Frequency range: 0 Hz - 5 MHz

Without considering the change of inductances, the ground capacitances of the 6th to 54th discs are changed the values as described in Table 4.2 to simulate radial movements for the 4 cases. The corresponding frequency re-

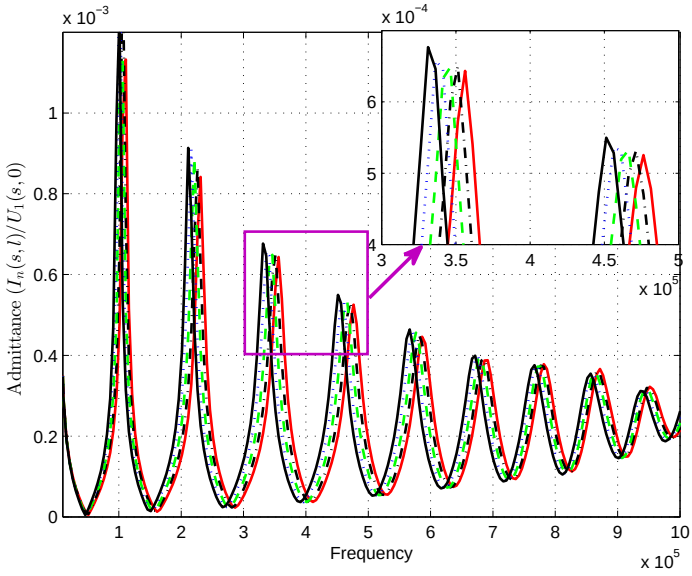

(a) 0 Hz-1 MHz extracted from (a)

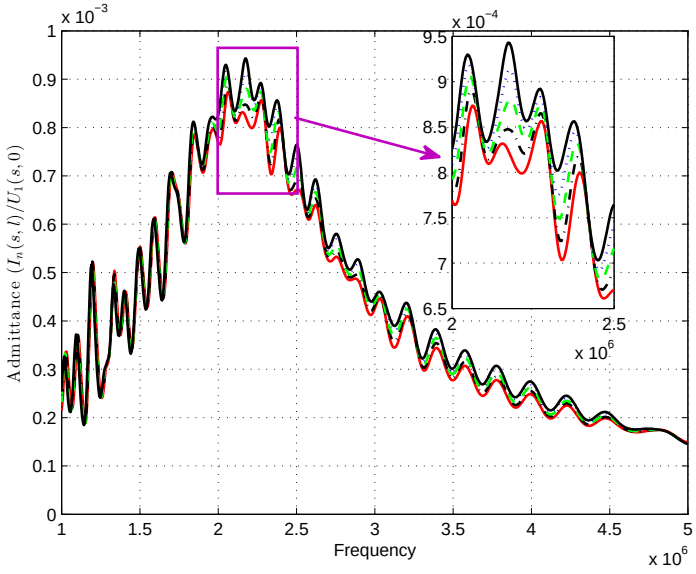

(b) 1 MHz-5 MHz extracted from (a)

Figure 4.11: Frequency response in 4 cases of radial deformation without changing inductance. Frequency range: (a) 0 Hz - 1 MHz (b) 1 MHz - 5 MHz

sponses of admittance are plotted in Fig. 4.10 and partially zoomed in Fig. 4.11. From Fig. 4.11(a) which is the extracted frequency responses up to 1 MHz from the whole frequency range, it can be found that a distinct leftward

shift (up to 4.2% in frequency) occurs at each resonant frequency peak, but the change in amplitude of the admittance at resonant frequencies is not significant. Moreover, more numbers of buckling, which is equivalent to stronger severity of deformation, cause further leftward shifting. The results in the low frequency range meet the experimental results reported in [33] [35]. From Fig. 4.11(b), it shows that when the frequency is higher than 2 MHz, the increase of amplitude of resonant peaks (up to 13% in amplitude) is more recognizable rather than the phase shift. By analyzing the frequency responses over the whole frequency range as shown in Fig. 4.10, it can be summarized that the distortion in amplitude in the frequency range 2 MHz-4.5 MHz is more visible.

To investigate the effect of changing inductances due to the radial deformation on frequency responses, not only the ground capacitances of the 2nd-54th discs have been varied as listed in Table 4.2 in the case of 4 buckling, but also the inductance matrix have been modified as described in Table 4.3. Figure. 4.12(a) shows the corresponding FR in the frequency range 0 Hz - 1 MHz and Fig. 4.12(b) illustrates the FR between 1 MHz - 5 MHz. It is noticed that the reduction of inductances due to radial deformation can shift the resonant frequencies slightly rightwards. While from the observation of Fig. 4.11(a), the resonant frequencies distinctly shift leftwards due to the variations of ground capacitances. Therefore, from Fig. 4.12(a), it shows that the effect of considering the change of L slightly leads to less further leftward shift of resonant peaks when the frequency is lower than 1 MHz. With increasing frequencies, the shift of resonant frequencies is less obvious due to the opposite influences of the reduction of inductances and the variations of ground capacitances. In other words, when considering the effect of changing both inductances and ground capacitances due to radial deformation, the change of frequency response is becoming less obvious, which thereby can be neglected in the low frequency range. Compared with the simulation results in the low frequency range, the results in Fig. 4.12(b) demonstrate that when considering the change of the inductance matrix, the distortion in amplitude in the high frequency range especially between 2 MHz - 3.5 MHz is becoming more remarkable, which matches with the

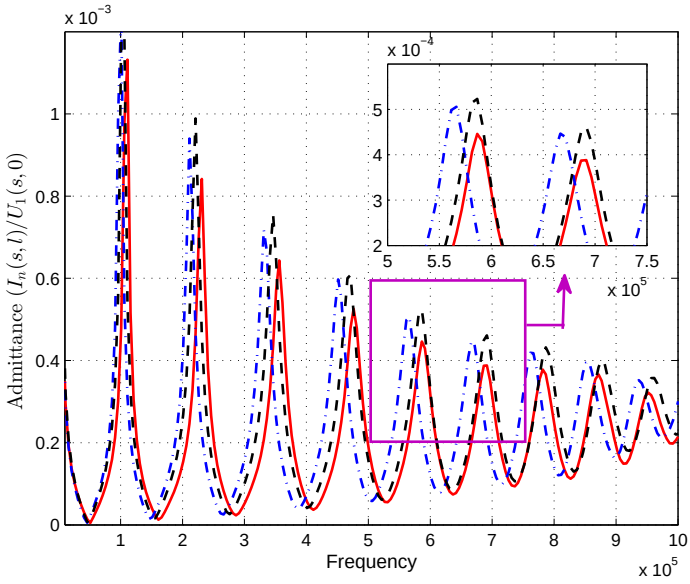

(a) 0 Hz-1 MHz

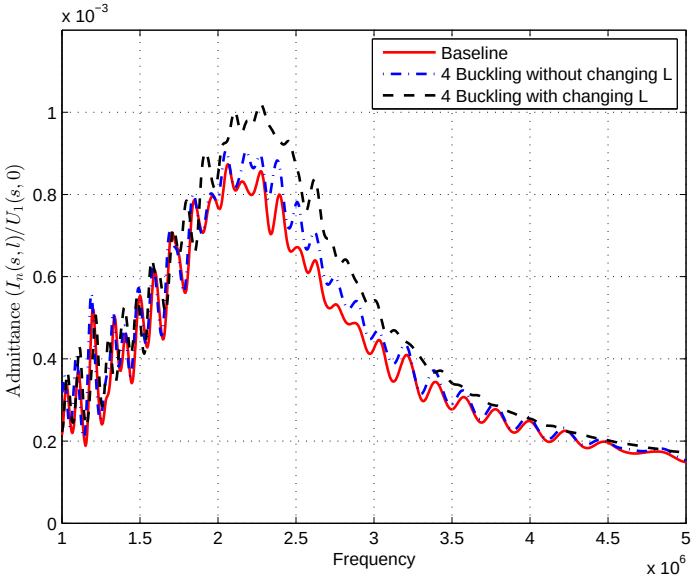

(b) 1 MHz-5 MHz

Figure 4.12: Frequency response for 4 buckling on 2nd to 54th discs. Frequency range: (a) 0 Hz - 1 MHz (b) 1 MHz - 5 MHz

experimental results described in [34]. In summary, by taking the variations of inductances into account, the variations of frequency response in the low frequency range can be neglected in a radial deformation case, but the variations

of frequency response at high frequencies are getting more significant, which means the frequency response in high frequencies possesses more detectable information for minor radial deformation.

4.5 Case Study of Minor Axial Winding Movement

4.5.1 Variation of Inductance

In order to investigate the change of inductances regarding the cases of minor axial winding movement, the simulation results at 50 Hz obtained from a case in which the inter-disc distance from the 11th to 15th discs has a reduction of 20% along the axial direction are compared with the results derived from the undeformed case. Table 4.3 shows the relative deviation of the first 18 groups of inductances. It can be found that the most significant change is the mutual

Table 4.3: Relative deviation (%) of elements of inductance matrix with 20% reduction of inter-disc distance on 11th-15th discs of HV Winding

$L_{1,1}$	$L_{1,2}$	$L_{1,3}$	$L_{1,4}$	$L_{1,5}$	$L_{1,6}$
0.8979	0.6452	-0.1565	0.0059	0.1141	0.1433
$L_{1,7}$	$L_{1,8}$	$L_{1,9}$	$L_{1,10}$	$L_{1,11}$	$L_{1,12}$
0.0190	0.0240	0.0227	0.2973	0.9357	1.8446
$L_{1,13}$	$L_{1,14}$	$L_{1,15}$	$L_{1,16}$	$L_{1,17}$	$L_{1,18}$
2.7514	3.7986	4.7288	0.0217	0.1568	0.1689

inductance of the 15th disc to the 1st disc which is 4.7 %, which means that the inductances of this minor axial movement don't change much. Such slight variations may not be revealed from the frequency responses.

4.5.2 Simulation Results for Minor Axial Winding Movement

Minor axial movement can be simulated by moving part of discs up or down in different degrees. Several scenarios are considered to compare the results:

Scenario I The effect of inductance change is considered.

Scenario II The degree of displacement is changed.

Scenario III The number of deformed discs is changed.

Scenario I

Each disc from the 11th to 15th discs moves left 20% in distance along the axial direction as shown in Fig. 4.13, which means the distance between deformed windings $\tau_{\mathrm{d}}^{'} = 0.8\tau_{\mathrm{d}}$. Hence, a 4.5 mm displacement occurs in this part of 5 discs. The inter-disc capacitance per unit length is expressed in equation (3.5.9) given in Chapter 3. From this equation, the values of inter-disc capacitance C_{d} between deformed discs, $C_{\mathrm{d}(10)(11)}$ to $C_{\mathrm{d}(14)(15)}$, are increased 25%. In both [34] and [35], the simulations of minor axial winding movement were achieved by simply increasing or decreasing part of inter-disc inductances. However, by analyzing the structures of minor displaced windings, the values of these inter-disc capacitance are not simply increased or decreased. For instance, in this case of 11th to 15th discs moving left along the axial direction, the distance between the 15th disc and the 16th disc is increased significantly ($\triangle\tau_{\mathrm{d}} = 5\times0.2\tau_{\mathrm{d}}$ in this case), which means the inter-disc capacitance, $C_{\mathrm{d}(15)(16)}$ are remarkably reduced ($C_{\mathrm{d}(15)(16)} = 0.5C_{\mathrm{d}}$ in this case).

The changes of inter-disc capacitances are much more significant compared with the change of inductances which are shown in Table 4.3. The frequency responses of output-input voltage ratio are shown in Fig. 4.14. From this figure, it can be seen that the resonant peaks shift leftwards significantly from 40 kHz. At the frequency range of 40 kHz to 600 kHz the shift of resonant peaks is most detectable, and at the frequency range of 600 kHz to 2 MHz the magnitude

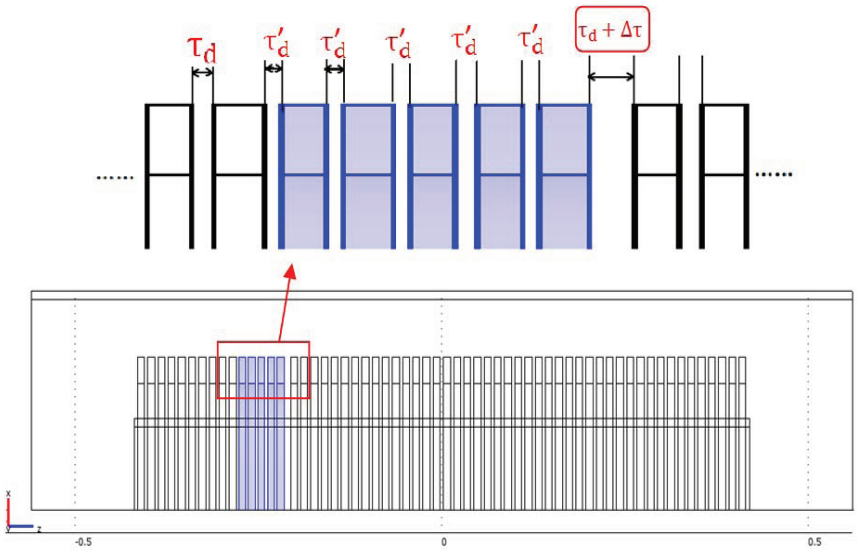

Figure 4.13: Winding structure of axial movement

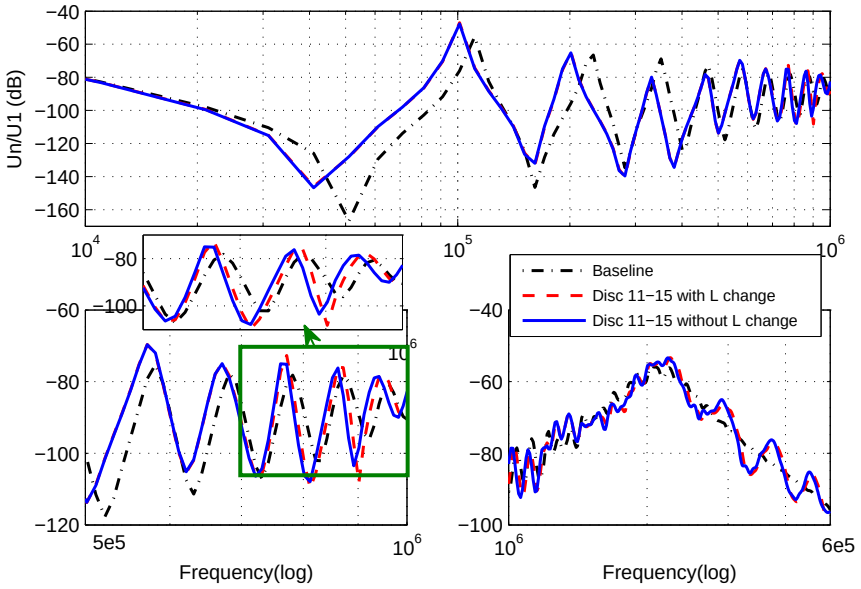

Figure 4.14: Frequency responses in scenario I

of resonant peaks increases slightly. However, in the frequency range above 2 MHz, the distortion is apparent. With consideration of the variations of inductances, the frequency response trace is slightly shifting rightwards when

the frequency is above about 7.5 kHz compared with the trace that only inter-capacitances are changed. However, the impact of changing the inductances is almost imperceptible, due to the slight change of inductance in this case study.

Scenario II

In this scenario, the inter-disc distance along the axial direction of the 31th-35th discs reduces 20% and 50% respectively to represent different severity degrees of winding displacement. The frequency response traces are shown in Fig. 4.15. Comparing the results in Fig. 4.14 with Fig. 4.15, the distortion above 2 MHz is much more significant when the winding displacement occurred near the high voltage lead. From Fig. 4.15, it is obvious that a greater winding displacement leads to further leftward shift of resonant peaks at the frequency range of >40 kHz. Moreover, when the frequency above 800 kHz, the peak-to-peak magnitude is increased with stronger severity degree of the axial winding movement.

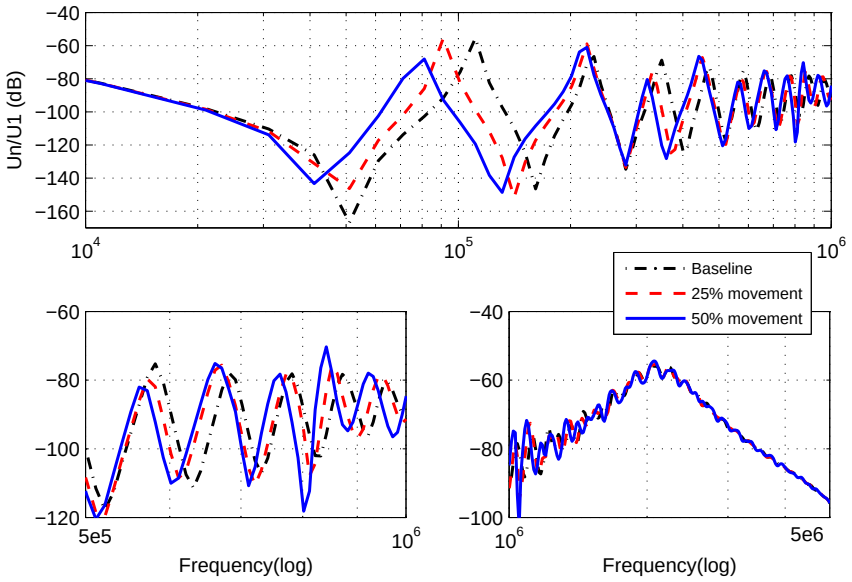

Figure 4.15: Frequency responses in scenario II

Scenario III

To investigate the effect of the number of deformed discs, the location of the most noticeable gap should remain the same. In this case study, 5 discs which is from 31st-35th disc, and 15 discs from the 21st -35th disc are simulated to be moved in the same degree respectively. Figure. 4.16 shows the simulated frequency response results of different numbers of deformed windings. From this figure, it can be observed that the patterns of these three simulations are very similar but slightly further shifting leftwards of resonant peaks from the undeformed baseline with the increasing numbers of deformed discs. In other words, the minor axial winding deformation with more deformed discs is more detectable.

If the location of the most noticeable gap was changed, there will be an obvious difference between patterns. Possibly it could be used to detect deformed locations by recognizing the corresponding FRA results [34].

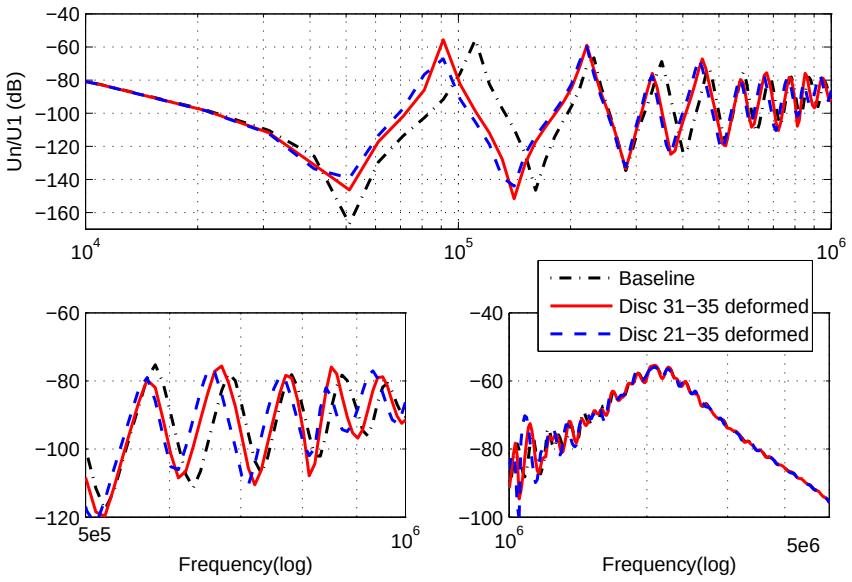

Figure 4.16: Frequency responses in scenario III

4.6 Summary

This chapter has explained how to construct computational FEM models to simulate magnetic and electric fields within a power transformer. By using these FEM models, accurate electrical parameters in equivalent winding circuits are calculated in both cases of undeformed transformer conditions and incipient winding faults. Therefore, due to improved electrical parameters, the hybrid winding model introduced in Chapter 3 performs upgraded accuracy in simulation studies. By using this methodology, fault features of winding deformation can be extracted from FRA data. As a result, a specific fault can be diagnosed by identifying similar fault features from measured frequency response data.

The inductances and capacitances, which are derived using computational FEM models related to a radial deformed transformer, are applied into the hybrid winding model to improve its accuracy, rather than changing relative parameters roughly based on qualitative analysis as in most previous research. Another advantage of using the hybrid model is that an accurate analysis in high frequencies can be achieved. Subsequently, the frequency responses can also be analyzed at the high frequency range, so that more useful information can be extracted in this range. Simulation studies have shown that the radial deformation leads to significant changes in both ground capacitances and inductances. The changes in ground capacitances and inductances all have influence on frequency responses. By considering variations of both ground capacitances and inductances, the variations of frequency responses in the low frequency range are negligible, while frequency responses at high frequencies contains detectable information for minor radial deformation.

Three scenarios have been analyzed in simulation studies of minor axial winding movement. The change of the inductances are subtle. The most noticeable gap between two adjacent discs has major influence on the patterns of frequency response. When the gap gets closer to the high voltage lead, the distortion above 2 MHz becomes much more significant. The differences between the frequency response traces are more detectable with the larger gap

between two adjacent discs especially in the frequency range from 40 kHz to 2 MHz.

Chapter 5

Automatic Transformer Condition Classification Using Binary Erosion and Hybrid Indices

5.1 Introduction

As mentioned in Chapter 1, in practical applications of FRA method, interpretation of frequency responses is usually conducted by experts using graphical analysis based purely on visual comparison. This means that a certain level of expertise is required to assess the condition. In order to make the FRA interpretation methods easy to use, quantitative interpretation methods by using statistical indices (or indicators) have been popular to be applied to assess frequency responses in recent years [91–95]. Among the applied statistical indices, only a few of them provide criteria, and some indices have been applied to commercial FRA instruments by some manufacturers. For example, the Relative Factor (R_{XY}) defined by the Chinese standard in 2004 (DL/T911-2004) and E index established by North China Electric Power Research Institute (NCEPRI) are implemented in an FRA instrument named FRAnalyzer. R_{XY} is calculat-

ed by means of the calculation of variances and covariances, and E index is related to the calculation of the difference indices. In this case, technicians can directly acquire diagnostic results according to R_{XY} or E index, once they measure the frequency responses and import the reference. However, current quantitative interpretation methods only provide information of the severity of deformation, rather than identifying the failure modes [42]. Identification of the type of transformer fault is essential for developing appropriate maintenance plans. Therefore, it is necessary to develop more precise interpretation algorithms for automatic condition assessment.

Although the detailed form of FRA response curves depends on the design and arrangement of the transformer, usually the basic patterns of the response are similar for the same type of winding [10]. The indices involved in the typical quantitative methods are calculated either in the whole frequency range or at fixed frequency sub-bands. For instance, the frequency sub-bands used for calculating the widely used R_{XY} are categorized into low frequency (10 kHz - 100 kHz), medium frequency (100 kHz - 600 kHz) and high frequency (600 kHz - 1 MHz) regions. According to the research on the dominant effect of each electrical property on the FRA response curves done by Sofian [9], a more reasonable definition of sub-bands, which divide the frequency range into 4 regions, is proposed in [9] and [29]. Region 1 ($<$ 2 kHz) is dominated by core influence, region 2 (2 kHz - 20 kHz) corresponds to the interaction between windings, region 3 (20 kHz - 1 MHz) is mainly affected by winding structure under the FRA test, and region 4 ($>$ 1 MHz) shows the effect of taps and grounding leads [29]. However, no quantitative interpretation criteria corresponding to these 4 frequency regions are given in [9], the IEEE standards [29] or other published literature.

Region 1, which corresponds to magnetizing inductance (L_m) and ground capacitance (C_g), contains essential information for the diagnosis of electrical failure modes. In order to distinguish between the influence of magnetizing inductance and ground capacitance (shunt capacitance), Velasqueza [8,96] suggested a division of frequency range with 5 sub-bands, where region 1 based on

the definition of 4 regions proposed in [9] is redivided into two sub-regions. In this way, more details relative to magnetizing inductance and ground capacitance, respectively, can be extracted separately to support the classifications of failure modes.

As claimed in the IEEE standards [29], the described 4 frequency regions are typical but not exact, and they would vary slightly depending on transformer design and arrangement. Hence, based on the typical frequency division, a method to dynamically identify the frequency sub-bands for every specific type of windings can improve the sensitivity of indices relating to transformer failure modes, thereby facilitating the development of interpretation tools for automatic assessment.

Velasqueza [8] proposed a method to adapt frequency sub-bands to each specific winding. Another research work [97] also proposed a similar method of dynamic frequency sub-bands detection. Both of the proposed methods utilize the phase plot of the frequency response to extract resonances (magnitude maxima) and anti-resonances (magnitude minima). The methods are based on the theory that the resonances and anti-resonances are accompanied by zero crossing points in the phase angle. In practice, this theory is not necessarily suited to distinguishing which peaks are resonances or not, especially in the high frequency range where the core effect is negligible. This is because, in fact, a power transformer can be represented by a complex RLC circuit as mentioned in previous chapters, the resonances and anti-resonances actually indicate poles and zeros, respectively, obtained from the high-order transfer function of the RLC circuit. In the low frequency range, the pair of L_m and C_g plays a dominant role. Whereas in the high frequency range, the core effect is negligible, the circuit can be regarded as a connection of many pairs of series capacitance between discs or turns and the winding inductance, and the impedance of each pair is much smaller compared with the impedance of L_m and C_g. Since there are many LC pairs in the circuit, once one LC pair resonates at a certain frequency, the others could not. That is why lots of small peaks are observed in the high frequency range. They are in fact poles and

zeros, but their corresponding phase angles don't necessarily cross the zero.

In this chapter, a Hierarchical Dimension Reduction classifier (HDR classifier) is proposed to identify the conditions of power transformers automatically based on FRA measurements. This proposal contains several procedures. Firstly, image processing technologies including image binalization and binary erosion, are utilized to preprocess the measured FRA data for the purpose of optimizing the input data set for the further processing. This procedure can improve the sensitivity of calculating the employed statistical indices. Secondly, combined with the preprocessed data, a new approach of dynamic division of frequency sub-bands is proposed on the basis of the suggestion of 5 sub-bands. Then, together with two conventional quantitative indices, CC and σ, two new algorithms of indices, the Area Ratio Index ARI and the Angle Difference AD, are applied as key components the algorithms of the hybrid indices. The two proposed indices are designed primarily for identifying the condition under different remanence (DRC), failure mode of short-circuit between turns (SCTFM) and failure mode of open circuit in a winding (OCFM). The hybrid quantitative indices make the respective advantages of each employed index complementary to each other, so that the dimensions of the measured FRA data can be reduced to several expected dimensions which disclose key information for the classification. Finally, according to the extracted information, the transformer conditions revealed in the FRA data can be classified, which support the further maintenance schedule.

5.2 Preprocess FRA Data

The FRA data are usually represented in diagrams for visual evaluations. The crux of interpreting frequency responses is to extract characteristic information from the sections with clean-cut deviations in FRA diagrams. 'Deviation' means the difference between the reference frequency response curve and the suspected frequency responses curve. In order to direct the focus of quantitative analysis onto these sections of the FRA curves, Mathematical

Morphology (MM), which is a powerful nonlinear tool for image and signal processing, is applied to preprocess the FRA data in this section.

5.2.1 Mathematical Morphology (MM)

MM, which is based on set theory, is commonly used to extract shape features from objects. The object could be one dimensional or multidimensional, in binary or gray scale. MM was first introduced in 1964 [98] to solve problems in petrography and mineralogy by using a set formalism, such as unions, intersections, complementation and translations to analyze binary images. Until middle 1970s, MM dealt essentially with binary images, and a number of binary operators and techniques are developed, such as erosion, dilation, opening, closing, etc [99]. With the continuous development for several decades, MM has become a powerful tool for signal and image processing, especially for geometrical shape analysis. Techniques and applications of MM has been equally boosted. Well-established MM techniques are wildly used in various industries and research fields, such as visual inspection and quality control, optical character recognition and document processing, material science, geosciences, and life sciences [99].

The main notion of MM is to extract relevant structures of an image (a set) by probing the image with a simple shape called structuring element (SE). The morphological operators decide how the SE fits or misses the shapes in the image. The shape of the SE is pre-defined according to some a priori knowledge about the shape of the image. There are two basic morphological operators derived from Minkowski set theory, dilation and erosion.

In this thesis, binary erosion is employed as a filter to extract major areas with distinct deviations between 'reference' and 'suspected response' curves in the FRA images. The basic effect of the erosion operator on a binary image is to erode away the boundaries of regions of foreground pixels (i.e. white pixels where the value equals 1, typically). The direct visual impact is that the areas of foreground pixels shrink in size, and holes (i.e. black pixels where the value equals 0, typically) within those areas become larger.

Since a binary image is a digital image that has only two possible values for each pixel, it is very convenient to describe a binary image using the concept of a set. A binary image can be regarded as a set of pixel locations and corresponding values, which can be denoted as A with components $a = (a_1, a_2)$, where a_1 and a_2 present the pixel locations. A SE is regarded as a set B with components $b = (b_1, b_2)$. The basic image operations, translation and reflection, are defined as following:

- *Translation*

The translation of A by $x = (x_1, x_2)$, denoted by $(A)_x$, is defined as:

$$(A)_x = \{c | c = a + x, \forall a \in A\}. \tag{5.2.1}$$

- *Reflection*

The reflection of A, denoted by $\check{A}$, is defined as:

$$\check{A} = \{x | x = -a, \forall a \in A\}. \tag{5.2.2}$$

The erosion of binary image A by structuring element B is mathematically defined by:

$$A \ominus B = \bigcap_{b \in \check{B}} (A)_b = \bigcap_{b \in B} (A)_{-b} = \{x | x = a - b, a \in A\}, \tag{5.2.3}$$

where, $\ominus$ is the erosion operator.

Another straightforward understanding of the erosion operator is that moving the origin of SE inside the input image A, a foreground pixel in the input image changes to background if it has a background pixel as overlapped with any pixel in the SE. Two examples of erosion with different shapes of SE are shown in Fig. 5.1. A in (a) is the image being processed, B is the SE with the shape of 'corner' and C is the SE with the shape of 'rectangle'. $\check{B}$ and $\check{C}$ are the reflection of the SEs. Figure 5.1 (b), (c) and (d) illustrate the translations of A by each component. According to equation (5.2.3), the erosion is the intersection of the corresponding translations. Thus, the erosion of A by the SE B is shown in Fig. 5.1 (f) which is the intersection of (b), (c) and (d), and the erosion of A by the SE C is shown in Fig. 5.1 (h) which is the intersection

of (c) and (d). It can be found that the SE determines the precision of the erosion on the image. Erosion can be thought of as a shrinking procedure of the input image.

5.2.2 Application of MM to Preprocessing FRA Data

The original FRA data are a set of discrete data points organized by frequencies. Hence before applying binary erosion, it is necessary to transform the input data into a digital binary image with a consistent size for all data points as pixels. Another purpose of transforming the input data into a digital image is to re-scale the FRA diagrams. FRA results can be presented in different types of diagrams using different combinations of linear and logarithmic scales of the abscissa and ordinate for visual evaluation. The presentation of diagrams depends on which range of amplitude or frequency is of special interest. Logarithmic scales of amplitude in dB (y axis) are preferable for observation of overall deviations of amplitude, while linear amplitude scales (y axis) are more suitable to observe details within a frequency range of higher amplitude values. Similarly, logarithmic frequency scales (x axis) have equal weight of all decades of frequency range, thereby showing overall information in a compact space (frequency dimension); while a linear frequency scale emphasizes on the high frequency range. Therefore, double logarithmic scales are appropriate for getting an overview of FRA results. All the FRA data used in this chapter are amplitude vs. frequency (voltage ratio transfer function) curves with double logarithmic scales. This type of diagrams is the most frequently used form in FRA interpretation, eg. Fig. 5.2(a). In general, a visual comparison of two FRA curves often depends on the amplitude deviations as well as angular shift of key resonant or anti-resonant peaks, similar to the aforementioned FRA interpretations in Chapter 4. In terms of angular deviations, observation and calculation based on linear coordinates make more sense for visualized evaluation. Hence, in order to serve the calculations of the involved indices which are proposed in later sections, the curves are marked by pixel positions in the digital images with linear in x and y axes, e.g., Fig. 5.2(b).

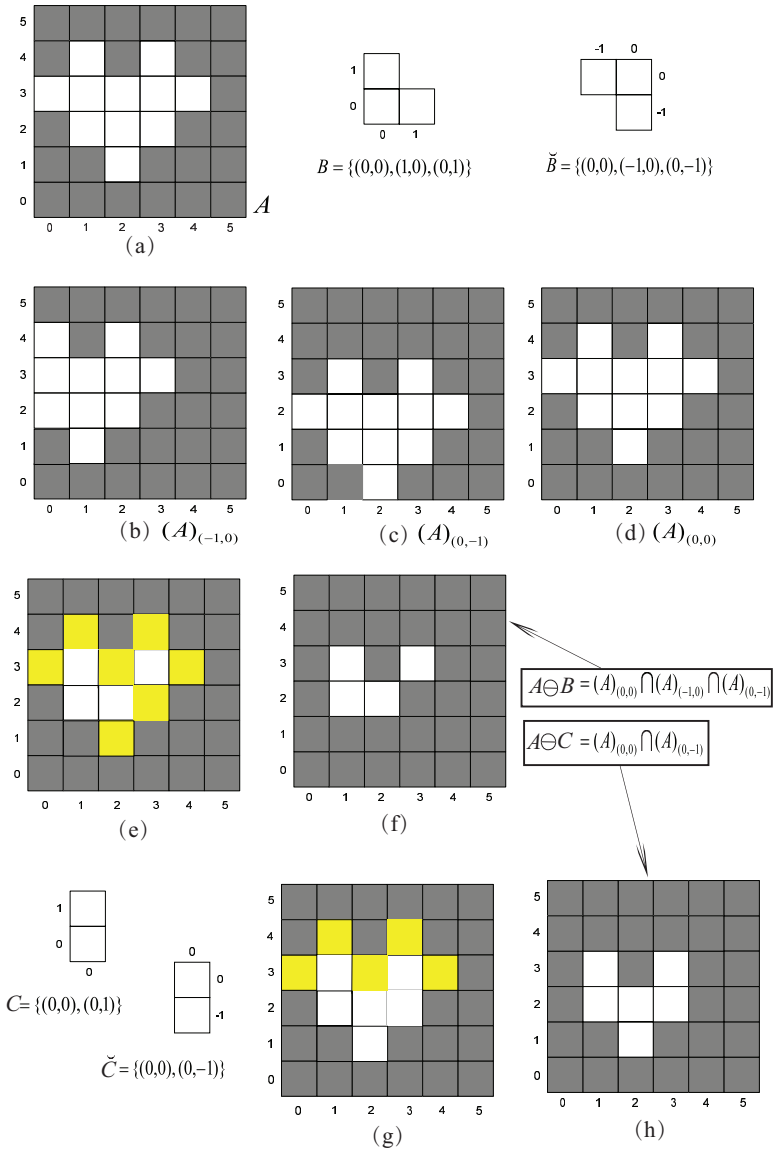

Figure 5.1: Erosion in a binary image by two given structuring element (SE)

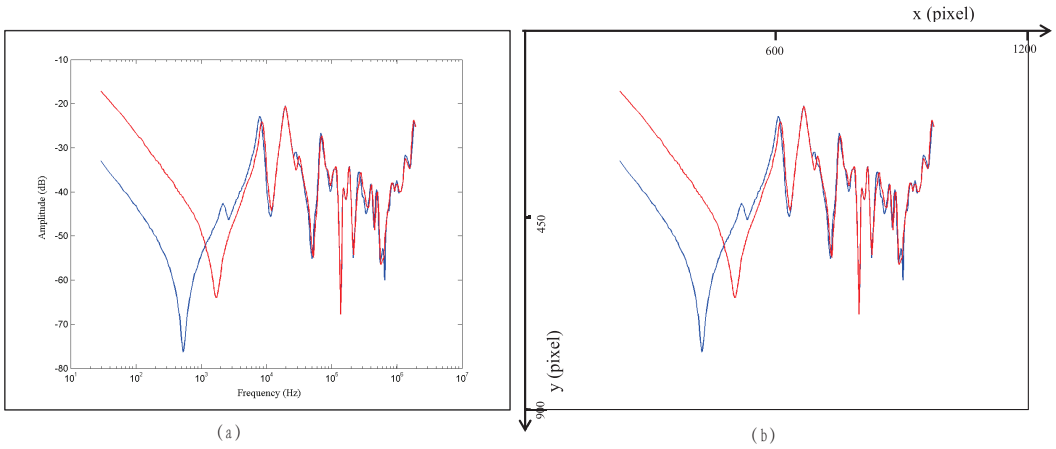

Figure 5.2: Examples of (a) Amplitude (dB) vs. Frequency Diagrams (b) Re-marked by pixel positions in linear coordinate system

First of all, save the FRA diagram as a uniform size of a RGB image to extract two sets of pixel potions of the FRA curves (the coordinate system is denoted as (px,py)) and their correspondence to the original coordinate units (amplitude vs. frequency, denoted as (x,y)). Then a basic image processing technology, image binarization which enforces only two possible values of each pixel, is used to highlight the difference area between the two curves. In other words, the pixels between two curves is transferred to foreground by assigning the value 1 to them (color white), and set the other pixels as background pixels (color black, where the value equals 0). For instance, Fig. 5.3(a) depicts the binary image of Fig. 5.2 after conversion, in which the overlapped curves has been eliminated. In the image after binarization, all areas with deviations are highlighted. However, some minor deviations which probably arise from admissible measuring errors are negligible. The results of the pertinent statistical indices, such as CC and σ, can become more sensitive in values by calculating them without taking the data in the segments with admissible measuring errors into account, which also coincides with visual-based judgement. Hence, erosion is applied in next step to filter the areas with minor deviations.

As mentioned in last subsection, the structuring element (SE), which is an essential factor to the erosion operation, is pre-defined in terms of its size and

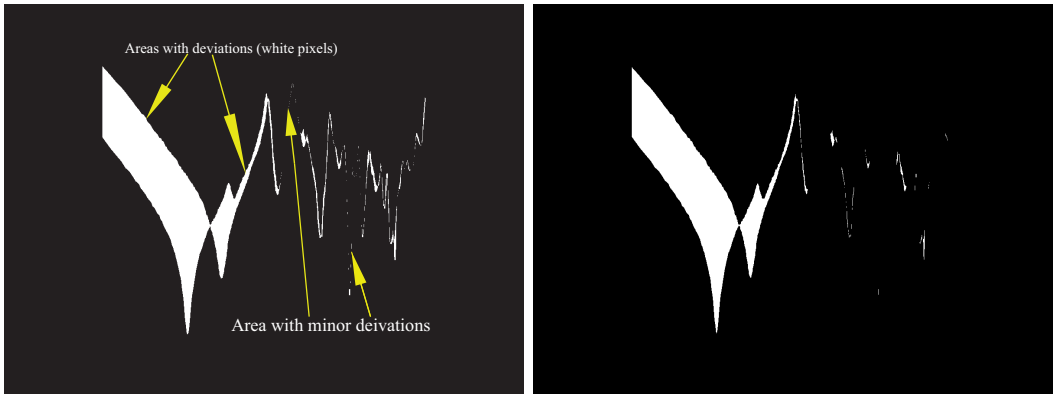

(a) FRA image after binarization (b) FRA image after erosion

Figure 5.3: Examples of image binarization and erosion

shape according to expected effect of the operation to the images. In this case, since each column of the binary image corresponds to a white (foreground) rectangular bar or nothing (background) in the binary images, it makes more sense to utilize a rectangular SE for erosion. The size of the SE is considered as a threshold value to decide how large of an area should be dismissed. With multiple testing using the 20 sets of training data mentioned in Subsection 5.5.1, the size of the rectangular SE is defined by the following equation:

$$SE = Round(0.03H) \times W, \tag{5.2.4}$$

where 'Round()' means to approximate the value by the nearest integer value, H represents the maximum pixel difference of ordinates between the curves, and W denotes the width of the rectangular SE which equals to 2 in this application. $Round(0.03H)$, which is the height of the SE, is adaptable to each frequency response diagrams with different degree of deviations. The threshold value 0.03 which is determined by the best eroded results of the training data.

Figure. 5.3(b) shows an example of an eroded image where the SE defined in (5.2.4) is used to erode the binary image shown in Fig. 5.3(a). It can be found that most of the very thin areas with minor deviation are removed. The retained sections after erosion corresponds to the frequency ranges in which deviations between two curves are distinct. Thus, the original FRA data or

re-marked FRA images are filtrated. In further stage, the related indices will be calculated only in the retained sections, so that the calculated values are more sensitive to the difference (deviation) between the reference and suspected response curves. It will be further explained in Subsection 5.4.1. In addition, the automatic division strategy of frequency sub-bands, which is introduced in next section, also takes the advantage of eroded results.

5.3 Automatic Division of Dynamic Frequency Sub-bands

5.3.1 Typical Frequency Sub-bands Structure of FRA Diagrams

As mentioned in Section 5.1, typical quantitative assessment is usually conducted with fixed frequency sub-bands [42, 51, 100]. An advanced method proposed in [9] to divide the frequency range considers the links between the FRA diagrams and the electrical components of transformers. It has been briefly introduced in Section 5.1. Based on this, an improvement on frequency range division is suggested in [96] and [8], which is able to distinguish the effect of magnetizing inductance and ground capacitance. The spectra is normally divided into 5 sub-bands as illustrated in Fig. 5.4 [8].

The typical values of sub-band boundaries and their relations with the electrical parameters are listed in Table 5.1. The sub-band LF1 is usually counted from the starting frequency point in the test to where the linear region ends, and the response in this region is mainly controlled by the magnetizing inductance (L_m). The apparent anti-resonance (minimum) in sub-band LF2 is dominated by a combination of magnetizing inductance and ground capacitance (or parallel capacitance C_g). The sub-band MF (C to D) is usually between 2 kHz to 60 kHz. In this range, the interaction between windings in terms of self inductance, ground capacitance and mutual couplings, as well as the connection and termination styles (eg., open/closed delta, floating/grounded)

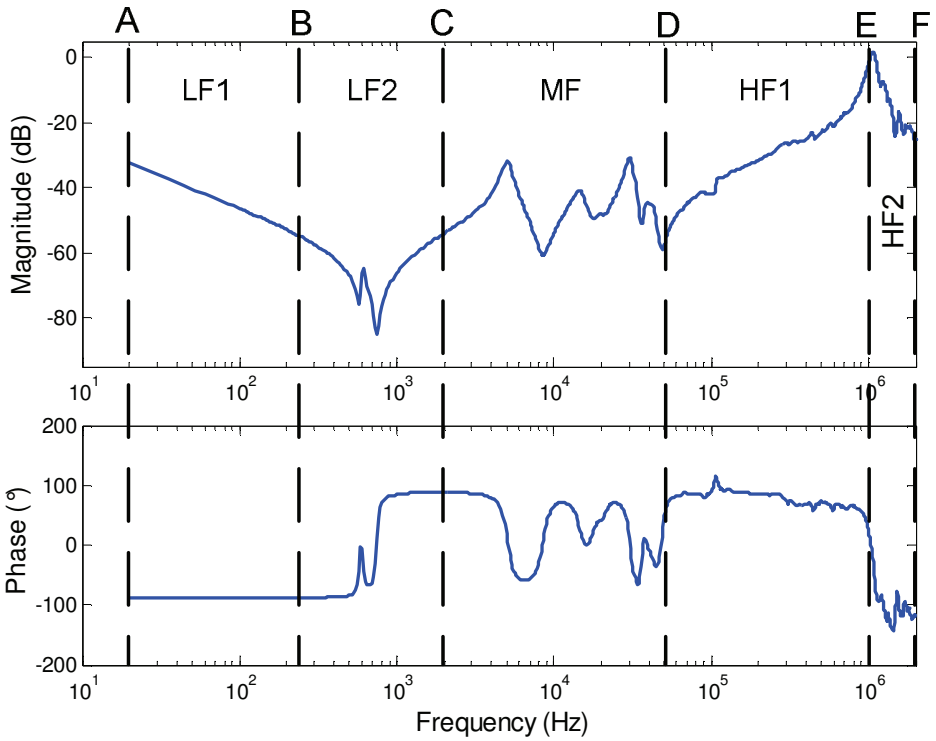

Figure 5.4: Illustration of a 5 sub-bands structure for a 150 kV winding [8]

Table 5.1: 5 frequency sub-bands and their typical values. A to F are the frequency boundaries given in Fig. 5.4

Sub-band	Range	Dominant parameters	Typical value
LF1	A-B	L_m	20 Hz - 200 Hz
LF2	B-C	L_m and C_g	200 Hz - 2 kHz
MF	C-D	interaction between windings and mutual couplings	2 kHz -60 kHz
HF1	D-E	winding structure (mainly C_s and C_g)	60 kHz -1 MHz
HF2	E-F	tap and grounding leads	$>$ 1 MHz

between windings and neutrals heavily influence the frequency response. In the sub-band HF1 (D to E), usually up to 1MHz, the frequency response is mainly affected by the winding structure [29]. It mainly depends on the series

capacitance (C_s), and normally in HV windings where the series capacitance is high for uniform distribution of voltage along windings, the response shows a mainly capacitive rising trend. Response in the last sub-band which is usually beyond 1 MHz is complex and highly influenced by the tap leads and grounding leads of the measurement setup.

5.3.2 Strategy for Automatic Division of Dynamic Frequency Sub-bands

A generalized sub-bands structure with the typical values of frequency boundaries are illustrated in Subsection 5.3.1, but the patterns of frequency responses to each specific transformer vary according to their design and interconnection. For example, the frequency response illustrated in Fig. 5.5(a) corresponds to a 300 MVA 400/220 kV autotransformer, and the frequency response in Fig. 5.5(b) is from a 52.5 MVA 240.5/12 kV power transformer. The apparent anti-resonance valley decided by L_m and C_g is 200 Hz in Fig. 5.5(a), but 500 Hz in Fig. 5.5(b). Besides, the patterns from different families

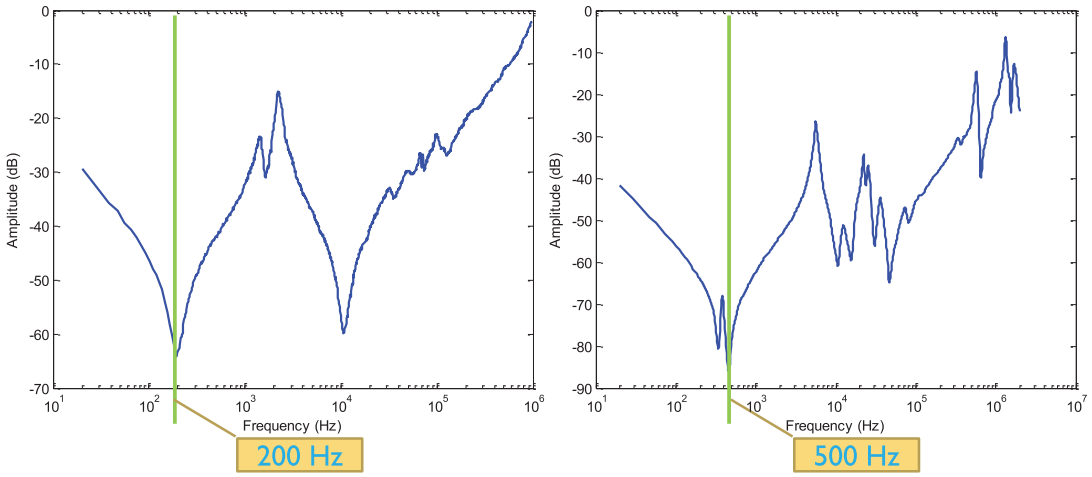

Figure 5.5: Frequency Responses of (a) 300 MVA 400/220 kV autotransformer and (b) 52.5 MVA 240.5/12 kV power transformer

of transformers have different characteristics due to the type of windings, the

winding forms of transformers (core-form, shell-form, etc.), the phase connection configurations and so on. A characterization of typical FRA patterns was conducted in [10], showing that the boundaries of frequency sub-bands cannot be exactly defined indeed. An improved and uncomplicated approach to adapt the frequency sub-bands to each specific frequency responses is proposed in this chapter. This approach is based on the sub-bands structure, but not the exact width mentioned above, and a careful analysis of the frequency response patterns of multiform transformers. Only FRA magnitude plots are required in this method.

For the low frequency range, LF1, the key feature of FRA curves is that it usually begins with an almost linearly decreasing amplitude of 20 dB/decade due to the magnetizing inductance of the core [29]. For some connection configurations, it is at least smooth and dominant by total inductance. This is then followed by a minimum which is the key feature in sub-band LF2. This minimum, marked as Z_m, occurs due to the series resonance between L_m and C_g. Hence the boundaries B and C (referring to Fig. 5.4) should satisfy the conditions that keep the potential linear part in LF1 and contain the minimum in LF2. Through the analysis of a variety of FRA curves, the boundaries B and C can be determined by following the flowchart illustrated in Fig. 5.6.

The essential strategy of this division method is to find the minimum point Z_m. Typically, Z_m is the minimum point of the whole curve, but for some secondary or low voltage windings, drastic oscillations can occur at high frequencies. In this regard, points lower than Z_m would likely exist at high frequencies. In order to eliminate the disturbance caused by these points, only the first three valleys are compared without counting the valleys at comparatively higher frequencies. After finding out Z_m, the peak next to point Z_m can be located for defining the upper boundary of LF2, C. This peak is marked as P_m. The sub-band LF1 begins at the starting point of the measurement, so $A = F_{start}$. The upper boundary of LF1, B, is defined as $B = \frac{1}{2}(A + Z_m(x))$, and the upper boundary of LF2, C, is defined as $C = \frac{1}{2}(Z_m(x) + P_m(x))$.

The feature of FRA patterns in sub-band MF usually presents multiple

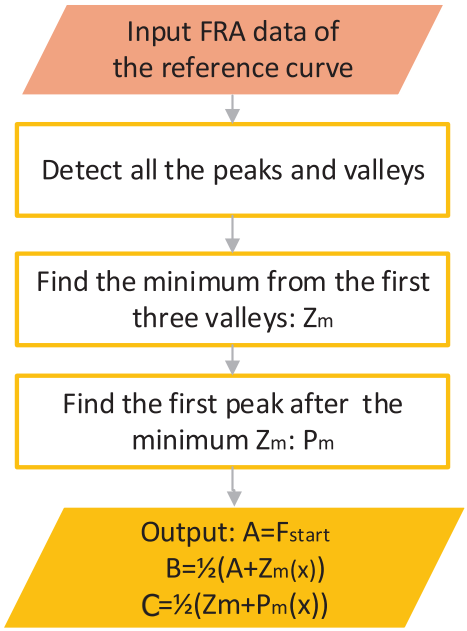

Figure 5.6: Strategic flow chart of algorithm for decision of low frequency sub-bands boundaries, B and C

oscillations in this range. Then the feature of the following high frequency range is often known as rising trend with damped oscillations typically due to high series capacitance C_s compared to ground capacitance C_g. However, for middle-voltage (MV) or low-voltage (LV) windings, C_s is not required to be that high in design. The FRA patterns of these windings at high frequencies do not show capacitive rising trend, such as the frequency response of a LV winding depicted in Fig. 5.7. Therefore, the boundaries D and E are hard to determine. For this reason, a semi-dynamic approach is proposed in this section to define the boundaries D and E compromised for more general FRA patterns. This approach is based on the typical fixed values shown in Table 5.1 and retained sections after erosion. This procedure also attempts to avoid separation at the middle of a continuous section with distinct deviation into two sub-bands. The reason to do so is that in most cases, the deviations in the nearby areas in the FRA patterns usually arise from a chain effect of the same electrical component. If the section with these deviations is separated in

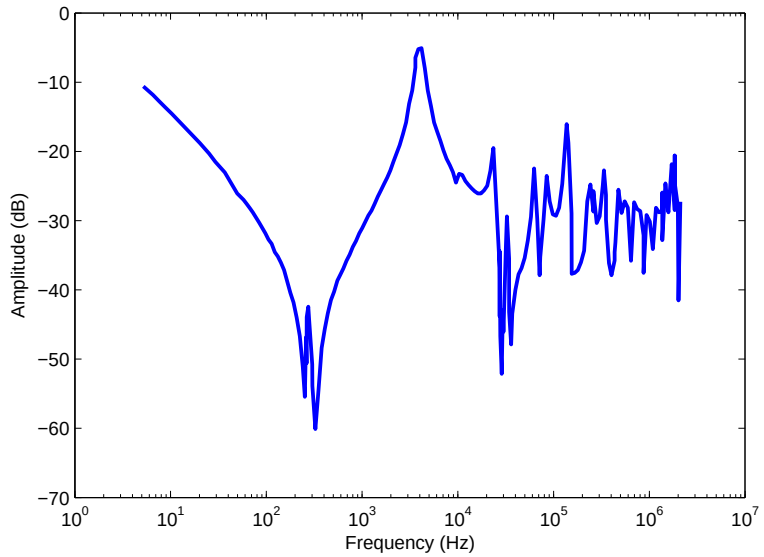

Figure 5.7: Frequency response of LV winding in a double-wound transmission transformer

two sub-bands, the calculation results of relevant statistical indices could be compromised.

Figure. 5.8 shows the idea of adjusting the boundaries D and E using this approach. This picture is a part of a frequency response plot after erosion. On the basis of the typical boundary values shown in Table 5.1, the boundaries D and E are adjusted slightly according to the retained deviation areas. The strategic algorithms of this approach is shown in the flow chart in Fig. 5.9. The basic idea is to search a break column where all the pixels in this column is black (value 0) in the (px,py) coordinate (mentioned in Subsection 5.2.2) from higher to lower (right to left) in a predefined range of frequencies around the fixed boundary (Table 5.1). If the break column exists, then the corresponding frequency is then defined as the boundary. If white area (deviation) is continuous across the predefined range, the default value is used as the boundary. The upper boundary of sub-band HF2 equals to the last measured frequency F_{end}. If F_{end} is smaller than 1.2 MHz, sub-band HF2 will no longer exist due to limited measuring range.

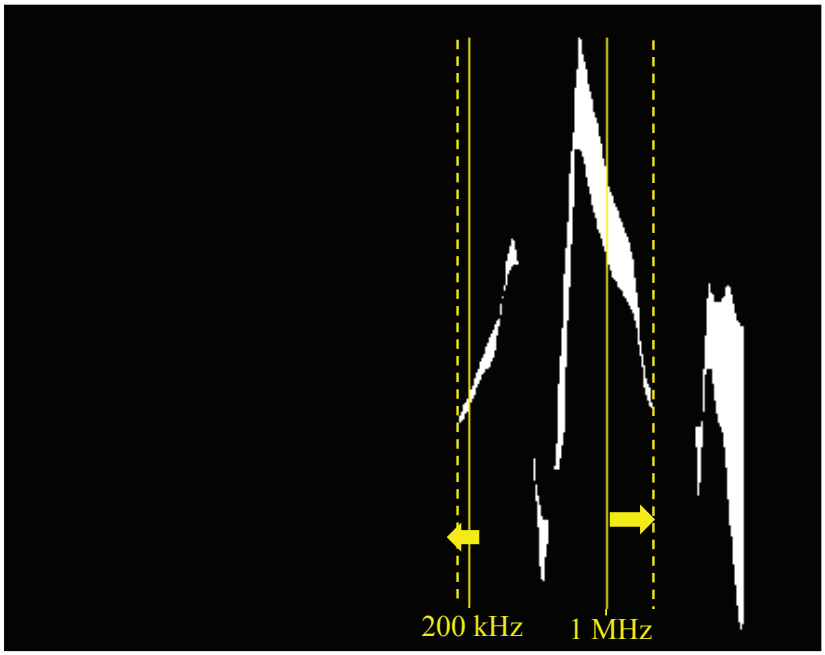

Figure 5.8: Idea of adjustment of boundaries D and E

5.3.3 Implementation and Summary

The algorithms are implemented in Matlab, and the performance is validated in various cases of FRA plots (20 sets of training data mentioned in Subsection 5.5.1). Examples of automatic division of dynamic frequency sub-bands for the real FRA plots of four different transformer windings are illustrated in Fig. 5.10. The results agree with the proposed sub-band structures, especially in low frequency range. Since the search direction is from right to left (high to low in frequency), the cases that have no distinct deviation in the searching range or around the upper bound of the searching range would cause that the upper bound of the searching range becomes the boundary of the corresponding sub-band, eg., Fig. 5.10(d). The sub-band division results of these cases could look not that accurate at high frequencies, especially the boundary between MF and HF1. However, it won't affect the evaluation of statistical indices involved in this chapter because the calculations are only conducted in

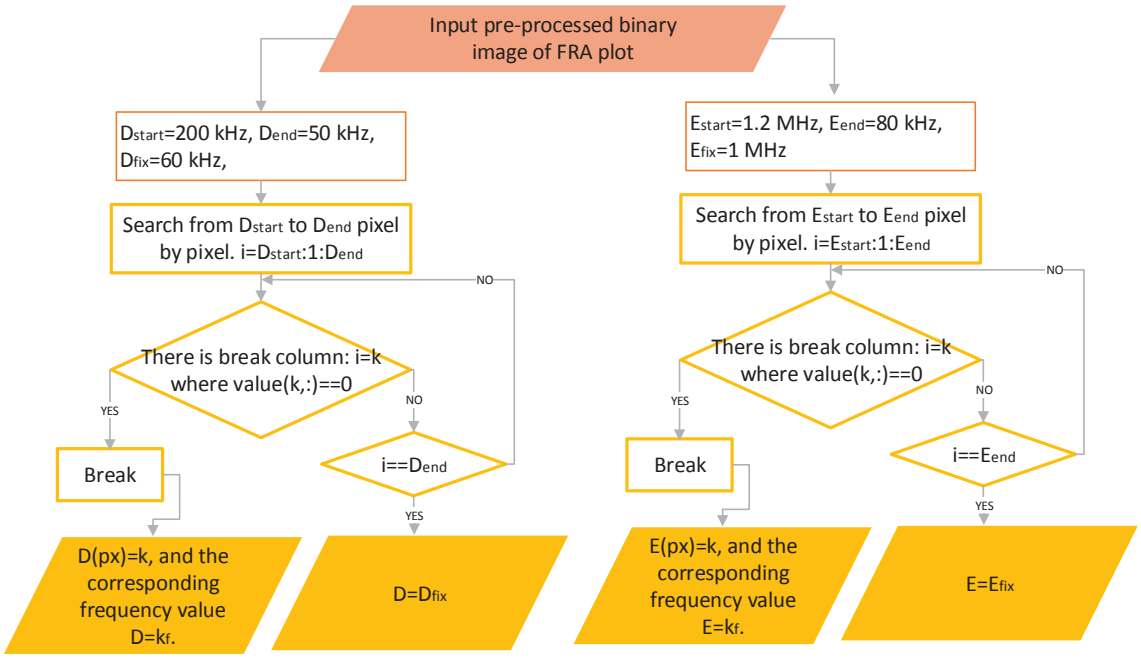

Figure 5.9: Strategic flow chart of algorithm for decision of middle and high frequency sub-bands boundaries, D and E

the filtered area with deviation.

In conclusion, this section offers algorithms for automatic division of the dynamic frequency sub-bands based on the theory of 5 frequency sub-bands structures. The algorithms are uncomplicated and easy to be implemented. Besides, the only data needed to carry out this division method are FRA magnitude plots. This method shows good performance on adapting frequency sub-bands to each specific frequency responses of multiform transformers, especially in low frequency range (see Fig. 5.10), which is essential to detect electrical transformer failure.

5.4 Evaluation Indices for Hierarchical Dimension Reduction (HDR)

A FRA diagram actually describes a set of multi-dimensional data. After preprocessing the FRA data and dividing the data into 5 groups, the next step

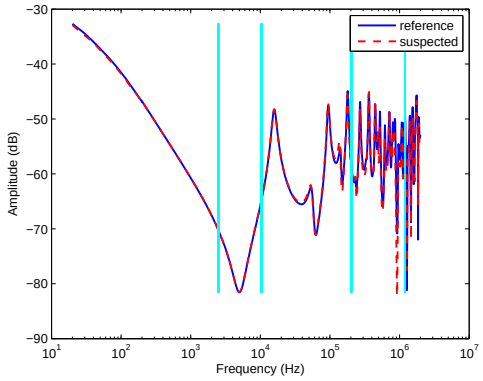

(a) 10 kV Winding of a 50 kVA transformer

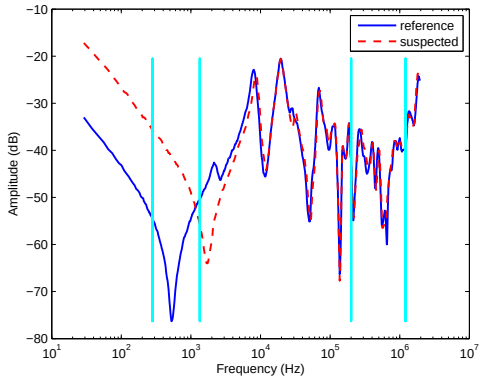

(b) 220 kV Winding of a 140 kVA auto-transformer

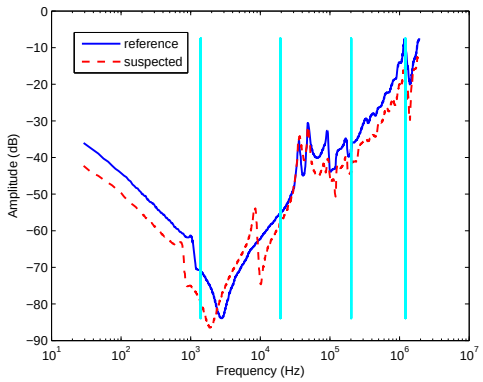

(c) Data reprint from [29], configuration not clear

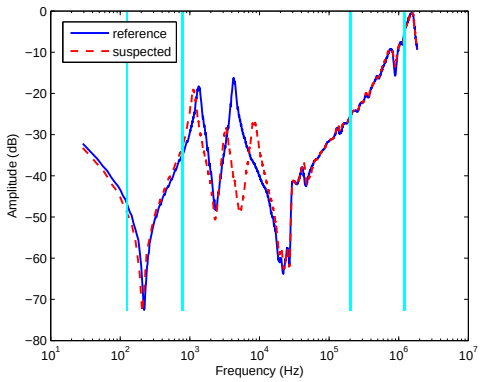

(d) 220 kV Winding of a 100 kVA transformer

Figure 5.10: Examples of automatic division of dynamic frequency sub-bands for the real FRA plots

needs to think about how to reduce the dimensions of FRA data so that useful information can be extracted for the final classification. Using hybrid indices (combined use of different kinds of indices) is a good strategy to effectively extract key information from the input data. Among classic statistical indicators, correlation coefficients (CC) and Spectrum Deviation (σ or SD) are selected as a part of the hybrid indices due to their uniform normalization of values and widely approved usage [32, 42, 93]. The main drawback of these indicators is that each of them is not sensitive to a certain kind of deviations between two

curves. Thus, to cover the deficiency of these two indicators, apart from these two classic statistical indicators, two new algorithms of indices on the basis of prior knowledge are proposed and implemented as the other part of the hybrid indices. These new indices are primarily designed to identify electrical failure modes and assess condition of residual magnetization, since by using CC and σ only electrical failure modes and residual magnetization are hard to be identified from each other.

All relevant indices are introduced in this section. The algorithms of HDR are proposed together with the classifier in next section.

5.4.1 Implemented Statistical Indices

The hybrid indices used in research include 4 types of indices. The correlation coefficient (CC) is defined by equation (5.4.1) [32, 42, 101], and the Spectrum Deviation (σ) is defined by equation (5.4.2) [4, 35, 93].

$$CC(X,Y) = \frac{\sum_{i=1}^{N} x_i y_i}{\sqrt{\sum_{i=1}^{N} x_i^2 \cdot \sum_{i=1}^{N} y_i^2}}; \tag{5.4.1}$$

$$\sigma(X,Y) = \frac{1}{N}\sum_{i=1}^{N}\sqrt{\left(\frac{x_i-(x_i+y_i)/2}{(x_i+y_i)/2}\right)^2+\left(\frac{y_i-(x_i+y_i)/2}{(x_i+y_i)/2}\right)^2}; \tag{5.4.2}$$

where vectors $X = \{x_1, x_2, \ldots, x_N\}$ and $Y = \{y_1, y_2, \ldots, y_N\}$ denote the values on ordinate of two frequency responses (in the (px,py) coordinate system) and N is the number of pixels on abscissa corresponding to the observed frequency interval.

CC is used to evaluate the similarity between the two sets of data X and Y. Theoretically the interval of CC is [-1, 1]. The more similar X and Y are, the closer to 1 CC gets; when X and Y are completely different, $CC = 0$; when X and Y are opposite in sign, CC becomes negative. In this application, X and Y are defined in the (px,py) coordinate system, so the practical interval is normalized in [0, 1]. σ is a normalization equation to measure the deviation

between X and Y with an interval of [0, 1]. When X and Y are similar to each other, σ approaches 0.

Instead of using all sets of data to calculate CC and σ, the novelty of applying these two statistical indices in this thesis is that only the data within the retained segments after erosion are used for the calculation. In this application, if the deviation is not significant in the whole set (the FRA diagram), the corresponding area will be filtered during the preprocessing, then the default value is 1 for corresponding CC and 0 for σ. If there is significant deviation in an area, take the value of CC as an example, the calculated value will be smaller than the conventional calculation based on all sets of data. This indicates that the sensitivity of calculating the statistical indices CC and σ is improved. Moreover, the indices are calculated at 5 frequency sub-bands that are proposed in Section 5.3 rather than at fixed frequency sub-bands.

5.4.2 New Indices for Low Frequency Sub-bands

This subsection proposes two new indices for evaluating deviation in the low frequency sub-bands. The purpose of these two indices is to effectively support the identification of DRC, SCTFM and OCFM.

Area Ratio Index (ARI)

The common deviation in sub-band LF1 is vertical displacement. This kind of characteristic deviation usually occurs when the winding under test is in different remanence condition, or when some kind of electrical faults appears, i.e short-circuit between turns and open circuit in a winding. CC is not sensitive to vertical changes. Although σ can detect this kind of deviation, the calculated value of σ cannot detect the degree of deviation explicitly. In other words, by calculating σ for this case above (LF1), it is difficult to define a threshold value for the purpose of the classification. Besides, the calculations of σ and CC do not have the ability of differentiating whether the curve is shifting upwards or downwards with reference to the reference curve. The shifting direction (upwards or downwards) in sub-band LF1 also contains vital

information to classification. In consequence, to cover these deficiencies of CC and σ in sub-band LF1, a new index, Area Ratio Index (ARI), is designed to differentiate the changing directions of curves and reflecting the degree of vertical deviation in quantitative manner. This index is specially designed for sub-band LF1 where the curves are generally linear or smooth.

The definition of Area Ratio Index (ARI) is:

$$ARI(X,Y) = \frac{\sum_{i=1}^{N}(y_i - x_i)}{\sum_{i=1}^{N}(MAX - min(x_i, y_i))}, \tag{5.4.3}$$

$$MAX = max\{max(X), max(Y)\}, \tag{5.4.4}$$

where $X = \{x_1, x_2, \ldots, x_N\}$ and $Y = \{y_1, y_2, \ldots, y_N\}$ denote vertical pixel positions (py) of two frequency responses (in (px,py) coordinate system) and N is the number of pixels in horizontal axis that corresponds to the maximum frequency point.

The physical understanding of (5.4.3) is illustrated in Fig. 5.11. It can be seen that the absolute value of ARI is equivalent to the area ratio of the deviation area in LF1 (yellow (dark) area in Fig. 5.11) to the accumulated maximum area (doted area). In most of the FRA curves of the power transformer in usual use, the slope angle is similar and does not change much (eg. typically 20 dB/decade). Therefore, the area ratio can reflect the degree of deviation. The interval of ARI is [-1, 1]. The sign of ARI represents the shifting direction of the suspected curve compared to the reference curve. Take X as reference, then the positive sign means that the suspected curve Y moves below X (shifting downwards), and the negative sign means that the suspected curve Y moves above X (shifting upwards). Therefore, both of direction of change and degree of vertical deviation in sub-band LF1 are described by ARI.

ARI can accurately used to extract the information in LF1, but for some LV windings or test results under connection of end-to-end shirt-circuit (see Chapter 2), the determination of the threshold values for this index has limitations due to the flat slope angle at the beginning of the curves (much smaller than 20 dB/decade). This can be solved by adding a weighted parameter according

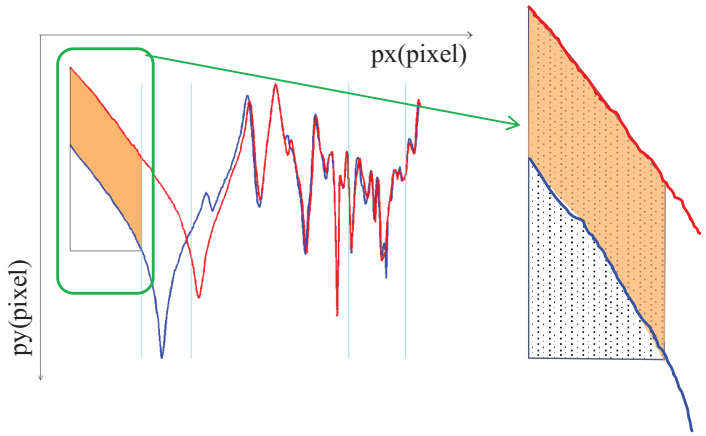

Figure 5.11: Explanation of Area Ratio Index (ARI)

to the type of the input FRA data, but it is not considered in this thesis. In future study, when the data sets can cover more types of transformer, it should be considered when determining the threshold values for ARI.

Angle Difference of the anti-resonance in LF2 (AD)

The apparent anti-resonance (minimum, Z_m mentioned in Subsection 5.3.2) in sub-band LF2 contains essential information and can be easily detected in automatic processing of data. The shift of this point effectively reflects the change of L_m or C_g or both of them. A new index, Angle Difference (AD), is designed to extract the information of the changing angle of this point, and its definition is:

$$AD = atan2d((b_1 - b_2), (a_2 - a_1)), \tag{5.4.5}$$

where $atan2d(B, A)$ represents a function of four-quadrant inverse tangent in degrees as explained in Fig. 5.12. The minimum anti-resonance of baseline in LF2 is chosen as the origin of plane, and the range of AD is $(-180°, -180°]$. $X(a_1, b_1)$ represents the pixel positions of Z_m of the reference in LF2, and $Y(a_2, b_2)$ represents the pixel positions of Z_m of the suspected curve.

The index AD is purposefully designed for coherent usage with ARI. It is only used to calculate the changing angle rather than the severe degree of

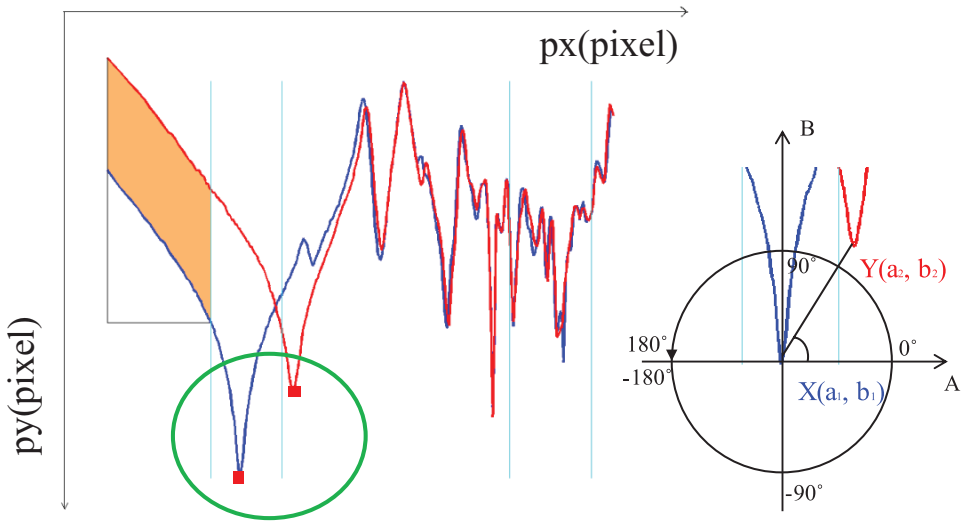

Figure 5.12: Explanation of Angle Difference (AD)

curve shift. The index ARI can reflect the change of electrical parameters which could be L_m or winding resistance R. AD can indicate the change of parameters, which could be L_m or C_g. Whereas using them together, it is able to differentiate the changed electrical parameter(s) from each other. The novelty of these two proposed indices is that as a part of the hybrid indices, they substantially increase the sensitivity of the hybrid indices at low frequencies. A combined use of ARI and AD is able to distinguish the key parameter that causes deviation at low frequency sub-bands. It consequently supports the identification of DRC, SCTFM and OCFM. The implementation of these indices will be given in the case studies.

5.5 Hierarchical Dimension Reduction Classifier

This section firstly introduces the classes of the training sets involved in this study, which is followed by the algorithms of HDR of FRA data using the hybrid indices that are introduced in the last section. A classifier called

Hierarchical Dimension Reduction Classifier (HDR Classifier) is proposed.

5.5.1 Classes of Training Sets

To implement the method of assessing FRA measurement data proposed in this thesis, 32 sets of typical FRA measured data from various transformers are collected from the published paper and dissertations which are related to the FRA interpretation. Among them, 20 sets are used for training, so that the relevant threshold values for the indices are determined. In such way, useful information can be extracted via effective data dimension reduction. Another 12 sets of the data are prepared for validating the performance of the classifier at the end. Although the population of the data sets is not particularly large, the collected data represent very typical cases of failure modes or conditions in a satisfied amount, and they are able to provide general threshold values. It was proved by using 10 random sets primarily and then adding the amount of the sets to check the obtained threshold values. The threshold values of indices can be refined by using a larger amount of training sets in further work for considering more types of transformers or measurement connection methods.

The data from the FRA measurement are either time-based or phase-based comparison. However, all the phase-based FRA data are from symmetrical phases, so the situation of healthy conditions from asymmetrical phases are not included nor considered in the evaluation of threshold values.

Based on the training sets, 5 general classes listed in Table 5.2 are included in the design of the classifier. MEFM is a class that includes all common types of mechanical winding deformation, such as axial and radial winding deformation, with the exception of lead deformation due to lack of relevant training data. OCFM and SCTFM are frequently happening electrical failure modes. DRC is not a failure mode, but this condition affects the FRA curves which could easily lead to a mis-interpretation. Therefore, identifying the phenomena of different remanence is mandatory.

Table 5.2 also highlights the characteristically affected sub-bands of each class. The cell with light background color in the column 'DRC' presents less

Table 5.2: Classes of training sets and characteristic affected sub-bands

Class	Abbreviation	Frequency Sub-band				
		LF1	LF2	MF	HF1	HF2
Mechanical failure modes	MEFM			▼	▼	
Open circuit in a winding	OCFM	▲	▲	▲	▲	▲
Short-circuit between turns	SCTFM	▲	▲			
Different Remanence Condition	DRC	▲	▲			
Healthy Condition	HC	▲	▲	▲	▲	▲

∗ Sign ▼ means logic 'OR' of the marked cells in the same column

∗ Sign ▲ means logic 'AND' of the marked cells in the same column

significance compared with the cell with dark background in the same column. Logic 'OR' means that the affected frequency sub-bands could be any one of the marked sub-bands, and logic 'AND' means that this condition affects all marked sub-bands.

5.5.2 Algorithms of Hybrid Indices for Hierarchical Dimension Reduction

This subsection introduces the procedure of the hierarchical dimension reduction of preprocessed FRA data. A general flowchart is shown in Fig. 5.13. The input is the data set of vertical pixel positions of frequency response curves in retained frequency sections after erosion. The number of the data in a set can be regarded as the number of the dimension of the data set. The value is usually in the range of a few hundreds. The procedure is described as below:

1. Divide the input data into 5 groups according to their sub-bands structure (denoted as DATA_LF1, DATA_LF2, DATA_MF, DATA_HF1, DATA_HF2), plus a group of detected points of the aforementioned anti-resonance (Z_m) in sub-band LF2.

2. These 6 groups of data are processed by following the algorithm in each

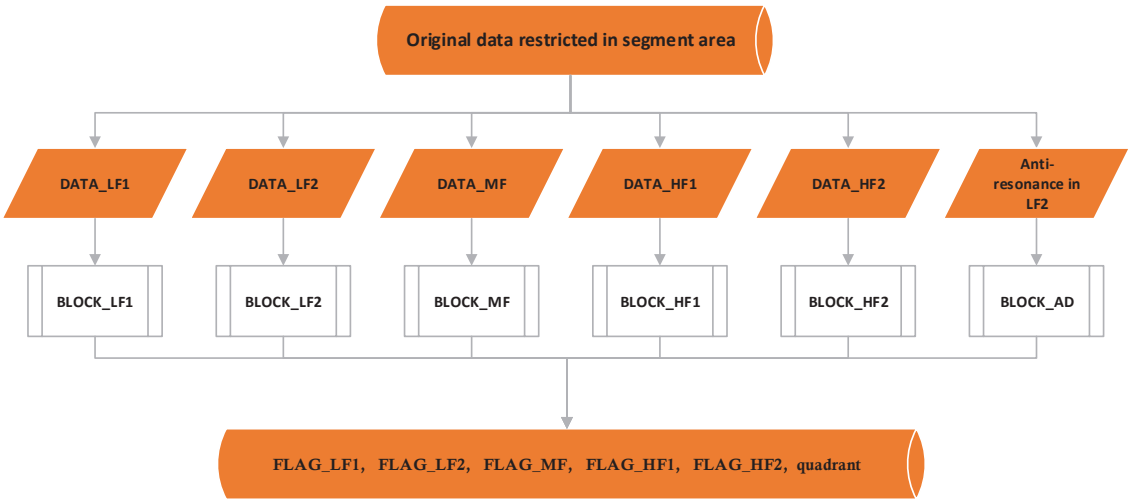

Figure 5.13: Flowchart of Algorithms of Hierarchical Dimension Reduction

block listed in Fig. 5.13.

3. After the dimension reduction, the outputs of this procedure are 6 dimensional, which are denoted as FLAG_LF1, FLAG_LF2, FLAG_MF, FLAG_HF1, FLAG_HF2 and *quadrant*. FLAG_LF1 is a 2-bits binary digit; FLAG_LF2, FLAG_MF, FLAG_HF1 and FLAG_HF2 are 1-bit binary digits; *quadrant* is an integer ranging from 1 to 4.

BLOCK LF1, which is depicted in Fig. 5.14, involves the calculated indices CC and ARI using DATA_LF1. As mentioned before, CC is insensitive to vertical changes, so CC is firstly used to detect the cases that catastrophic failure happens or if there is noise in the FRA curves that is not filtered during test. If the situation is not found, ARI is then used to identify the changing direction and the degree of vertical deviation of the curves in sub-band LF1, and the information is classified into 4 circumstances and recorded by FLAG_LF1.

In Fig. 5.15, the algorithms of BLOCK LF2, BLOCK MF, BLOCK HF1 and BLOCK HF2 are illustrated in the form of flowchart. CC and σ (or SD) are used together to judge the deviation in each sub-band, due to their

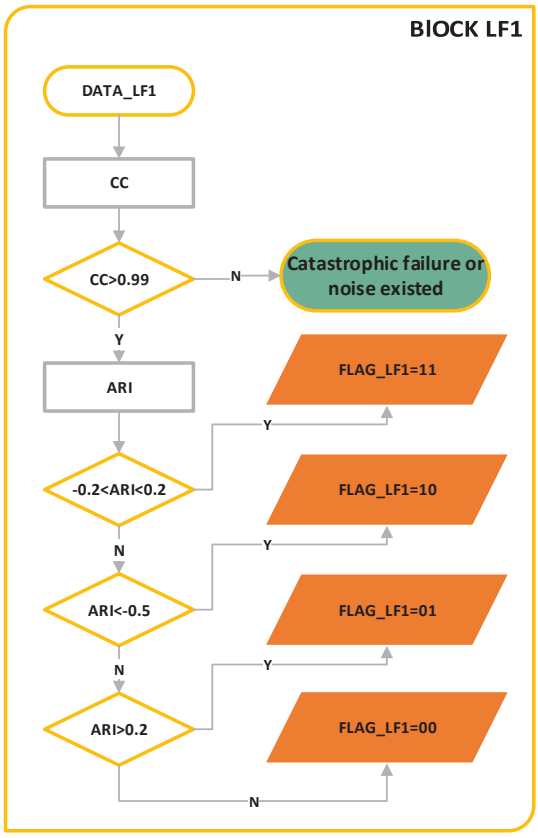

Figure 5.14: Flowchart of Block LF1

complementary sensitivities of different kinds of deviations. The information extracted in each sub-band is represented by a 1-bit binary digit, 1 means significant deviations at corresponding sub-band, and 0 means non or negligible deviations at corresponding sub-band.

BLOCK AD, which is illustrated in Fig. 5.16, simply classifies the calculated results of index AD in 4 classes. It indicates the changing quadrants of the anti-resonance in LF2.

In brief summary, the hierarchical process of dimension reduction can extract expected information from a data set with hundreds of dimensions and store the information in 6 dimensions.

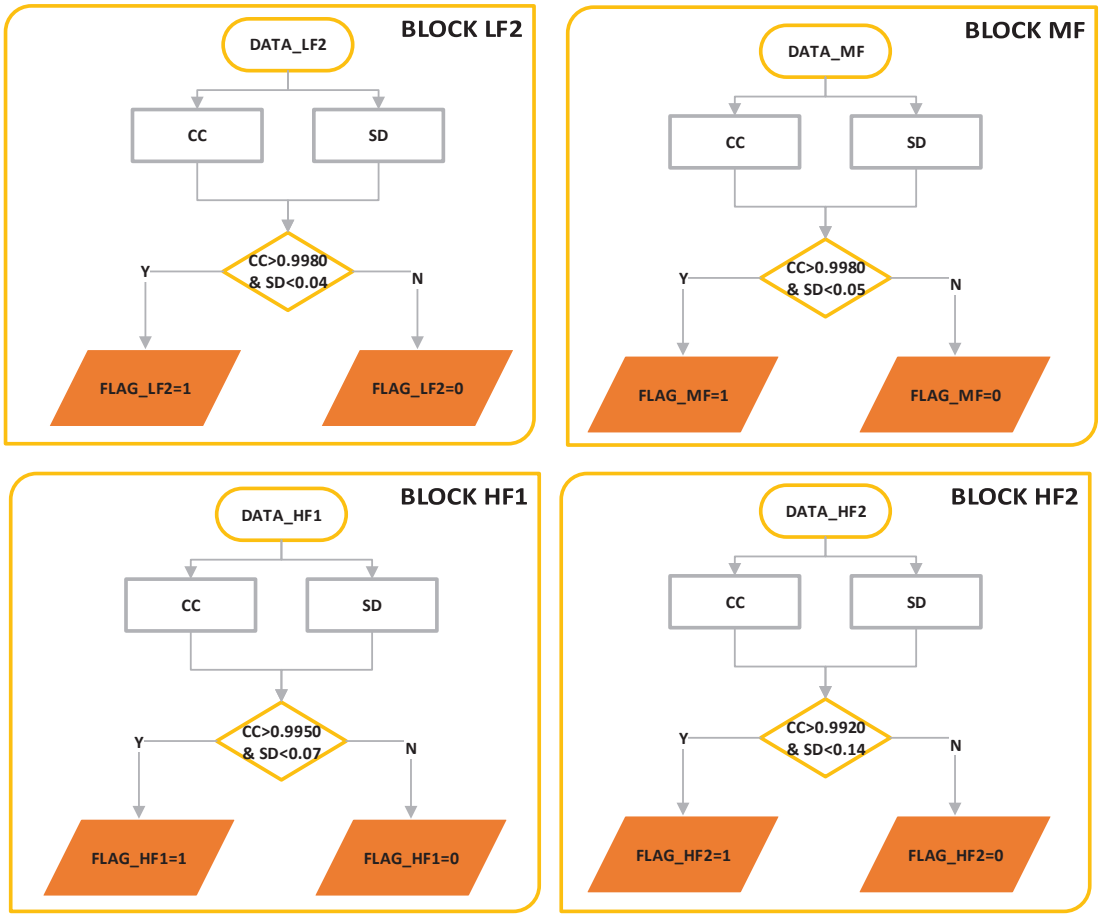

Figure 5.15: Flowchart of BLOCK LF2, BLOCK MF, BLOCK HF1 and BLOCK HF2

5.5.3 Final Classification of Failure Modes

Based on the extracted information in six dimensions, the final classification is decided by the decision map shown in Fig. 5.17. The target classes are basically the 5 classes shown in Table 5.2.

However, considering real cases, the classes of assessed conditions by HDR classifier are refined elaborately. Nine assessed conditions which are exhibited in Table 5.3 are settled in this classifier.

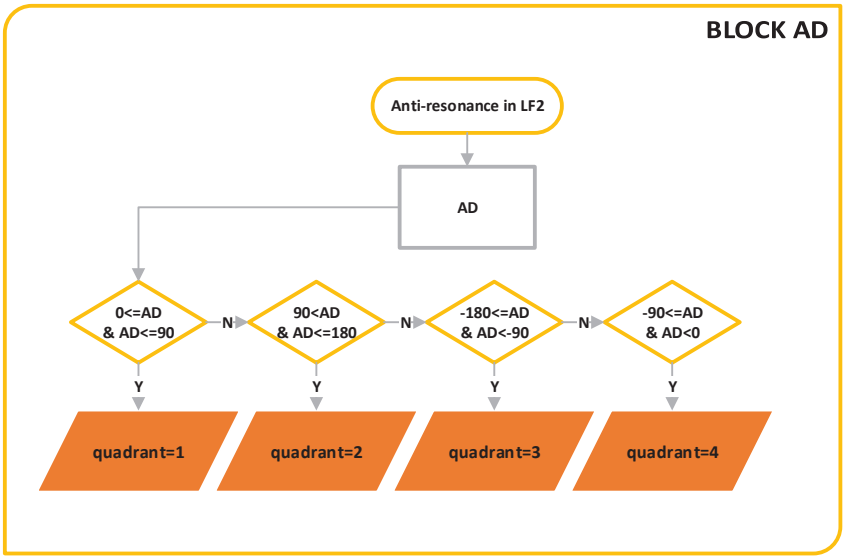

Figure 5.16: Flowchart of Block AD

Table 5.3: Assessed Conditions of HDR Classifier

A	SCTMF (Short-circuit between turns failure mode)
B	Undetectable failure mode
C	OCFM (Open circuit failure mode)
D	HC with DRC (Healthy condition with different remanence)
E	MEFM with DRC (Mechanical failure modes with different remanence)
F	DRC (Different remanence condition) with other failure modes
G	HC(Healthy condition)
H	MEFM(Mechanical failure modes)
I	Undetectable condition

5.6 Implementation of HDR Classifier

To validate the HDR classifier primarily, the aforementioned 20 sets of training data which are used to determine the size of the structuring elements and the threshold values of indices are applied in the final complete classifier. All the cases are passed successfully, which means the performance of the HDR

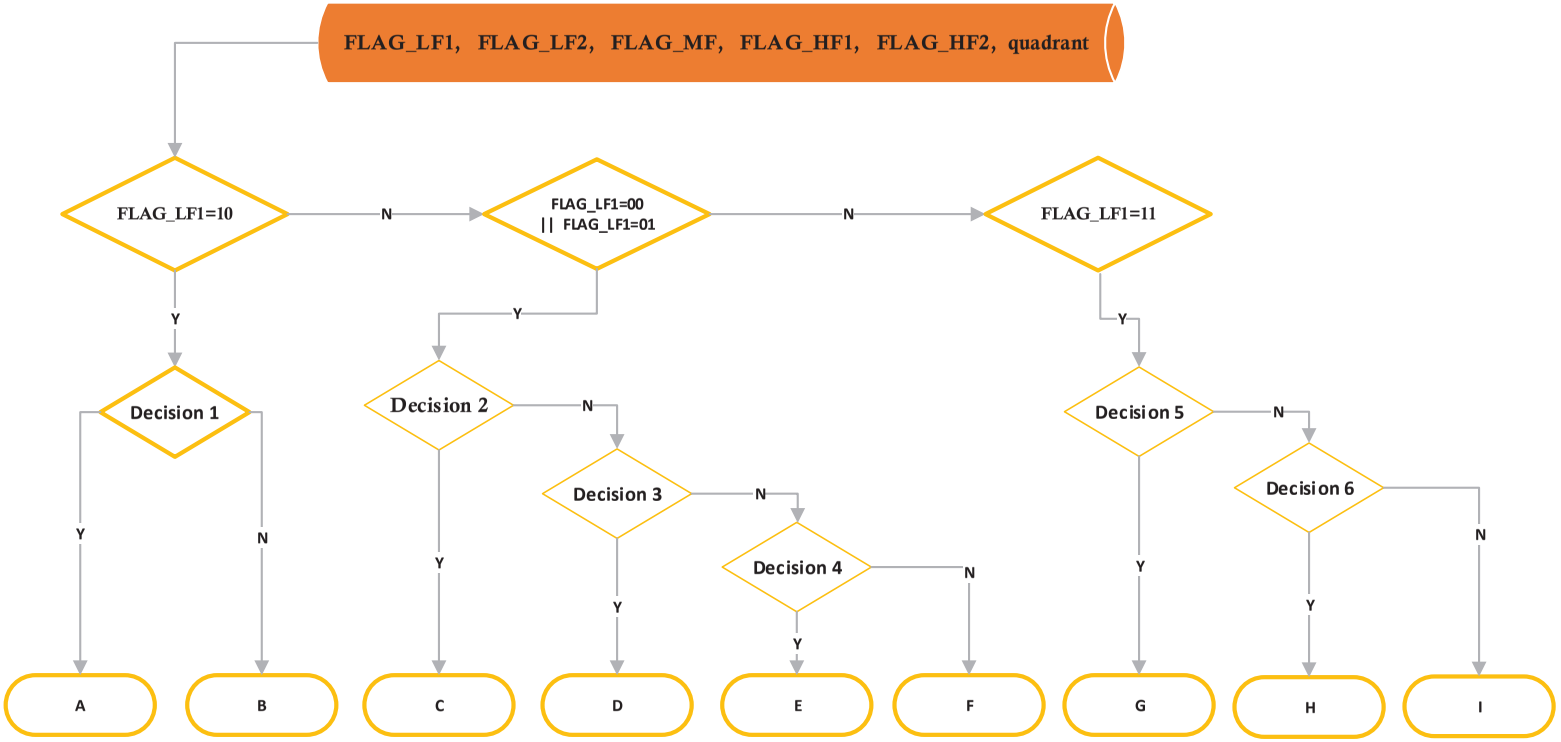

Decision 1: FLAG_LF2=0 & quadrant=1
Decision 2: FLAG_LF1==01 && FLAG_LF2==0 && FLAG_MF==0 && FLAG_HF1==0 && FLAG_HF2==0 && (quadrant==3 || quadrant==4)
Decision 3: FLAG_MF==1 && FLAG_HF1==1 && FLAG_HF2==1
Decision 4: FLAG_MF==0 || FLAG_HF1==0
Decision 5: FLAG_LF2==1 && FLAG_MF==1 && FLAG_HF1==1 && FLAG_HF2==1
Decision 6: FLAG_MF==0 || FLAG_HF1==0

Figure 5.17: Flowchart of the algorithm for final classification of failure modes

classifier in this implementation is 100% accurate. Performance of the proposed HDR classifier is further verified by the rest 12 sets of experimental data of FRA measurements. Among them, 5 typical case studies are explained in details.

5.6.1 Case Studies

These 5 cases included in this subsection are representative for the conditions listed in Table 5.3. By explaining these 5 cases, the details about the procedure of the proposed HDR classifier are revealed.

Case 1

The frequency response used in this case is collected from a 68 MVA, 240/21 kV power transformer. According to the visual diagnosis conducted by experts, the deviation in the low frequency range is caused by residual magnetism in the core (DRC), but no faults happened in this transformer. The effect of this type of condition is the increasing magnetizing inductance. Therefore, the comparison of FRA curves under this condition usually shows obvious vertical displacement in sub-band LF1 and correlative changes in sub-band LF2.

Figure. 5.18 shows the assessment results of this case by using the HDR classifier, which includes the FRA plot with frequency sub-bands and its eroded binary image. It can be seen that the deviation occurs in sub-bands LF1 and LF2. Hence FLAG_MF, FLAG_HF1 and FLAG_HF2 all equal to 1 which means no noticeable deviation is flagged. FLAG_LF1 = 01 represents obvious downward displacement in LF1, and FLAG_LF2 = 0 represents noticeable deviation in LF2. The final diagnosis result determined by the HDR classifier is **D** which means healthy condition with different remanence. This result is consisted with the visual diagnosis.

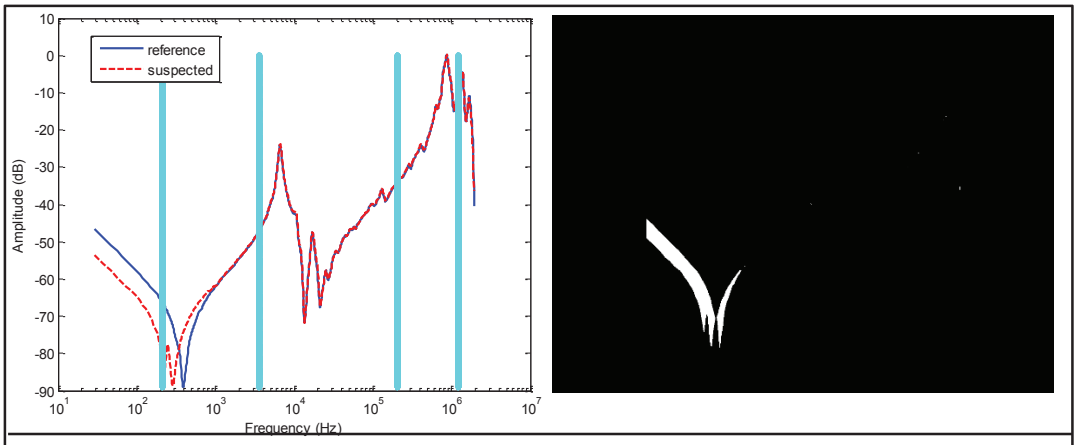

FLAG_LF1=01, FLAG_LF2=0, FLAG_MF=1, FLAG_HF1=1, FLAG_HF2=1, quadrant=2
HDR Classifier diagnosis: D
Validation: Pass

Figure 5.18: Performance of HDR Classifier: Case 1

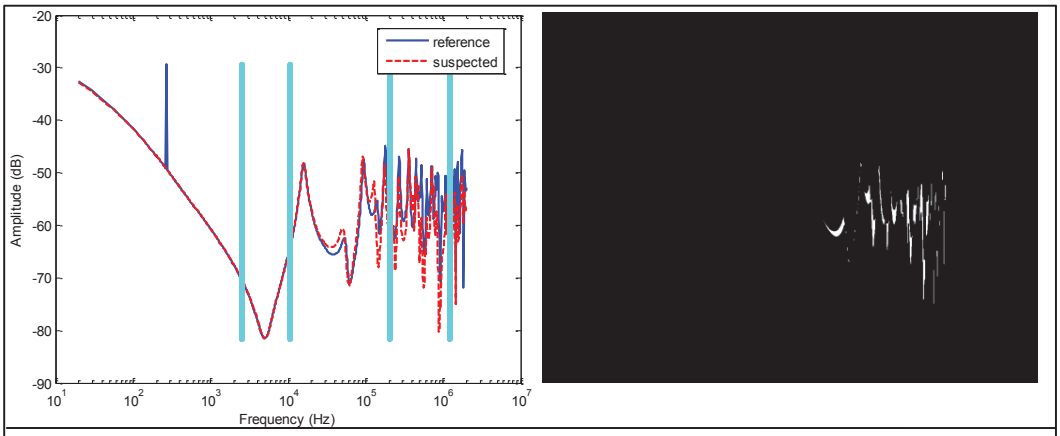

FLAG_LF1=11, FLAG_LF2=1, FLAG_MF=0, FLAG_HF1=0, FLAG_HF2=0, quadrant=1
HDR Classifier diagnosis: H
Validation: Pass

Figure 5.19: Performance of HDR Classifier: Case 2

Case 2

This case corresponds to the FRA measurements on the HV winding in phase B of a power transformer (50 kVA, 10/0.4 kV). This set of result comes

from the designed experiment introduced in Chapter 2. Details of the specifications and experimental setup can be found in Chapter 2, and it is specially designed for the minor axial displacement failure mode, which belongs to the class MEFM.

The assessment results of this case using the HDR classifier is illustrated in Fig. 5.19. The FRA plot with the boundaries of 5 frequency sub-bands and its eroded binary image are given in this figure. The final diagnosis result is **H** which agrees with the fact of the experimental setup.

Case 3

The frequency response used in this case is reprinted from [29]. The configuration of the tested transformer is not given in [29]. This frequency response diagram is shown as an example of axial winding movement (which belongs to MEFM) from tertiary open-circuit test in [29]. This type of failure mode mainly affects the FRA curves in sub-bands MF and HF1. The response to axial winding deformation is unpredictable when the frequency is higher than 1 MHz which corresponds to sub-band HF2 [29].

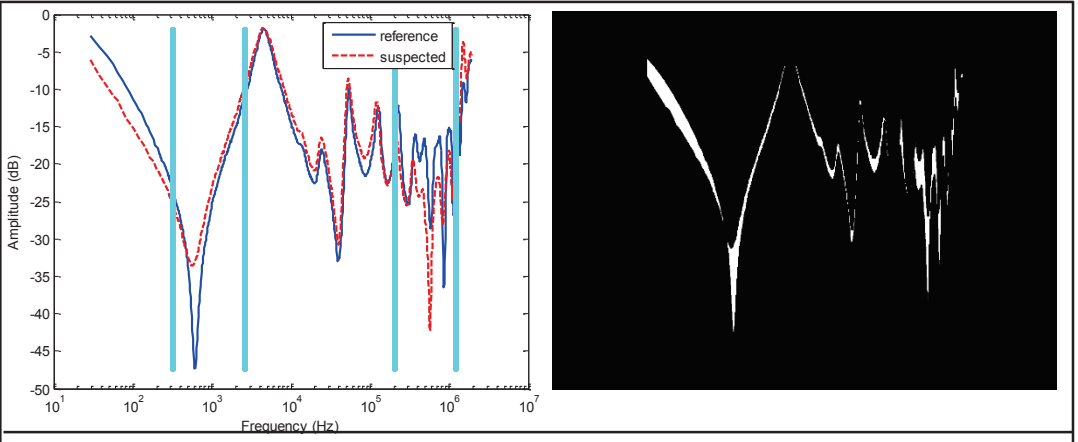

Figure 5.20: Performance of HDR Classifier: Case 3

Figure. 5.20 shows the assessment results of this case by using the HDR classifier, which includes the FRA plot with frequency sub-bands and its eroded binary image. FLAG_LF1 = 01 indicates obvious downward displacement of the FRA curve in LF1. The states of FLAG_LF2, FLAG_MF, FLAG_HF1 and FLAG_HF2 all being 0 represent noticeable deviation at each frequency sub-band. The final diagnosis result determined by the HDR classifier is **E** which means mechanical failure with different remanence. According to visual diagnosis of the FRA plot shown in Fig. 5.20, the deviation in the low frequency range is caused by different residual magnetism (DRC). Thus, the assessment result of the HDR classifier agrees with the visual diagnosis.

Case 4

The frequency response used in this case is collected from a 140 MVA, 220/69 kV autotransformer based on construction-based (phase) comparison (explained in Section 2.3, Chapter 2). According to the visual diagnosis conducted by experts, short circuit between turns (SCTFM) causes the deviation between FRA curves. Therefore, the comparison of FRA curves under this condition usually shows obvious vertical displacement in sub-band LF1 and correlative changes in sub-band LF2. This is the most common electrical failure mode. This failure mode mainly affects the magnetizing inductance and winding resistance, so the visible effect mainly exists in low frequency range. This effect is similar with the condition in Case 1 which is DCR. Therefore, the identification between these two cases depends on the performance of the proposed indices ARI and AD.

The key factors of diagnosis of this type of failure mode using HDR classifier are FLAG_LF1, FLAG_LF2 and *quarant*. Due to the reduction of magnetizing inductance, the response curve will move upwards in sub-band LF1, and the angle difference of the minimum anti-resonance in LF2 is usually located at the second quadrant ($quarant = 2$). The deviation level depends on the severity of the failure. It is usually more distinct than the deviation caused by different remanence, and based on the training sets, FLAG_LF1 is usually

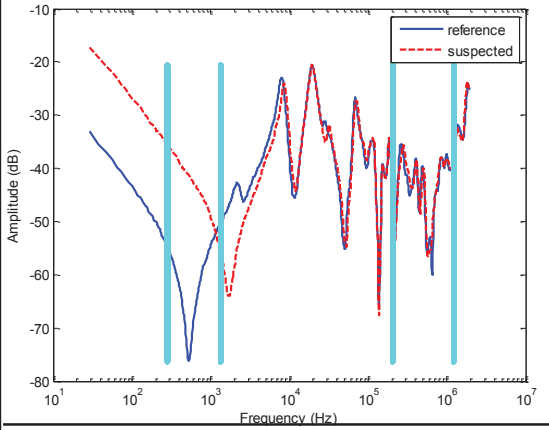

FLAG_LF1=10, FLAG_LF2=0, FLAG_MF=0, FLAG_HF1=1, FLAG_HF2=1, quadrant=1
HDR Classifier diagnosis: A
Validation: Pass

Figure 5.21: Performance of HDR Classifier: Case 4

set to 10 in the algorithm shown in BlockLF1(Fig. 5.14), which indicates the displacement level and direction. Figure. 5.21 shows the assessment results of this case obtained by using the HDR classifier, which includes the FRA plot with frequency sub-bands and its eroded binary image. The final diagnosis result is **A** (SCTFM) matches the visual diagnosis. Meanwhile, it also verified the performance of *ARI* and *AD*.

Case 5

The frequency response used in this case is reprinted from [29]. The configuration of the tested transformer is not given by [29]. This frequency response diagram is shown as an example of open circuit response from a HV open-circuit test in [29]. This type of failure mode would cause very high impedances and commonly affect frequency response over a wide frequency range. When the open-circuited point is completely broken, the measured FRA result often presents capacitive property or gets lost in noise floor. This situation can be easily classified by the HDR classifier during the procedure using Block LF1 shown in Fig. 5.14. Nevertheless, this case corresponds to the situation that

parts of parallel coils are not broken thereby keeping an electrical connection. An increasing attenuation usually occurs in the frequency responses of this failure mode. Another characteristic of this failure mode is that new resonance peaks and valleys could appear in sub-band MF or LF2.

Figure. 5.22 shows the assessment results of this case by using the HDR classifier, which includes the FRA plot with frequency sub-bands and its eroded binary image. The key factors considered in the HDR classifier are downward shift of the FRA curves in sub-band LF1 accompanied by angle difference of the minimum anti-resonance in LF2 at the second or the fourth quadrants ($quarant = 3$ *or* 4), and the deviation in the overall frequency range. In this case, FLAG_LF2 = 01, $quarant = 3$, FLAG_LF2 = 0, FLAG_MF = 0, FLAG_HF1= 0 and FLAG_HF2 = 0. Hence, the final diagnosis result is class **C** which indicates an open circuit failure. Thus, the assessment result of the HDR classifier agrees with the visual diagnosis.

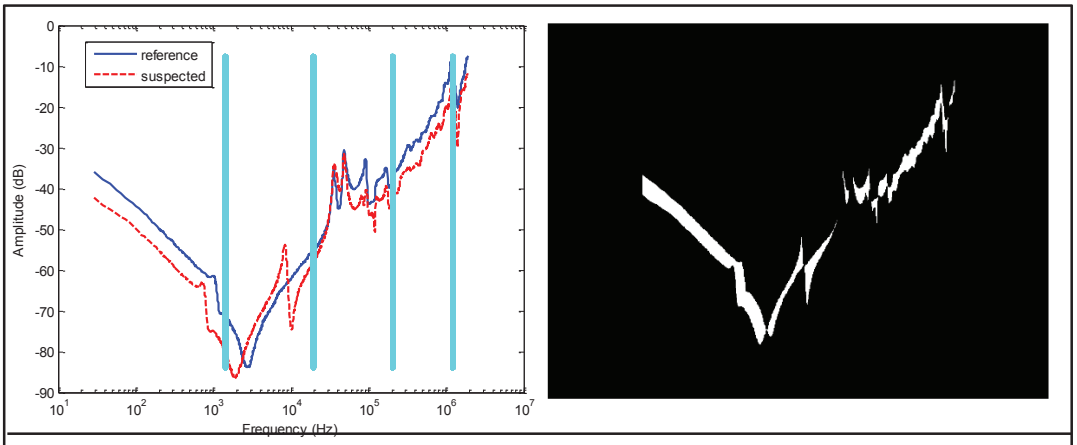

Figure 5.22: Performance of HDR Classifier: Case 5

5.6.2 Discussion on the Performance of HDR Classifier

During the further verification of the performance of the proposed HDR classifier using 12 sets of experimental FRA data, only one case failed to pass the validation. The diagnosis of this failed case has a reproducibility problem due to connection technique or injection polarity accompanied by different remanence. This kind of failure should be classed to **F**, but the HDR Classifier diagnoses this case to **E** which is mechanical failure modes with different remanence. Hence, the diagnosis result at low frequencies is correct, but it goes wrong for the causes of deviation at high frequencies. This wrong judgement probably can be corrected by considering the cases of the reproducibility issue in the design of the HDR classifier. Due to lack of the data regarding the reproducibility issue, the abnormality is not considered in the proposal of the HDR classifier. This is a great challenge to improve the performance of the HDR classifier in future work. In conclusion, the performance of the HDR classifier in this implementation is 95.83% (0.5 out of 12) of validity.

The implementations of HDR classifier on the 20 sets of training data and 12 sets of random FRA data all show very good performance. The HDR classifier can be refined by applying a larger amount of data for training to more accurately determine the size of SE and the threshold values of the indices.

The HDR classifier can aggregate subjective expertise and approved statistical indices in furtherance of automatic decision analysis on identifying transformer failure modes or conditions. It is applicable in potential commercial use. By embedding the HDR classifier to the FRA instruments, automatic condition assessment of transformers is possible to be realized during the FRA measurement.

5.7 Summary

A Hierarchical Dimension Reduction (HDR) classifier has been proposed in this chapter to identify typical transformer failure modes or conditions. To establish the HDR classifier, image processing technologies, including image bi-

nalization and binary erosion, are utilized to preprocess measured FRA data for the purpose of optimizing the input data set for further processing. Meanwhile, FRA diagrams are re-scaled in a liner coordinate system counted by pixels for the convenience of implementing the new proposed indices. Two algorithms of indices *ARI* and *AD* are proposed based on human experts' knowledge. These indices increases the sensitivity of the hybrid indices at low frequencies. The high performance of *ARI* and *AD* is verified with respect to identification of electrical failures (eg. SCTFM) and the condition of residual magnetization (DRC). Moreover, this chapter also proposes an approach to dynamically divide the frequency range into 5 sub-bands according to the correlation between electrical properties and features of FRA responses. The algorithms of this division method are uncomplicated and easy to implement, and only the FRA magnitude plots are needed. This division method of frequency range is more reasonable than the conventional fixed range of frequency sub-bands and more applicable than other existing method. The performance of this classifier has been verified by implementing it with experimental data of FRA.

Chapter 6

Conclusions and Future Work

6.1 Summary and Conclusions

This thesis presented studies of power transformer condition assessment aimed at two targets: developing an accurate transformer winding model for the interpretation of FRA responses specific to incipient winding faults, and establishing intelligent algorithms for automatically identifying transformer failure modes based on FRA techniques. The work and the promising results in the preceding chapters are summarized as follows:

The preliminary step was to review typical failure modes of power transformers. The influence of short-circuit current on transformer windings was explained in detail, because winding defects caused by short-circuit current from the correlative systems are the main threats to in-service transformers. The fundamental knowledge of transformer failure modes is the basis to establish the HDR classifier. The FRA technique is an effective method to detect winding defects and has been applied in this research work. FRA can be accessed by either physical measurement or transformer modeling. Although the work in this thesis was focussed on transformer modeling, the basic knowledge of FRA measurement and FRA instrument attributes provided a link between the practical tests and modeling. An experiment for testing the effect of minor axial winding movement on frequency responses was demonstrated, and

the corresponding results were used to support the implementation of HDR classifier and the determination of the threshold values of the hybrid indices.

Detecting incipient winding faults before a real failure occurs can gain more time for appropriate maintenance management. Therefore, providing accurate interpretations of the FRA data with regard to the incipient winding faults is of supreme importance. To achieve this goal, a review of widely used transformer modeling methods was undertaken to reveal which modeling method is suitable for interpreting frequency responses in a sufficiently broad frequency range. A simplified distributed parameter model (hybrid winding model) was considered to be an appropriate method for high frequency modeling of power transformers. This hybrid winding model possesses comprehensive properties of less computation complexity and high accuracy of simulation results even in the high frequency range. It was established in this thesis for the purpose of numerical simulations of frequency responses of transformers. The expressions of transfer functions for FRA according to this winding model were presented based on the practical connection methods of the FRA technique.

In previous implementations of the hybrid winding model in FRA simulations, conventional analytical approaches were taken to calculate electrical parameters. However, for transformers with complex geometries or deformed windings, the analytical approaches can on longer ensure the accuracy of the calculated parameters. In this regard, FEM models were considered as an effective tool to calculate more accurate electrical parameters for irregular transformer geometries. Therefore, in this thesis, FEM models were established to simulate magnetic and electric fields within a power transformer to obtain accurate electrical parameters in both cases of undeformed and incipient winding faults. The accuracy improvement in electrical parameters substantially empowers the performance of the hybrid winding model in simulations for the purpose of FRA interpretations.

This modeling methodology (the FEM models plus the hybrid winding model) was implemented to simulate radial winding deformation and minor axial winding movement. Results showed that radial deformation in a wind-

ing leads to significant changes in both ground capacitances and inductances. These changes all have influence on frequency responses. By considering the variations of both the ground capacitances and inductances, the variations in frequency responses in the low frequency range may be neglected, while frequency responses at high frequencies contain detectable information indicating minor radial deformation. In three scenarios of minor axial winding movement, results showed that the change in inductances are subtle. The largest gap between two adjacent discs has major influence on the patterns of frequency response. When the gap gets closer to the high voltage lead, the distortion above 2 MHz becomes much more significant. The differences between the frequency response traces are more detectable with a larger gap between two adjacent discs especially in the range of middle and high frequencies. These results revealed the characteristic features of the corresponding types of winding fault. Therefore, by adopting this methodology, indications corresponding to mechanical winding faults can be extracted from FRA data. Consequently, this extracted information can support the diagnosis by identifying similar fault features from measured frequency response data.

In order to develop an intelligent interpretation tool for automatic condition assessment of power transformers, a Hierarchical Dimension Reduction (HDR) classifier was proposed for the first time. This classifier was designed to identify typical transformer failure modes or conditions using the hybrid quantitative indices following the dimension reduction of the raw FRA data. To establish the HDR classifier, image processing technologies, including image binalization and binary erosion, were utilized to preprocess the measured FRA data for the purpose of optimizing the input data set for further processing. In the meantime, FRA diagrams were re-scaled in a liner coordinate system for the convenience of implementing the new proposed indices. As a part of the hybrid indices, two proposed algorithms of indices based on existing knowledge enhanced the sensitivity of the hybrid indices at low frequencies. High performance has been achieved in the identification of electrical failures and the condition of residual magnetization.

Moreover, this research also proposed an approach to dynamically divide the frequency range into 5 sub-bands according to the correlation between electrical properties and features of FRA responses. This division method of frequency range was more reasonable than the conventional fixed range of frequency sub-bands and more applicable than other existing method. Based on these advantageous processes, the HDR classifier can aggregate subjective expertise and approved statistical indices in furtherance of automatic decision analysis on identifying transformer failure modes or conditions. The performance of this classifier has been verified by 32 sets of experimental FRA data, in which 20 sets are primarily used for determination of threshold values of the related algorithms and the rest 12 are purely used for the verification. Results of this implementation of the HDR classifier are 100% accuracy with using the 20 sets of training data and 95.83% accuracy with using the rest 12 sets.

6.2 Future Research

Future research may be undertaken in the following directions:

- In the present work, the methodology of transformer modeling was implemented in a single phase power transformer. Based on the advantages of computational FEM models with regard to dealing with complex geometries, further simulation studies and model verification can be undertaken within three-phase power transformers.

  In addition to the proposed FEM models for calculating the inductances and shunt capacitance between coaxial components, construction of 3-D FEM models of three-phase transformers for calculating the shut capacitance between components in different phases is worthwhile for the purpose of simulating mechanical faults in a three-phase transformer. In this manner, the simulation studies are closer to the real conditions of in-service transformers, which thereby can establish more reliable interpretation criteria for FRA diagnosis.

- Only 20 sets of experimental data were used to decide the threshold values in the proposed HDR classifier. In future work, extensive data with more general representation of different types of power transformers should be used to refine the threshold values of indices to improve the applicability of the HDR classifier.

- Limited types of transformer failure modes were considered in the establishment of the structure of the HDR classifier. Further research can be conducted to extend the HDR classifier by considering more types of transformer failure modes or conditions, when reliable data are available. This work requires the support of a sufficient database of frequency responses regarding various transformers with different types of faults.

References

[1] H. M. Ahn, Y. H. Oh, J. K. Kim, J. S. Song, and S. C. Hahn. Experimental verification and finite element analysis of short-circuit electromagnetic force for dry-type transformer. *IEEE Transactions on Magnetics*, 48(2):819–822, Feb. 2012.

[2] M. Bagheri. *Transformer Winding Deformation and Insulation Characteristic Effects on Frequency Response Analysis*. PhD thesis, University of New South Wales, 2009.

[3] User Manual. *Sweep Frequency Response Analyzer for Power Transformer Winding Diagnosis*. OMICRON electronics GmbH, FRA.AE.8 edition, 2009.

[4] A. Shintemirov. *Modelling And Condition Assessment of Power Transformers Using Computational Intelligence*. PhD thesis, University of Liverpool, 2009.

[5] J. L. Velasqueza, M. Krugera, S. Knuttera, A. Kraetgea, and S. Galceranb. Noise in fra measurements: Sources, effects and suppression methods. In *Workshop "Diagnostic Measurements on Power Transformers"*. OMICRON electronics GmbH, 2009.

[6] E. Bjerkan. *High Frequency Modelling of Power Transformers: Stresses and Diagnostics*. PhD thesis, Norwegian University of Science and Technology, 2005.

[7] N. Abeywickrama. *Effect of Dielectric and Magnetic Material Characteristics on Frequency Response of Power Transformers*. PhD thesis, Chalmers University of Technology, Sweden, 2007.

[8] J. L. Velasquez-Contreras, D. Kolb, M. A. Sanz-Bobi, and W. Koltunowicz. Identification of transformer-specific frequency sub-bands as basis for a reliable and automatic assessment of FRA results. In *Conference on Condition Monitoring and Diagnosis 2010 (CMD2010)*, Tokyo, Japan, Sep. 2010.

[9] D. M. Sofian. *Transformer FRA interpretation for detection of winding movement*. PhD thesis, The University of Manchester, 2007.

[10] CIGRÉ WG A2.26. *Mechanical-Condition Assessment of Transformer Winding Using Frequency Response Analysis (FRA)*. CIGRÉ Technical Brochure 342, 2008.

[11] T. Westman, P. Lorin, and P. A. Ammann. Fit at 50. *ABB review 1|2010*, pages 63–69, Oct. 2010.

[12] M. Wang, A. J. Vandermaar, and K. D. Srivastava. Review of condition assessment of power transformers in service. *IEEE Electrical Insulation Magazine*, 18(6):12–25, Nov. 2002.

[13] S. Chakravorti, B. Chatterjee, and D. Dey. *Recent Trends in the Condition Monitoring of Transformers*. Springer, 2013.

[14] V. I. Kogan, J. A. Fleeman, J. H. Provanzana, and C. H. Shih. Failure analysis of ehv transformers. *IEEE Transactions on Power Delivery*, 3(2):672–683, Apr. 1988.

[15] R. P. Y. Mehairajan, M. Van-Hattem, D. Djairam, and J. J. Smit. Risk-based approach to maintenance management applied on power transformers. In *9th WCEAM Research Papers*, pages 415–434. Springer, 2015.

[16] Ahmed E.B. Abu-Elanien and M.M.A. Salama. Asset management techniques for transformers. *Electric Power Systems Research*, 80(4):456 – 464, 2010.

[17] C. Roberts, H. P. B. Dassanayake, N. Lehrasab, and C. J. Goodman. Distributed quantitative and qualitative fault diagnosis: railway junction case study. *Control Engineering Practice*, 10(4):419–429, 2002.

[18] CIGRÉ WG A2.27. *Recommendations for Condition Monitoring and Condition Assessment Facilities for Transformers*. CIGRÉ Technical Brochure 343, 2008.

[19] V. Sokolov, Z. Berler, and V. Rashkes. Effective methods of assessment of insulation system conditions in power transformers: a view based on practical experience. In *EIC and EMCWE'99. Proceedings, Cincinnati, USA*, pages 659–667, 1999.

[20] P. Feghali. Life extension methodology through the replacement of old ltcs. In *the 5th Annual Weidmann-ACTI Technical Conference. Albuquerque, New Mexico*, pages 1–6, 2006.

[21] S. V. Kulkarni and S. A. Khaparde. *Transformer Engineering: design and practice*, volume 25. CRC Press, 2004.

[22] W. H. Tang. *Intellegent Condition Monitoring and Assessment for Power Transformers*. PhD thesis, The University of Liverpool, U.K., 2004.

[23] CIGRÉ WG A3. *State of the Art of Instrument Transformers*. CIGRÉ Technical Brochure 394, 2009.

[24] M.D. Judd, S.D.J. McArthur, J.R. McDonald, and O. Farish. Intelligent condition monitoring and asset management. partial discharge monitoring for power transformers. *Power Engineering Journal*, 16(6):297–304, 2002.

[25] M. Wu, H. Cao, J.N. Cao, H.L. Nguyen, J.B. Gomes, and S.P. Krishnaswamy. An overview of state-of-the-art partial discharge analysis techniques for condition monitoring. *IEEE Electrical Insulation Magazine*, 31(6):22–35, Nov. 2015.

[26] W.S. Zaengl. Dielectric spectroscopy in time and frequency domain for hv power equipment. i. theoretical considerations. *IEEE Electrical Insulation Magazine*, 19(5):5–19, Sept 2003.

[27] T.K. Saha and P. Purkait. Investigation of polarization and depolarization current measurements for the assessment of oil-paper insulation of aged transformers. *IEEE Transactions on Dielectrics and Electrical Insulation*, 11(1):144–154, Feb 2004.

[28] BS EN 60076-18:2012. *Power transformers. Measurement of frequency response.* BSI Standards Limited, 2013.

[29] IEEE Standard. IEEE guide for the application and interpretation of frequency response analysis for oil-immersed transformers. *IEEE Std C57.149-2012*, Mar. 2013.

[30] Z. W. Zhang, W. H. Tang, T. Y. Ji, and Q. H. Wu. Finite-element modeling for analysis of radial deformations within transformer windings. *IEEE Transactions on Power Delivery*, 29(5):2297–2305, Oct. 2014.

[31] Z. W. Zhang, W. H. Tang, Q. H. Wu, and J. D. Yan. Detection of minor axial winding movement within power transformers using finite element modeling. In *PES General Meeting | Conference Exposition, 2014 IEEE*, pages 1–5, Jul. 2014.

[32] S. A. Ryder. Diagnosing transformer faults using frequency responce analysis. *IEEE Electrical Insulation Magazine*, 19(2):16–22, 2003.

[33] E. Rahimpour, J. Christian, and K. Feser. Transfer function method to diagnose axial displacement and radial deformation of transformer windings. *IEEE Transactions on Power Delivery*, 18(2):493–505, 2003.

[34] M. Wang, A. J. Vandermaar, and K. D. Srivastava. Improved detection of power transformer winding movement by extending the fra high frequency range. *IEEE Transactions on Power Delivery*, 20(3):1930–1938, 2005.

[35] T. Y. Ji, W. H. Tang, and Q. H. Wu. Detection of power transformer winding deformation and variation of measurement connections using a hybrid winding model. *Electric Power System Research*, 87(0):39–46, 2012.

[36] W. Lech and L. Tyminski. New method of fault indication in dynamic strength testing transformers. *Electrichestvo*, pages 77–81, 1966.

[37] M. Waters, A. Stalewski, J. C. Farr, and J. D. Whitaker. Short-circuit testing of power transformers and the detection and location damage. In *Conference Internationale des Grandes Reseaux Electriques a Haut Tension*, pages 12–05, 1968.

[38] L. E. Humbard, E. J. Rogers, and D. A. Gillies. Instrumentation techniques for low voltage impulse testing of power transformers. *IEEE Transactions on Power Apparatus and Systems*, PAS-91(3):1281–1293, May 1972.

[39] E. P. Dick and C. C. Erven. Transformer diagnostic testing by frequuency response analysis. *IEEE Transactions on Power Apparatus and Systems*, PAS-97(6):2144–2153, Nov. 1978.

[40] S. Tenbohlen and S. A. Ryder. Making frequency response analysis measurements: A comparison of the swept frequency and low voltage impulse methods. In *13th International Symposium on High Voltage Engineering*, Netherlands, 2003.

[41] W. H. Tang, Q. H. Wu, W. H. Tang, and Q. H. Wu. Evidence-based winding condition assessment. In *Condition Monitoring and Assessment of*

Power Transformers Using Computational Intelligence, Power Systems, pages 185–194. Springer London, 2011.

[42] M. Bagheri, M. S. Naderi, T. Blackburn, and T. Phung. Frequency response analysis and short-circuit impedance measurement in detection of winding deformation within power transformers. *IEEE Electrical Insulation Magazine*, 29(3):33–40, May 2013.

[43] G. Bertagnolli. *Short-Circuit Duty of Power Transformers.* Zurich, Switzerland: ABB Ltd., 2007.

[44] M. N. O. Sadiku. *Elements of electro-Magnetics.* Oxford series in electrical and computer engineering. New York, Oxford University Press, 2007.

[45] J. A. S. B. Jayasinghe, Z. D. Wang, P. N. Jarman, and A. W. Darwin. Winding movement in power transformers: a comparison of fra measurement connection methods. *IEEE Transactions on Dielectrics and Electrical Insulation*, 13(6):1342–1349, Dec. 2006.

[46] N. S. Nise. *Control systems engineering.* [Hoboken, NJ]: Wiley, 2008.

[47] P. T. M. Vaessen and E. Hanique. A new frequency response analysis method for power transformers. *IEEE Transactions on Power Delivery*, 7(1):384–391, Jan. 1992.

[48] T. McGrail. *SFRA Basic Analysis Version 1.0*, volume 2. Doble Engineering Co., 2003.

[49] IEC Standard. Measurement of frequency response. *IEC Standard 60076-18*, Jul. 2012.

[50] J. L. Velasquez. *Application Note: Understanding Noise Suppression Methods.* OMICRON electronics GmbH, v2.0 edition, 2010.

[51] Std. DL/T911-2004. Frequency response analysis on winding deformation of power transformers. *The Electric Power Industry Standard of People's*

Republic of China, ICS27.100, F24, Document No. 15182-2005,, Jun. 2005.

[52] P. H. Thomas. Static strains in high tension circuits and the protection of apparatus. *Transactions of the American Institute of Electrical Engineers*, XIX:213–264, Jan. 1902.

[53] J. H. McWhirter, C. D. Fahrnkopf, and J. H. Steele. Determination of impulse stresses within transformer windings by computers [includes discussion]. *Power Apparatus and Systems, Part III. Transactions of the American Institute of Electrical Engineers*, 75(3), Jan. 1956.

[54] X. Z. Dong, D. H. Zhu, C. C. Wang, C. X. Tan, and Y. L. Liu. Simulation of transformer pd pulse propagation and monitoring for a 500 kv substation. *IEEE Transactions on Dielectrics and Electrical Insulation*, 6(6):803–813, Dec. 1999.

[55] T. Y. Ji, W. H. Tang, and Q. H. Wu. Partial discharge location using a hybrid transformer winding model with morphology-based noise removal. *Electric Power Systems Research*, 101:9–16, 2013.

[56] R. C. Degeneff, W. J. McNutt, W. Neugebauer, J. Panek, M. E. McCallum, and C. C. Honey. Transformer response to system switching voltages. *IEEE Transactions on Power Apparatus and Systems*, PAS-101(6):1457–1470, Jun. 1982.

[57] M. Popov, L. Van-Der-Sluis, R. P. P. Smeets, J. Lopez-Roldan, and V. V. Terzija. Modelling, simulation and measurement of fast transients in transformer windings with consideration of frequency-dependent losses. *IET Electric Power Applications*, 1(1):29–35, Jan. 2007.

[58] H. Akay, S. M. Islam, and B. Ninness. Identification of power transformer models from frequency response data: A case study. *Signal Processing*, 68(3):307–315, 1998.

[59] B. Gustavsen. Wide band modeling of power transformers. *IEEE Transactions on Power Delivery*, 19(1):414–422, Jan. 2004.

[60] B. Gustavsen and A. Semlyen. Application of vector fitting to state equation representation of transformers for simulation of electromagnetic transients. *IEEE Transactions on Power Delivery*, 13(3):834–842, Jul. 1998.

[61] A. O. Soysal and A. Semlyen. Practical transfer function estimation and its application to wide frequency range representation of transformers. *IEEE Transactions on Power Delivery*, 8(3):1627–1637, Jul. 1993.

[62] D. J. Wilcox. Theory of transformer modelling using modal analysis. *Generation, Transmission and Distribution, IEE Proceedings C*, 138(2):121–128, Mar. 1991.

[63] D. J. Wilcox, W. G. Hurley, T. P. McHale, and M. Conlon. Application of modified modal theory in the modelling of practical transformers. *Generation, Transmission and Distribution, IEE Proceedings C*, 139(6):513–520, Nov. 1992.

[64] M. Condon and D. J. Wilcox. Tuning of resonant modal transformer models. In *Proceedings of IPST*, volume 99, pages 474–479, 1999.

[65] E. C. Cherry. The duality between interlinked electric and magnetic circuits and the formation of transformer equivalent circuits. *Proceedings of the Physical Society. Section B*, 62(2):101, 1949.

[66] C. M. Arturi. Transient simulation and analysis of a three-phase five-limb step-up transformer following an out-of-phase synchronization. *IEEE Transactions on Power Delivery*, 6(1):196–207, Jan. 1991.

[67] M. Elleuch and M. Poloujadoff. New transformer model including joint air gaps and lamination anisotropy. *IEEE Transactions on Magnetics*, 34(5):3701–3711, Sep. 1998.

[68] J. Pleite, R. Prieto, R. Asensi, J. A. Cobos, and E. Olias. Obtaining a frequency-dependent and distributed-effects model of magnetic components from actual measurements. *IEEE Transactions on Magnetics*, 35(6):4490–4502, Nov. 1999.

[69] N. Abeywickrama, A. D. Podoltsev, Y. V. Serdyuk, and S. M. Gubanski. Computation of parameters of power transfromer windings for use in frequency response analysis (FRA). *IEEE Transactions on Magnetics*, 43(5):1983–1990, 2007.

[70] A. Shintemirov, Z. J. Richardson, and Q. H. Wu. Transformer core parameter identification using frequency response analysis. *IEEE Transactions on Magnetics*, 46(1):141–149, 2010.

[71] N. Abeywickrama, Y. V. Serdyuk, and S. M. Gubanski. Exploring possibilities for characterisation of power transfromer insulation by frequency response analysis (FRA). *IEEE Transactions on Power Delivery*, 21(3):1375–1382, 2006.

[72] N. Abeywickrama, Y. V. Serdyuk, and S. M. Gubanski. High-frequency modeling of power transformers for use in frequency response analysis (FRA). *IEEE Transactions on Power Delivery*, 23(4):2042–2049, Oct. 2008.

[73] M. Florkowski and J. Furgal. Detection of transformer winding deformations based on the transfer function- measurements and simulations. *Measurement Science and Technology*, 14(11):1986–1992, 2003.

[74] K. W. Wagner. The progress of an electromagnetic wave in a coil with capacity between turns. *Electrotechnik und Maschinenbau*, pages 89–107, 1915.

[75] A. Shintemirov, W. H. Tang, and Q. H. Wu. A hybrid winding model of disc-type power transformers for frequency response analysis. *IEEE Transactions on Power Delivery*, 24(2):730–739, Apr. 2009.

[76] M. Popov, L. Van-Der-Sluis, G. C. Paap, and H. De-Herdt. Computation of very fast transient overvoltages in transformer windings. *IEEE Transactions on Power Delivery*, 18(4):1268–1274, Oct. 2003.

[77] L. V. Bewley. *Traveling Waves on Transmission Systems*. Dover, New York, USA, 1963.

[78] R. Rüdenberg. *Electrical Shock Waves in Power Systems: Traveling Waves in Lumped and Distributed Circuit Elements*. Harvard University Press, Cambridge, Massachusetts, 1968.

[79] C. R. Paul. *Analysis of Multiconductor Transmission Lines*. John Wiley & Sons, Inc., New York, 1994.

[80] D. J. Wilcox, M. Conlon, and W. G. Hurley. Calculation of self and mutual impedances for coils on ferromagnetic cores. *IEE Proceedings-Science, Measurement and Technology*, 135(7):470–476, 1988.

[81] D. J. Wilcox, W. G. Hurley, and M. Conlon. Calculation of self and mutual impedances between sections of transformer windings. *IEE Proceedings- Generation, Transmission and Distribution*, 136(5):308–314, 1989.

[82] A. Shintemirov, W. J. Tang, W. H. Tang, and Q. H. Wu. Improved modelling of power transformer winding using bacterial swarming algorithm and frequency response analysis. *Electric Power System Research*, 80(9):1111–1120, 2010.

[83] S. N. Hettiwatte, P. A. Crosley, Z. D. Wang, A. W. Darwin, and G. Edwards. Simulation of a transformer winding for partial discharge propagation studies. In *IEEE Power Engineering Society Winter Meeting*, volume 22, pages 1394–1399, Jan. 2002.

[84] COMSOL Inc. *Introduction to Comsol Multiphysics*, 4.0a edition, 2010.

[85] A. D. Podoltsev, N. Abeywickrama, Y. V. Serdyuk, and S. M. Gubanski. Multiscale computation of parameters of power transfromer windings at high frequencies. part I: Small-scale level. *IEEE Transactions on Magnetics*, 43(11):3991–3996, 2007.

[86] A. D. Podoltsev, N. Abeywickrama, Y. V. Serdyuk, and S. M. Gubanski. Multiscale computation of parameters of power transfromer windings at high frequencies. part II: large-scale level. *IEEE Transactions on Magnetics*, 43(12):4076–4082, 2007.

[87] Z. D. Wang, J. Li, and D. M. Sofian. Interpretation of transformer fra responses; part i: Influence of winding structure. *IEEE Transactions on Power Delivery*, 24(2):703–710, 2009.

[88] Y. Yang, Z. J. Wang, X. Cai, and Z. D. Wang. Improved lumped parameter model for transformer fast transient simulations. *IET Electric Power Applications*, 5(6):479–485, Jul. 2011.

[89] A. Konrad. Integrodifferential finite element formulation of two-dimensional steady-state skin effect problems. *IEEE Transactions on Magnetics*, 18(1):284–292, Jan. 1982.

[90] T. Dreher and G. Meunier. 3d modeling of electromagnets fed by alternating voltage sources. *IEEE Transactions on Magnetics*, 29(2):1341–1344, Mar. 1993.

[91] P. Karimifard and G.B. Gharehpetian. A new algorithm for localization of radial deformation and determination of deformation extent in transformer windings. *Electric Power Systems Research*, 78(10):1701 – 1711, 2008.

[92] E. Rahimpour, M. Jabbari, and S. Tenbohlen. Mathematical comparison methods to assess transfer functions of transformers to detect different types of mechanical faults. *IEEE Transactions on Power Delivery*, 25(4):2544–2555, Oct 2010.

[93] J. Bak-Jensen, B. Bak-Jensen, and S. D. Mikkelsen. Detection of faults and ageing phenomena in transformers by transfer functions. *IEEE Transactions on Power Delivery*, 10(1):308–314, Jan. 1995.

[94] A.J. Ghanizadeh and G.B. Gharehpetian. Ann and cross-correlation based features for discrimination between electrical and mechanical defects and their localization in transformer winding. *IEEE Transactions on Dielectrics and Electrical Insulation*, 21(5):2374–2382, Oct 2014.

[95] M.F.M. Yousof, C. Ekanayake, and T.K. Saha. Frequency response analysis to investigate deformation of transformer winding. *IEEE Transactions on Dielectrics and Electrical Insulation*, 22(4):2359–2367, August 2015.

[96] J. L. Velasquez-Contreras, M. A. Sanz-Bobi, M. Gutierrez, and A. Kraetgea. Knowledge bases for the interpretation of the frequency response analysis of power transformers. In *Congreso Internacional en Alta Tensin y Aislamiento Elctrico, ALTAE 2009*, pages 23–27, Medelln, Colombia., Nov. 2009.

[97] J. C. Gonzales and E. E. Mombello. Automatic detection of frequency ranges of power transformer transfer functions for evaluation by mathematical indicators. In *Transmission and Distribution: Latin America Conference and Exposition (T&D-LA), 2012 Sixth IEEE/PES*, pages 1–8. IEEE, 2012.

[98] B. J. Mann and I. F. Morrison. Digital calculation of impedance for transmission line protection. *IEEE Transactions on Power Apparatus and Systems*, pages 270–279, 1971.

[99] Q. H. Wu, Z. Lu, and T. Y. Ji. *Protective relaying of power systems using mathematical morphology*. Springer Science & Business Media, 2009.

[100] H. M. Ahn, J. Y. Lee, J. K. Kim, Y. H. Oh, S. Y. Jung, and S. C. Hahn. Finite-element analysis of short-circuit electromagnetic force in power

transformer. *IEEE Transactions on Industry Applications*, 47(3):1267–1272, May 2011.

[101] D. K. Xu, C. Z. Fu, and Y. M. Li. Application of artificial neural network to the detection of the transformer winding deformation. In *High Voltage Engineering, 1999. Eleventh International Symposium on (Conf. Publ. No. 467)*, volume 5, pages 220–223, 1999.